Charging and Aggregation Behaviors of Model Colloidal Particles

- Effects of Flow on Aggregation Rates and Hetero-aggregation with Charge Reversal -

January 2018

Takuya SUGIMOTO

Charging and Aggregation Behaviors of Model Colloidal Particles

- Effects of Flow on Aggregation Rates and Hetero-aggregation with Charge Reversal -

A Dissertation Submitted to
the Graduate School of Life and Environmental Sciences,
University of Tsukuba
in Partial Fulfillment of the Requirements
for the Degree of Doctor of Philosophy in Agricultural Science
(Doctoral Program in Appropriate Technology and Sciences for
Sustainable Development)

Takuya SUGIMOTO

Contents

List of symbols

R_1, R_2: particle radii
N_A: the Avogadro number
C_i, $C_{i,b}$: ionic number concentration of ith species, and its value in the bulk
z_i: ionic valence of ith species
e: elementary charge
$\boldsymbol{E}$: electrical field
$\boldsymbol{n}$: outward normal unit vector
$\psi(x)$: electrical potential at position x
ψ_0: surface potential= $\psi(0)$
σ_0: surface charge density
σ_d: charge density at the start of diffuse double layer
k_B: the Boltzmann constant
T: absolute temperature
$\epsilon_r\epsilon_0$: dielectric constant in a medium
κ^{-1}: the Debye length
Q: total charge amount
h: inter-particle separation
A_{H}: the Hamaker constant
$F^S(h)$: inter-particle interaction force
$V^S(h)$: inter-particle interaction potential
Π_{dl}: disjoining pressure due to the electrical double layer
Γ_i: site density of surface groups i
K_i: dissociation constant of the surface groups i
a_i^s: surface activity of ith species
$F(\phi, m)$: the elliptic integral of the first kind
$\mathrm{sn}(u,m), \mathrm{cn}(u,m), \mathrm{dn}(u,m), \mathrm{cd}(u,m)$: the Jacobian elliptic functions
$C_{\pm}^I$: inner layer capacitance
$C_{\pm}^{dl}$: diffuse layer capacitance of isolated surfaces
C_s: the Stern layer capacitance
$p_{\pm} = C_{\pm}^{dl}/(C_{\pm}^{dl} + C_{\pm}^I)$: regulation param-

eter
μ_m: electrophoretic mobility
η: viscosity of a medium
ν: kinematic viscosity of a medium
ζ: zeta (electrokinetic) potential
N_i: number concentration of ith flocs
k_{ij}: aggregation rate coefficients between ith and jth flocs
D_{ij}: relative diffusion coefficient ith and jth flocs
W: stability ratio
$\boldsymbol{r}$: position vector with the magnitude of r
r^*: dimensionless distance of r
$\boldsymbol{e}_i$: unit vector in the direction of ith component
$\nabla \boldsymbol{u} = G_{ij}$: velocity gradient tensor
E_{ij}: rate-of-strain tensor
G: shear rate
$t^* = Gt$: dimensionless time of t
δ_{ij}: Kronecker's delta
ρ: particle size ratio
$\mathcal{A}, \mathcal{B}$: hydrodynamic interaction functions for shearing motion
$\mathcal{G}, \mathcal{H}$: hydrodynamic interaction functions for Brownian motion
α: capture efficiency
ϵ_{T}: turbulent energy dissipation rate per unit mass
Pe: the Peclet number
$x^i_{\alpha\beta}$, $y^i_{\alpha\beta}$ $(i = a, b, c, g)$: hydrodynamic mobility functions
$X^I_{\alpha\beta}$, $Y^I_{\alpha\beta}$ $(I = A, B, C, G, H)$: hydrodynamic resistance functions

Chapter 1

General introduction

1.1 Background and objectives

A significant amount of colloidal particles with their sizes of few nm to few μm such as clay minerals and natural organic matters can be found in the natural water, turbid water generated by a heavy rain, and in soils as shown in **Fig. 1.1.1**. The colloidal particles have some important characters; small in size, large specific surface area, a large amount of reactive surface sites, and charged surfaces due to surface functional groups, isomorphous substitution, and ion adsorption. These natures provide colloidal particles with the ability to adsorb contaminants such as heavy metals and agricultural chemicals. Once these particles are transported in the groundwater, they play an important role to control transport phenomena in water environments[1, 2]. Colloidal

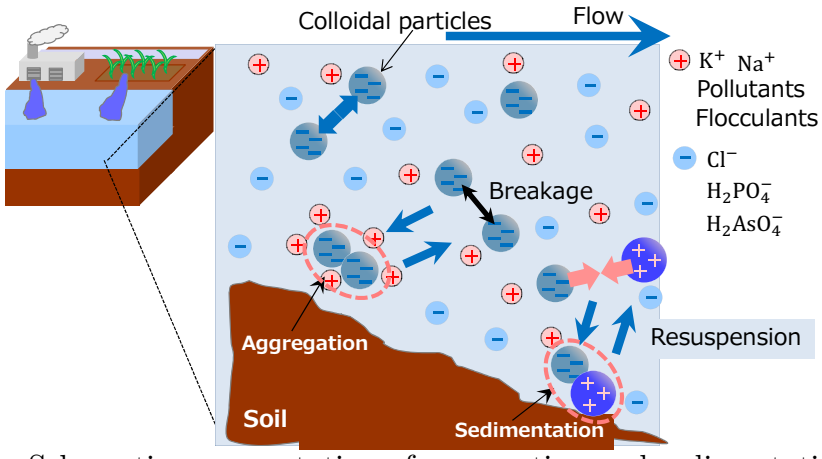

Figure 1.1.1: Schematic representation of aggregation and sedimentation relevant to transport properties of colloidal particles such as clay minerals and metal oxides in water environments.

particles aggregate in accordance with the change in chemical and hydrodynamic conditions around the particles. The aggregation of colloidal particles increases the size of transport unit. As a consequence, the transport properties also largely change[3]. Therefore, understanding the aggregation process of the colloidal particles is important to control the transport phenomena of colloidal particles in solid-liquid separation processes and in the prediction of spreading of contaminants in soil and water environments.

The aggregation process is typically determined by the physicochemical interaction and the collision frequency between the colliding particles[2]. The former is mainly composed of the van der Waals (vdW) attraction and the electrical double layer forces as shown in **Fig. 1.1.2**. The net force can be described as the sum of these interaction forces according to the classical theory by the Derjaguin-Landau-Verwey-Overbeek (DLVO), so-called the DLVO theory[4, 5]. The collision is mainly induced by Brownian motion in quiescent fluid and by the velocity difference in fluid such as laminar shear and turbulent flows as depicted in **Fig. 1.1.3**[6, 7, 8, 9, 10, 11].

Theoretical formulation for aggregation kinetics in Brownian motion and a laminar shear flow was undertaken by Smoluchowski[12], while the corresponding formulation in isotropic turbulence was derived by Saffman and Turner[13]. Unfortunately, their formulation neglects any interactions although the colliding particles hydrodynamically

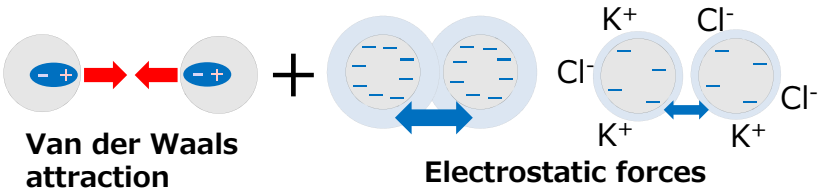

Figure 1.1.2: Schematic picture of the van der Waals attraction and electrostatic forces between colloidal particles explained in DLVO theory

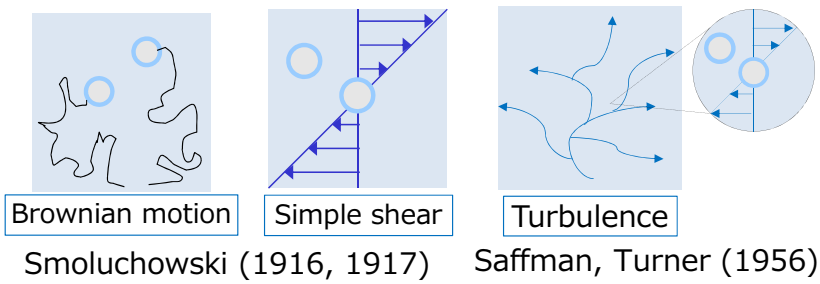

Figure 1.1.3: Schematic view of three typical collision modes to form aggregates such as Brownian motion, laminar shear, and turbulent flows.

and physicochemically interact with each other in more realistic system. Therefore, in general, their expression causes the overestimation in aggregation rates between colloidal particles.

To reduce such overestimation in the aggregation rates, one should include the physico-chemical and hydrodynamic interactions. The physico-chemical interactions can be described by the DLVO theory as mentioned above. The hydrodynamic interactions mean that changes in the velocities or forces acting on each neighboring particles from those for an isolated particle result from the disturbance induced by their existence. In the case of particles in creeping flow where the Reynolds number is sufficiently low, the hydrodynamic interaction has been formulated as a form of resistance-mobility problem to express the linear relationship between particle velocities and forces by Brenner[14, 15]. For example, when particles approach each other, the fluid in the gap between the particles is squeezed out, and the induced large velocity gradient between the gap causes the inter-particle viscous repulsion called a lubrication effect.

The aggregation induced by Brownian motion is called Brownian aggregation mainly determined by diffusion flux and physico-chemical interactions. The effect of physico-chemical interactions on Brownian aggregation has been incorporated by including the contribution from the conservative forces given by the gradient of potential energy to the inter-particle collision flux[16]. The effect of hydrodynamic interaction has been introduced by taking into account the correction factor to the relative diffusion coefficients between particles due to the additional drag based on the Brenner's formulation[17]. Thereafter, a useful approximated correlation function to the hydrodynamic correction factor[17] has been proposed by Honig[18].

Typically, aggregation between identical colloidal particles is impeded by the electrostatic repulsion attributed to the excess osmotic pressure due to the overlapped electrical double layers at low salt concentration. Such condition is called the slow aggregation regime. By increasing salt concentration and decreasing the electrostatic repulsion due the electrical screening, the aggregation is accelerated and its rates reach to a plateau above a certain salt concentration, so-called the critical coagulation concentration (CCC). Above CCC, the repulsions become negligible. Such condition

is called the fast aggregation regime. The experimental verifications for the prediction of the Brownian aggregation rates focusing on the fast and slow regions have been performed by many researchers[19, 20, 21]. Their experimental results of Brownian aggregation are explained by DLVO theory in a qualitative manner. Nevertheless, the well-known considerable quantitative discrepancies between experiments and the theory were observed at conditions in the presence of the electrostatic repulsion. The developments of surface force apparatus and atomic force microscope have allowed us to directly measure the interaction forces between surfaces. The direct force measurements have confirmed the validity of DLVO theory except in the range of several Å of surface separation distance[22]. However, in the landmark study by Behrens *et al.*[23], quantitative agreements between experimental and theoretical values for Brownian aggregation rates even in the presence of the electrostatic repulsion have been reported in the case of low surface charge densities (≤ 3 mC/m^2).

In their study of Brownian aggregation[23], colloidal particles are immersed in indifferent monovalent electrolyte solutions, in which ions do not adsorb on their surface. However, more practically, the particles may co-exist with multivalent ions[24, 25, 26], polyelectrolytes[27, 28], and/or hydrophobic organic ions[29] such as surfactants[30, 31], and they can be strongly adsorbed onto the particle surfaces. Such ion adsorptions accompany the compensation of the surface charge amounts on the surfaces, and enhance the particle aggregation by diminishing the electrical repulsion between the particles. Furthermore, the excess accumulation of ions even may induce the change in the sign of the net surface charges, so-called charge reversal[32] with the additional region of slowed aggregation by the recovered electrical repulsion[27, 31]. Although the Brownian aggregation kinetics with the DLVO theory explains the experimental data reasonably well even for such situations using the complementary measurements of their charging behaviors such as zeta potentials through electrophoretic mobilities, some researchers have been trying to model the charging behaviors by including inter-ion correlations[33], or specific interactions with the surfaces[34, 29]. Therefore, modeling the charging behaviors of colloidal particles are still questioning.

In contrast to Brownian aggregation in quiescent fluid, the aggregation caused by shearing motion of fluids is called shear aggregation. The effect of inter-particle

interactions on shear aggregation has been included by calculating the particle collision flux with the trajectory analysis[35], which is a method to calculate the time evolution of relative particle positions by integrating the relative velocity determined by the balance of hydrodynamic and physico-chemical forces[35, 36, 37]. The trajectory analysis has been applied for the analysis of turbulent aggregation rates as a first approximation because the flow in the smallest eddies of a turbulence is expected to be analogous to the shear flow with a mean local shear rate in the turbulence[38]. This assumption is presumable if the length scale, where coagulation occurs, is smaller than the Kolmogoroff microscale of the turbulence. The validity of this approximation has been confirmed by previous researchers in the absence of electrostatic repulsion[6, 38, 39, 40].

More recently, the systematic measurements of the shear aggregation in the presence of the electrostatic repulsion have been carried out as a function of salt concentration at different shear rates[7, 41]. They have reported that the bending point of shear aggregation rates as a function of salt concentration, which corresponds to the CCC for shear aggregation, increases with shear rates, and more gradual dependence on salt concentration is found in higher shear rates. This experimental observations are consistent with the theoretical predictions by the trajectory analysis qualitatively. However, quantitative comparisons of experiments with theory have not yet been performed since approximate expressions of electrostatic repulsion for low electric potential case was used in the previous calculation[35]. This approximation is not valid for high potential cases where we often encounter in experiments.

The review mentioned above is on homo-aggregation process meaning that aggregates are formed through the collision between identical particles. However, systematic experiments of hetero-aggregation between different particles are still lacking, yet practically important. In the recent study, Lin *et al.* have reported the measured Brownian hetero-aggregation rates between oppositely-charged particles as a function of pH and KCl concentration[42]. They have shown the increase in hetero-aggregation rates with decreasing salt concentration due to electrostatic attraction and the agreements between experiments and DLVO theory. More recently, Cao *et al.* have measured the hetero-aggregation rates between oppositely-charged particles in the

presence of multivalent ions[43]. They reported that the aggregation is slower for hetero-aggregation than homo-aggregation in the range of salt concentration where one of two different particles undergoes a charge reversal. That is attributed to the stronger repulsion between charge reversed particles with weak-charge and highly-charged non-reversed ones than the repulsion for the charge-reversed particles. Yet, no one has known if these observations hold even on other systems such as focusing on ion specific effects[44, 45].

For shear hetero-aggregation, the previous works have calculated the hetero-aggregation for oppositely-charged particles in a simple shear flow[46, 47] and have applied it for the corresponding experimental data in a turbulent flow[48]. They have reported the qualitatively similar trends: the increase in the turbulent hetero-aggregation rates between oppositely-charged particles is observed with decreasing KCl concentration as reported in the case of Brownian aggregation. In addition, Yamauchi *et al.*[49] has reported the measured results of the turbulent hetero-aggregation rates for oppositely-charged and unequal-sized particles as a function of particle size ratio with the analysis using the corresponding correlation equation in a simple shear flow without the electrostatic forces proposed by Han and Lawler[50]. They have observed the substantial quantitative discrepancy between the experimental and calculated values, showing that the experiments are approximately constant with decreasing the size ratio, while the calculations largely decrease down to more than 1000 times smaller than the experimental data. However, the explanation to the discrepancy still remains unresolved.

To unveil the issues given above, we have extensively investigated the charging and aggregation behaviors of model colloidal particles. First, we focus on the effect of electrostatic repulsion on aggregation in a shear flow with its analysis. Second, we study the charging behavior of model colloid experiencing charge reversal induced by the adsorption of hydrophobic ions. Third, the charge reversal effects on homo- and hetero-Brownian aggregation rates are examined by the measurements and its analysis based on DLVO theory. Finally, the understanding of hetero-aggregation is complemented by analyzing the flow type effects on the turbulent hetero-aggregation for unequal-sized particles as a function of particle size ratio.

1.2 Outline of this thesis

This thesis consists of 8 chapters with the four research topics that will be introduced from Chapter 4 to Chapter 7, which are preceded by Chapter 1 general introduction and Chapters 2 and 3 for summarizing fundamental theories used here. In the last Chapter 8, the summary of this thesis is given.

First of all, we have already mentioned the backgrounds and objectives of this thesis in this Chapter 1. In Chapter 2, we briefly summarize the DLVO theory with some theoretical expressions used in this thesis. In Chapter 3, we explain the fundamentals on electrophoresis and aggregation kinetics. Then, by using these theories, we analyze the charging behavior for model colloidal particles and its aggregation kinetics in a simple shear flow in Chapter 4. Furthermore, we apply a simple charging model to analyze the measured data of electrophoretic mobilities in the presence of hydrophobic monovalent ions which induce a charge reversal in Chapter 5. Then, in Chapter 6, to clarify effects of charge reversal on aggregation, we examine anion specific effects on Brownian homo- and hetero-aggregation rates with charge reversal. In order to better understand the flow effects on hetero-aggregation, Chapter 7 deals with the analysis of turbulent hetero-aggregation for unequal-sized particles by using the calculations in two different types of flow. Finally, the obtained results from Chapter 4 to Chapter 7 are summarized as the concluding remarks of this thesis in Chapter 8.

Chapter 2

Fundamental theory on colloidal interactions - DLVO theory -

2.1 Introduction

In our daily life including food processing, paintings, cosmetics, and water purification, we need to control the colloidal suspensions to be quickly aggregated or dispersed by controlling the mutual interactions between particles. The fundamental interaction is given by the balance of the van der Waals attraction, which universally acts between particles, and electrostatic repulsion originated from particle surface charges. The theory describing the interaction was established by Derjaguin, Landau[4], Verwey, and Overbeek[5]. After these researchers, it is now widely accepted as DLVO theory. In this theory, charged surfaces develop the ionic atmosphere around them by accumulating counter ions with Coulombic forces. This is called the electrical double layer (EDL). Overlapping of the electrical double layers results in local increase of disjoining pressures and electrostatic repulsion between the surfaces.

In this chapter, we summarize the potential distribution near an isolated plate as a typical example. We also briefly explain the framework of van der Waals attraction originated from molecular dispersion forces and the electrostatic repulsion between plates

with the Derjaguin approximation as described below.

2.2 Potential distribution near an isolated plate

In general, colloidal particles are charged in the nature, for instance, by dissociation reaction of surface functional groups such as carboxylic group, and/or isomorphous replacement in clay minerals. Since the charging by dissociation reaction depends on chemical compositions in suspended solutions such as pH and salt concentration, it is called variable charges. In the case of isomorphous replacement, for example, by replacing Si with valence electron number 4 in Si tetrahedron with Al whose valence electron number is 3 smaller than that of Si, the clay minerals acquire negative charges to remain electrical neutrality. In this case, the charge amounts of the minerals do not change with the chemical conditions in solutions. This is thus called permanent charges. With these charging mechanisms, colloids bear charges on their surfaces, and induce the electrostatic repulsion between them. Such electrostatic repulsion increases with charge amounts on the particles and decrease with increasing salt concentration by electrical screening due to the compression of electrical double layer. Because of the screening of long-ranged forces by ions, the electrical repulsion decays exponentially with surface separation distance. These effects are included in diffuse electrical double layer theory or DLVO theory[4, 5]. First of all, as a basics, let us consider about potential distribution near an isolated plate.

2.2.1 Poisson-Boltzmann equation

Let us consider a plate which has charges on the surface adjacent to an electrolyte solution. Such charged plate attracts ions with the opposite sign of the charge respect to the surface, so-called counter ions, to the surface via Coulombic attraction. Meanwhile, the ions tend to spread diffusively due to their thermal motion, in other words, diffusional force which can be described as osmotic pressure difference due to concentration gradient as shown in **Fig. 2.2.1**. At equilibrium state, the ionic distribution around the charged surface is determined by the balance between the electrical force and the diffusional force. By neglecting ion-ion interactions, the ionic concentration

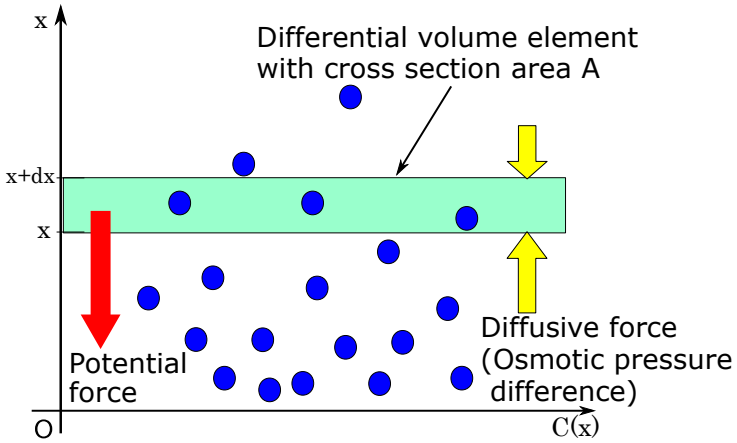

Figure 2.2.1: Schematic view of the boltzmann distribution balancing between diffusion and potential force

distribution follows the Boltzmann distribution as

$$C_i(x) = C_{i,b} \exp\left(-\frac{z_i e \psi(x)}{k_B T}\right), \tag{2.2.1}$$

where $C_i(x)$ is the concentration of certain ionic species i with the valence of z_i at the position x from the surface, $C_{i,b}$ is its bulk concentration, e is the elementary charge, $\psi(x)$ is the electrical potential at the position x, k_B is the Boltzmann constant, T is the absolute temperature.

From the Maxwell equation in matter, the relationship between divergence of electric field and charge distribution in space, so-called Gauss's law is given by the following equation

$$\nabla \cdot \boldsymbol{E} = \frac{\rho_e}{\epsilon_r \epsilon_0}, \tag{2.2.2}$$

where $\boldsymbol{E}$ is the electric field, ρ_e is the volume charge density, ϵ_r is the relative dielectric constant of the medium, and ϵ_0 is the dielectric constant of the vacuum. Here, we put the relationship between electrical potential and field in electrostatics Eq.(2.2.3) into Eq.(2.2.2)

$$\boldsymbol{E} = -\nabla \psi. \tag{2.2.3}$$

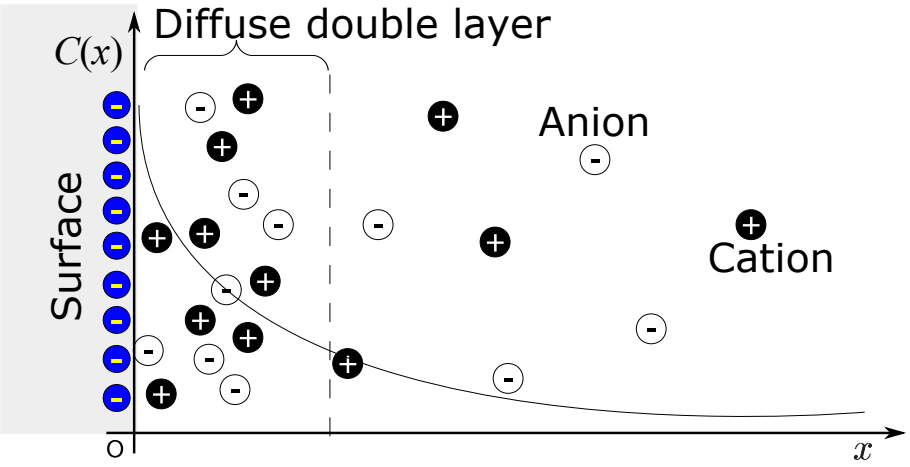

Figure 2.2.2: Schematic view of the electrical double layer adjacent to an isolated charged plate.

One obtains Poisson's equation giving the relationship between the electrical potential and the volume charge density as

$$\nabla^2\psi = -\frac{\rho_e}{\epsilon_r\epsilon_0}. \tag{2.2.4}$$

Now, let us assume that the isolated plate is covered with uniform charge density. It allows us to consider that the electrical potential is a function of the position x from the surface. With this assumption, Poisson's equation (Eq.(2.2.4)) is reduced to one-dimensional equation as follows:

$$\frac{d^2\psi}{dx^2} = -\frac{\rho_e}{\epsilon_r\epsilon_0}. \tag{2.2.5}$$

In an electrolyte solution adjacent to an isolated charged surface, the charge distribution is determined by the composition of ions distributed (**Fig. 2.2.2**) as described by Eq.(2.2.1).

$$\rho_e = \sum_i z_i e C_i(x). \tag{2.2.6}$$

Therefore, substituting Eqs.(2.2.1) and (2.2.6) into Eq.(2.2.5), we can obtain the following equation

$$\frac{d^2\psi}{dx^2} = -\frac{e}{\epsilon_r\epsilon_0}\sum_i z_i C_{i,b}\exp\left(-\frac{z_i e\psi(x)}{k_B T}\right). \tag{2.2.7}$$

Eq.(2.2.7) is called the Poisson-Boltzmann (PB) equation, which is a non-linear second-order differential equation. Equation (2.2.7) is a governing equation for the electrical potential distribution near charged surfaces in the electrolyte solution.

For low electrical potential case of Eq.(2.2.7), $\left|\frac{z_i e\psi(x)}{k_B T}\right| \ll 1$, we can use the Taylor expansion to linearize Eq.(2.2.7), so-called Debye-Hückel (DH) approximation. With the DH approximation and electrical neutrality $\sum_i z_i e C_i = 0$, one obtains the following equation:

$$\frac{d^2\psi}{dx^2} = \kappa^2 \psi, \tag{2.2.8}$$

where κ is the Debye parameter given by

$$\kappa = \left(\frac{1}{\epsilon_r \epsilon_0 k_B T} \sum_i z_i^2 e^2 C_{i,b} \right)^{\frac{1}{2}}. \tag{2.2.9}$$

Its inverse κ^{-1} has the dimension of length. It is therefore called the Debye length characterizing the measure of thickness of the electrical double layer. For an isolated charged plate, the boundary condition for Eq.(2.2.8) is described by

$$\begin{aligned} \psi(x)\big|_{x=0} &= \psi_0, \\ \frac{d\psi}{dx}\Big|_{x\to\infty} &= 0, \end{aligned} \tag{2.2.10}$$

where ψ_0 is the surface potential of the isolated surface. Then, the solution of Eq.(2.2.8) is given by the following equation

$$\psi(x) = \psi_0 \exp(-\kappa x). \tag{2.2.11}$$

Eq.(2.2.11) indicates that the Debye length means the characteristic decay length of electrical potential in low potential case.

For symmetric (z:z type) electrolyte solution containing ions with the same valence of z in opposite sign of charges, we can derive an analytical solution for Eq.(2.2.7) without the liner approximation with the boundary condition Eq.(2.2.10) as

$$\psi(x) = \frac{4k_B T}{ze} \tanh^{-1}\left[\tanh\left(\frac{ze\psi_0}{4k_B T} \right) \exp(-\kappa x) \right]. \tag{2.2.12}$$

Eq.(2.2.12) is called the Gouy-Chapman equation. Eq.(2.2.7) for symmetric electrolyte solution case can be easily integrated once to obtain the potential gradient as

$$\frac{d\psi(x)}{dx} = -\left(\frac{8C_b k_B T}{\epsilon_r \epsilon_0}\right)^{\frac{1}{2}} \sinh\left(\frac{ze\psi(x)}{2k_B T}\right). \tag{2.2.13}$$

By taking the volume integral of Gauss's law for a closed space V, we have

$$\int_V \nabla \cdot \boldsymbol{E} dV = \frac{1}{\epsilon_r \epsilon_0} \int_V \rho_e dV. \tag{2.2.14}$$

Applying Gauss's divergence theorem on the left side, one can obtain

$$\int_S \boldsymbol{E} \cdot \boldsymbol{n} dS = \frac{1}{\epsilon_r \epsilon_0} \int_V \rho_e dV. \tag{2.2.15}$$

Now, we set the closed space V so that it has the surface S which is always parallel to the charged plate. With this assumption, the electric field induced by the charged plate is also perpendicular to the surface S. Then, we have $\boldsymbol{E} \cdot \boldsymbol{n} = E_n$ where E_n is the normal component of the electric field on the surface S. In this one-dimensional case, $E_n = -\frac{d\psi}{dx}\big|_{x=0}$. The volume integral on the right side means the total charge Q inside the surface S. Thus, by setting the cross section in the closed volume V parallel to the charged plate as A, we can obtain the following equation

$$-\left.\frac{d\psi}{dx}\right|_{x=0} A = \frac{Q}{\epsilon_r \epsilon_0},$$

where $\int_S dS = A$. In the above equation, defining the surface charge density σ as $\sigma = Q/A$, we obtain

$$\sigma = -\epsilon_r \epsilon_0 \left.\frac{d\psi}{dx}\right|_{x=0}. \tag{2.2.16}$$

Then, substituting Eq.(2.2.13) with the boundary condition Eq.(2.2.10) into Eq.(2.2.16), we obtain

$$\sigma = (8\epsilon_r \epsilon_0 C_b k_B T)^{\frac{1}{2}} \sinh\left(\frac{ze\psi_0}{2k_B T}\right) = \frac{2\epsilon_r \epsilon_0 \kappa k_B T}{ze} \sinh\left(\frac{ze\psi_0}{2k_B T}\right), \tag{2.2.17}$$

where we use the definition of the Debye parameter Eq.(2.2.9). Eq.(2.2.17) is the relationship between surface potential ψ_0 and charge density σ for symmetrical electrolyte solution, especially, for monovalent salt, it is called the Grahame equation.

2.3 Van der Waals attraction

The van der Waals force universally acts between particles. Several types of van der Waals forces are based on different origins but are essentially electrical interactions originated from the interactions between permanent and/or instantaneously induced dipoles of polar/non-polar molecules. Therefore, the exact treatment of van der Waals forces requires the knowledge of quantum mechanics. According to the form of its interactions, the van der Waals forces can be categorized to three types, namely, the Keesom interaction(dipole-dipole), the Debye interaction(dipole-induced dipole), and the London interaction(induced dipole-induced dipole). These categories mean orientation, induction, and dispersion forces, respectively[51]. First, without going to such exact treatments, we just show the intermolucular potential is inversely proportional to the sixth power of the distance as the common property of the van der Waals forces by considering the dipole-dipole interaction.

Let us consider the electrostatic potential $\psi(r)$ generated by an electrical dipole (**Fig. 2.3.1**). With the linearity of Maxwell's equation, generally, the electrostatic potential induced at the distance r can be expressed by the superposition of the potential by the two point charges. From Coulomb's law, the electrostatic potential generated by the

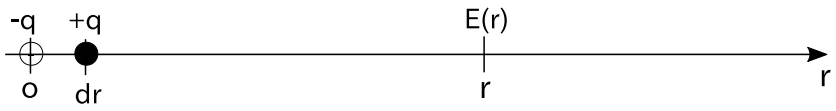

Figure 2.3.1: Schematic representation of the electrical dipole with an induced electric field.

two point charges is given by

$$\begin{aligned}\psi(r) &= \frac{-q}{4\pi\epsilon_r\epsilon_0 r} + \frac{+q}{4\pi\epsilon_r\epsilon_0(r-dr)} \\ &= \frac{q}{4\pi\epsilon_r\epsilon_0} r^{-1}\left[\left(1-\frac{dr}{r}\right)^{-1} - 1\right]. \end{aligned} \tag{2.3.1}$$

If dr is so small that $\frac{dr}{r} \ll 1$ and $(1-dr/r)^{-1} \approx 1 + dr/r$ with linear approximation, we have

$$\psi(r) \approx \frac{q}{4\pi\epsilon_r\epsilon_0} r^{-1}\left[1+\frac{dr}{r}-1\right] = \frac{qdr}{4\pi\epsilon_r\epsilon_0 r^2} = \frac{p}{4\pi\epsilon_r\epsilon_0 r^2} \tag{2.3.2}$$

where $p = qdr$ is the magnitude of the dipole moment.

With the above result, we calculate the electrostatic energy U of the dipole when it is moved from infinity to the position r as shown in **Fig. 2.3.2** (a). U_A is given by the product of the charge and potential

$$\begin{aligned} U_A &= q_1\psi(r+dr) - q_1\psi(r) \\ &= q_1\psi(r) + q_1\frac{d\psi}{dr}dr - q_1\psi(r) = q_1\frac{d\psi}{dr}dr, \end{aligned}$$

where we use the linear approximation as dr is small enough. With $E(r) = -\frac{d\psi}{dr}$,

$$U_A = -q_1 dr E(r) = -p_1 E(r) = -\frac{p_1 p_2}{2\pi\epsilon_r\epsilon_0 r^3}, \tag{2.3.3}$$

where $p_1 = q_1 dr$ in Eq.(**??**), and $p = p_2$ in Eq.(2.3.2) are used. Note that the sign of the case in **Fig. 2.3.2** (b) is reversed as $U_B = -U_A$.

Now, let us consider the cases where the dipoles are aligned in one dimension as depicted in **Fig. 2.3.2**. We assume that the existence probabilities of the two states in **Fig. 2.3.2** (a,b) follow the Boltzmann distribution. With the linear approximation, we can obtain

$$\exp\left(-\frac{U_A}{k_B T}\right) \approx 1 - \frac{U_A}{k_B T}\ , \quad \exp\left(-\frac{U_B}{k_B T}\right) \approx 1 - \frac{U_B}{k_B T}.$$

The averaged interaction energy U can be approximately expressed as the sum of products of the probability that each state can be taken and its realized value as

$$U \approx \left(1 - \frac{U_A}{k_B T}\right) U_A + \left(1 - \frac{U_B}{k_B T}\right) U_B = -\frac{2U_B^2}{k_B T} = -\frac{2p_1^2 p_2^2}{4\pi^2 e_r e_0 k_B T} \frac{1}{r^6},$$

where we use the fact that $U_B = -U_A$. Therefore, by defining the proportional coefficient λ, one obtains the common property of the van der Waals forces as

$$U = -\frac{\lambda}{r^6}. \tag{2.3.4}$$

With this equation, we can see that the molecular forces are short-ranged. In this thesis, since we usually treat the van der Waals forces between the macro-bodies composed of same materials, it is always attractive. However, in general, according to the Lifshitz theory[52], the Hamaker constant, which is a measure of the magnitude of the van der Waals forces, can be both positive and negative depending on the combination of materials and media. Therefore, the van der Waals forces for macro-bodies can be both attractive and repulsive.

2.3.1 Van der Waals attraction between two plates

In the previous section, inter-molecular van der Waals attraction is shown to be short-range forces $\propto -1/r^6$ described in Eq.(2.3.4). Based on Eq.(2.3.4) with the additivity assumption, the van der Waals attraction between macro-bodies can be long-range

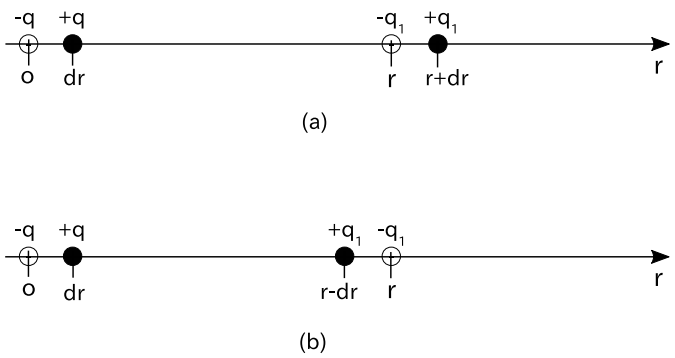

Figure 2.3.2: Another electrical dipole in the electric field induced by the electrical dipole around the Origin O: dipole moment (a) in the same direcion and (b) in the opposite direction.

forces[53].

First, let us start to calculate the van der Waals attraction between a molucule and an infinite plate as shown in **Fig. 2.3.3**. We set the x-axis normal to the plate surface, and put a molecule 1 at the origin with the separation distance h (**Fig. 2.3.3** (a)). We consider a circular ring with the inner and outer radii of r and $r+dr$, and the thickness of dx inside the plate as in **Fig. 2.3.3** (b). From the Pythagorean theorem with small dr and dx, the molecule 1 and all molecules in the ring are at the equal distance with $(r^2+x^2)^{\frac{1}{2}}$. With Eq.(2.3.4), the van der Waals attractive potential between the molecule at the origin and one in the ring can be expressed by

$$-\frac{\lambda}{(r^2+x^2)^{\frac{6}{2}}} = -\frac{\lambda}{(r^2+x^2)^3}. \tag{2.3.5}$$

Since the volume of the ring is $2\pi r dr dx$, the total number of molecules in the ring is given by $2N\pi r dr dx$ where N is the volume density of molecules in the plate. These all molecules of $2N\pi r dr dx$ equally interact with the molecule 1 by the van der Waals attraction, hence, the summation of their interactions represents the van der Waals potential between the molecule 1 and the ring as

$$-\frac{\lambda N 2\pi r dr dx}{(r^2+x^2)^3}. \tag{2.3.6}$$

The interaction $V(h)$ between the molecule 1 and the infinite plate can be derived by integrating with the ranges of $0<r<\infty$ and $h<x<\infty$, that is,

$$V(h) = -\int_h^\infty dx \int_0^\infty dr \frac{\lambda N 2\pi r}{(r^2+x^2)^3}. \tag{2.3.7}$$

Changing the variable $r = x\tan\theta$ and $dr = \frac{x}{\cos^2\theta}d\theta$ with the integration interval of $0<x<\infty \rightarrow 0<\theta<\pi/2$, we have

$$\begin{aligned} V(h) &= -\lambda N 2\pi \int_h^\infty dx \int_0^{\frac{\pi}{2}} d\theta \frac{x}{\cos^2\theta} \frac{x\tan\theta}{x^6(1+\tan^2\theta)^3} \\ &= -\lambda N 2\pi \int_h^\infty dx \int_0^{\frac{\pi}{2}} d\theta \frac{x^2\tan\theta}{x^6\cos^2\theta}\cos^6\theta \\ &= -\lambda N 2\pi \int_h^\infty dx \int_0^{\frac{\pi}{2}} d\theta \frac{\sin\theta\cos^3\theta}{x^4} \end{aligned}$$

$$
\begin{aligned}
&= -\lambda N 2\pi \int_h^\infty \frac{dx}{x^4} \int_0^{\frac{\pi}{2}} d\theta \frac{d}{d\theta} \left(\frac{-\cos^4\theta}{4} \right) \\
&= -\lambda N 2\pi \int_h^\infty \frac{dx}{x^4} \left[-\frac{\cos^4\theta}{4} \right]_0^{\frac{\pi}{2}} \\
&= -\lambda N 2\pi \int_h^\infty \frac{dx}{4x^4} \\
&= -\lambda N 2\pi \int_h^\infty \frac{dx}{4x^4} \\
&= -\lambda N 2\pi \left[-\frac{dx}{12x^3} \right]_h^\infty \\
&= -\frac{\lambda N \pi}{6h^3}.
\end{aligned} \tag{2.3.8}
$$

Next, with Eq.(2.3.8), we can calculate the van der Waals potential between infinite plates as shown in **Fig. 2.3.4**. In this case, we put the surface of the infinite plate 1 at the origin and the infinite plate 2 at the surface separation distance of $x = h$. The interaction between the molecules constituting the infinite plate 2 at $x > h$ and the infinite plate 1 is equal to the case when $h \to x$ in Eq.(2.3.8). Let us set the circular disc with the area of S and the thickness of dx parallel to the infinite plates at the position

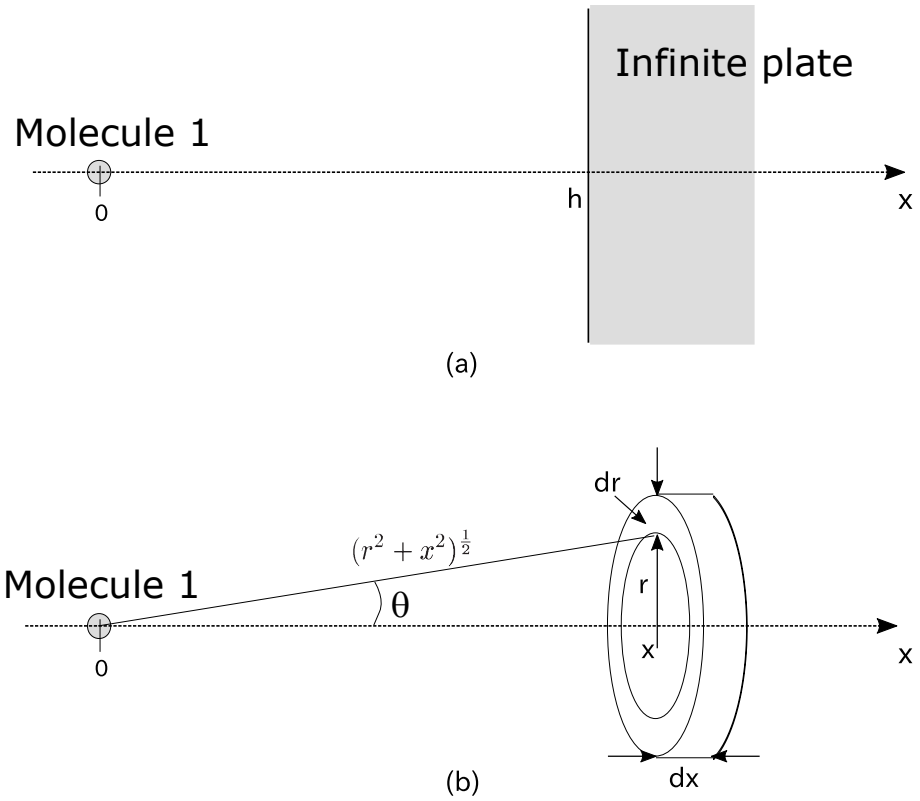

Figure 2.3.3: Interaction between an infinite plate and a molecule: interaction between a molecule and (a) an infinite plate, (b) a circular ring in the infinite plate.

x satisfying $x > h$ as depicted in **Fig. 2.3.4**. Since the volume of the disc is Sdx, the total number of molecules in the disc is expressed by $NSdx$. All the molecules in the disc interact with the infinite plate 1 by the van der Waals attraction in Eq.(2.3.8), thus, we have the following equation by taking the summation of all these interactions

$$-\frac{\lambda N^2 \pi S dx}{6x^3}. \tag{2.3.9}$$

By integrating Eq.(2.3.9) with the range of $h < x < \infty$, we can obtain the van der Waals attractive potential between the infinite plate 1 and the infinitely thick disc with the area of S, that is,

$$-\frac{\lambda N^2 \pi S}{6}\int_h^\infty \frac{dx}{x^3} = -\frac{\lambda N^2 \pi S}{6}\left[-\frac{1}{2x^2}\right]_h^\infty = -\frac{\lambda N^2 \pi S}{12h^2}. \tag{2.3.10}$$

Dividing Eq.(2.3.10) by S, we obtain the van der Waals attractive potential between infinite plates per unit area $V_{vdW}^P(h)$ as follows

$$V_{vdW}^P(h) = -\frac{A_{\mathrm{H}}}{12\pi h^2}, \tag{2.3.11}$$

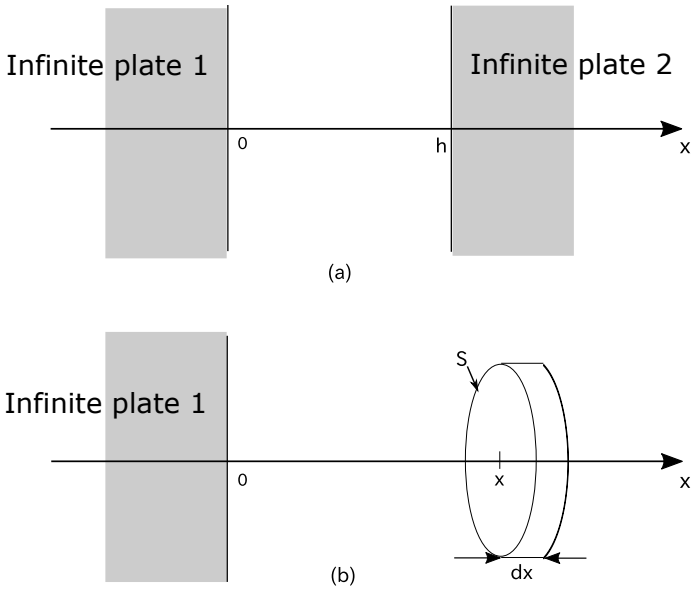

Figure 2.3.4: Interaction between infinte plates: interaction between an infinite plate and (a) another infinite plate, (b) a circular plate parallel to infinite plates.

where we define $A_{\mathrm{H}} = \lambda N^2 \pi^2$ and A_{H} is the Hamaker constant having the dimension of energy $[ML^2T^{-2}]$ and characterizes the magnitude of the van der Waals attraction. Although the value of Hamaker constant can be calculated by the Lifshitz theory[52], it is often treated as an experimental parameter. From Eq.(2.3.11), the van der Waals attraction between macro-bodies such as the plates is a long-range potential proportional to h^{-2}.

2.3.2 Derjaguin approximation

With Eq.(2.3.11), we can estimate the van der Waals potential energy per unit area between two plates. However, such equation can not be directly used to, for example, spherical particles. To overcome this, Derjaguin developed the method to calculate the mutual interaction between particles from the result in plate-plate configuration. This is called the Derjaguin approximation[54]. In this method, first, one divides the sphere surfaces into parallel rings whose centers are on the line connecting the centers of the two spheres as shown in **Fig. 2.3.5**, and approximates the inter-particle interaction as the summation of the plate-plate interaction between the opposed rings on the surfaces of two spheres over the whole spheres. It neglects the interaction with others than the opposed rings.

Let us set the plate-plate interaction (force, potential energy) $f^P(H)$ with the plate-plate separation distance H, and consider the inter-particle interaction between two spheres with the radii of R_1, R_2 (**Fig. 2.3.5**). If the particle separation distance h is small so that $h \ll R_1$ and $h \ll R_2$, the inter-particle interaction can be approximated by summing up the interaction between the rings with the area of $2\pi y dy$ on each spheres.

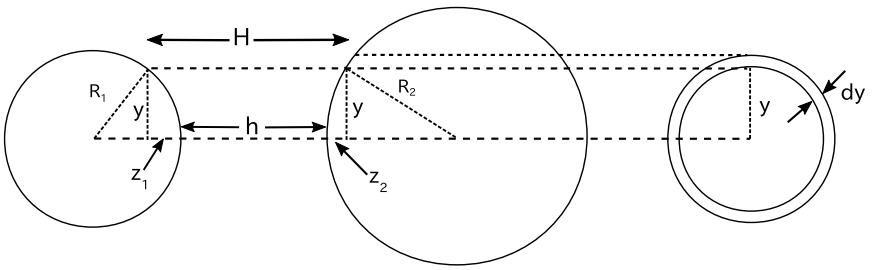

Figure 2.3.5: Schematic representation of the Derjaguin approximation: inter-particle interaction as a summation of inter-circular ring interaction.

Here, we set the separation distances between each opposed rings $H = h + z_1 + z_2$ and set the inter-particle interaction to $f^S(h)$:

$$f^S(h) = \int_{H=h}^{H\to\infty} f^P(H) 2\pi y dy. \tag{2.3.12}$$

This equation conventionally takes the summation from the particle separation h to ∞, since the radii of rings change with the distances H. It is analytically useful because it can take the limit of infinity including about all possible ring radius. The distance H can be known with z_1 and z_2 calculated by the particle distance and the Pythagorean theorem as

$$\begin{aligned} H &= h + z_1 + z_2 \\ &= h + R_1 - (R_1^2 - y^2)^{\frac{1}{2}} + R_2 - (R_2^2 - y^2)^{\frac{1}{2}} \\ &= h + R_1 \left[1 - \left\{ 1 - \left(\frac{y}{R_1} \right)^2 \right\}^{\frac{1}{2}} \right] + R_2 \left[1 - \left\{ 1 - \left(\frac{y}{R_2} \right)^2 \right\}^{\frac{1}{2}} \right]. \end{aligned}$$

With assuming only part of spheres near the closest surfaces contributes to the inter-particle interaction and being $\frac{y}{R_1}, \frac{y}{R_2} \ll 1$, the bracket terms in the above equation can be rewritten by linear approximation as

$$\left\{ 1 - \left(\frac{y}{R_1} \right)^2 \right\}^{\frac{1}{2}} \approx 1 + \frac{1}{2} \left(\frac{y}{R_1} \right)^2, \ \left\{ 1 - \left(\frac{y}{R_2} \right)^2 \right\}^{\frac{1}{2}} \approx 1 + \frac{1}{2} \left(\frac{y}{R_2} \right)^2.$$

Then, we have

$$H \approx h + \frac{1}{2} \frac{y^2}{R_1} + \frac{1}{2} \frac{y^2}{R_2}.$$

Differentiating this equation respect to y, one obtains

$$dH \approx \left(\frac{1}{R_1} + \frac{1}{R_2} \right) y dy.$$

Finally, substituting this equation into the integral in Eq.(2.3.12)

$$f^S(h) = \frac{2\pi R_1 R_2}{R_1 + R_2} \int_h^\infty f^P(H) dH. \tag{2.3.13}$$

Eq.(2.3.13) is called the Derjaguin approximation. With Eq.(2.3.13), we can calculate the inter-particle force $F^S(h)$ to substitute the force per unit area between flat plates $F^P(H)$ as

$$F^S(h) = \frac{2\pi R_1 R_2}{R_1 + R_2} \int_h^\infty F^P(H) dH.$$

The integral on the right hand side is equal to the potential energy per unit area between the plates $V^P(h)$ and can be rewritten as the relationship between $F^S(h)$ and $V^P(h)$ below

$$F^S(h) = \frac{2\pi R_1 R_2}{R_1 + R_2} \int_h^\infty F^P(H) dH = \frac{2\pi R_1 R_2}{R_1 + R_2} V^P(h). \tag{2.3.14}$$

Eq.(2.3.14) is the original form presented in the paper by Derjaguin in 1934[54, 22]. In general, a conservative force satisfies the following relationship with the potential energy as

$$F^S(h) = -\frac{dV^S}{dh}. \tag{2.3.15}$$

By integrating Eq.(2.3.15), we can calculate the potential energy between two spheres as follows

$$V^S(h) = \int_h^\infty F^S(h) dh. \tag{2.3.16}$$

Therefore, with the Derjaguin approximation, if we know the force per unit area between parallel plates, we can calculate the inter-particle force by Eq.(2.3.14). From Eq.(2.3.15), we can construct the inter-particle potential energy Eq.(2.3.16). By substituting Eq.(2.3.14) into Eq.(2.3.16), this can be rewritten as

$$V^S(h) = \frac{2\pi R_1 R_2}{R_1 + R_2} \int_h^\infty V^P(H) dH. \tag{2.3.17}$$

We often use this Derjaguin approximation to calculate the van der Waals attractive and electrostatic repulsive forces/potential energies in following sections.

2.3.3 Van der Waals attraction for sphere-sphere interaction using Derjaguin approximation

Using the Derjaguin approximation Eq.(2.3.13) to Eq.(2.3.11), we can obtain the van der Waals attractive potential between two spherical particles $V_{vdW}^{S}(h)$ as

$$\begin{aligned} V_{vdW}^{S}(h) &= \frac{2\pi R_1 R_2}{R_1 + R_2} \int_h^\infty V^P(H) dH \\ &= -\frac{R_1 R_2 A}{6(R_1 + R_2)h}, \end{aligned} \tag{2.3.18}$$

where H is the plate-plate separation distance, and h is the closest distance between spheres. Especially, for equal-sized particles with the radius of R, Eq.(2.3.18) reduces to

$$V_{vdW}^{S}(h) = -\frac{A_{\mathrm{H}} R}{12h}. \tag{2.3.19}$$

2.3.4 Van der Waals attraction between spheres without Derjaguin approximation

With the additivity assumption, Bradley calculated the London van der Waals attractive potential for spherical particles in the case of small particle-particle distances[55]. His calculation has been modified by correcting the small distance approximation and the matter that is not symmetrical in the radial direction of two spherical particles by Hamaker[56]. Now, it is called the Hamaker summation which gives the London van der Waals attraction for spherical particles without the Derjaguin approximation as described later.

As we see in the previous section, the van der Waals potential can be written as the volume integral on each spheres

$$V^S = -\int_{V_1} dV_1 \int_{V_2} dV_2 \frac{N^2 \lambda}{r^6}, \tag{2.3.20}$$

where V is the particle volume, and dV is the volume element. Indices 1 and 2 denote

the properties of each particles 1 and 2, and r is the distance between dV_1 and dV_2. Let us consider the spherical particle 1 with the radius of R_1 as shown in **Fig. 2.3.6**. By taking its center as O and a point P outside the sphere 1 with the length of $|OP| = R$, the surface of a sphere with the radius of r around P cut out the surface $S(ABC)$ from the sphere 1 around O in **Fig. 2.3.6**. Considering the surface integration on $S(ABC)$ in spherical coordinates with the fact that the arc lengths of the surface elements on $S(ABC)$ are $rd\theta$ in θ direction and $r\sin\theta d\phi$ in ϕ direction, we can calculate $S(ABC)$ by integrating the product of these arc lengths in the ranges of $0 < \phi < 2\pi,\ 0 < \theta < \theta_0$. That is,

$$S(ABC) = \int_0^{2\pi} d\phi \int_0^{\theta_0} r^2 \sin\theta d\theta. \tag{2.3.21}$$

Since θ_0 takes the value of $0 < \theta_0 < \frac{\pi}{2}$, we can obtain the following relationship using the law of cosines

$$R_1^2 = R^2 + r^2 - 2rRcos\theta_0. \tag{2.3.22}$$

Therefore, performing the integration in Eq.(2.3.21), we have

$$\begin{aligned} S(ABC) &= \int_0^{2\pi} d\phi \int_0^{\theta_0} r^2 \sin\theta \\ &= 2\pi r^2 \left[-\cos\theta\right]_0^{\theta_0} \\ &= 2\pi r^2 \left[-\cos\theta_0 + 1\right]. \end{aligned}$$

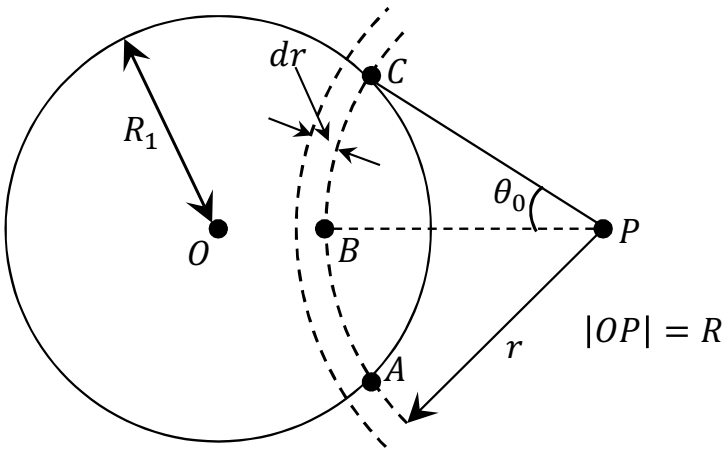

Figure 2.3.6: Interaction between a molecule and cut surfaces in a particle.

Using Eq.(2.3.22) leads to

$$S(ABC) = 2\pi r^2 \left[\frac{R_1^2 - R^2 - r^2}{2rR} + 1\right] = \pi \frac{r}{R}\left[R_1^2 - (R-r)^2\right]. \tag{2.3.23}$$

By multiplying Eq.(2.3.23) by dr, we obtain the volume between broken lines at r and $r + dr$. With the number of molecules in $S(ABC)dr$ given by $NS(ABC)dr$, the van der Walls potential between a molecule at the point P and the sphere 1, V_P, can be calculated by integrating the product of Eq.(2.3.23) and Eq.(2.3.4) with the range of $R - R_1 < r < R + R_1$ as

$$V_P = -\int_{R-R_1}^{R+R_1} \frac{\lambda N}{r^6} \pi \frac{r}{R}\left[R_1^2 - (R-r)^2\right] dr. \tag{2.3.24}$$

To calculate the van der Waals potential between two spheres, we put the sphere 2 at O_2 so that the center distance of the sphere 1 and 2 is $|O_1O_2| = C$ as shown in **Fig. 2.3.7**. Eq.(2.3.24) gives the van der Waals potential between the sphere 1 around O_1 and the molecules in the volume element between broken lines on the distances of R and $R+dR$ in the sphere 2. Therefore, its integration over the whole sphere ($C-R_2 < R < C+R_2$) provides the van der Waals potential between the two spheres $V_{vdW}^S(h)$, that is,

$$V_{vdW}^S(h) = \int_{C-R_2}^{C+R_2} V_P N \pi \frac{R}{C}\left[R_2^2 - (C-R)^2\right] dR.$$

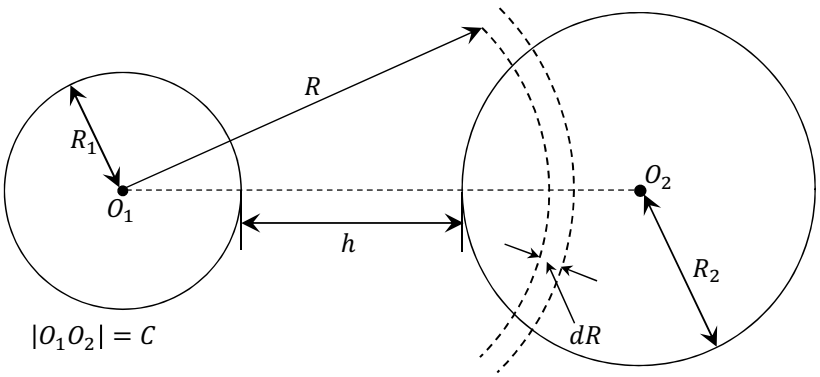

Figure 2.3.7: Interaction between a particle and cut surfaces in another particle.

By substituting Eq.(2.3.24) into this equation, we have

$$V_{vdW}^{S}(h) = -\frac{\lambda N^2\pi^2}{C}\int_{C-R_2}^{C+R_2}\left[R_2^2-(C-R)^2\right]dR\int_{R-R_1}^{R+R_1}\frac{1}{r^5}\left[R_1^2-(R-r)^2\right]dr.$$

We can perform the partial integral respect to r as:

$$\begin{aligned}
\int_{R-R_1}^{R+R_1}\frac{1}{r^5}\left[R_1^2-(R-r)^2\right]dr &= \left[\frac{-1}{4r^4}\{R_1^2-(R-r)^2\}\right]_{R-R_1}^{R+R_1}+\int_{R-R_1}^{R+R_1}\frac{1}{4r^4}2(R-r)dr\\
&= \int_{R-R_1}^{R+R_1}\frac{R}{2r^4}dr-\int_{R-R_1}^{R+R_1}\frac{1}{2r^3}dr\\
&= \left[-\frac{R}{6r^3}\right]_{R-R_1}^{R+R_1}-\left[-\frac{R}{4r^2}\right]_{R-R_1}^{R+R_1}\\
&= -\frac{R}{6(R+R_1)^3}+\frac{R}{6(R-R_1)^3}+\frac{1}{4(R+R_1)^2}-\frac{1}{4(R-R_1)^2}\\
&= \frac{1}{12}\left\{-\frac{2R}{(R+R_1)^3}+\frac{2R}{(R-R_1)^3}+\frac{3}{(R+R_1)^2}-\frac{3}{(R+R_1)^2}\right\}\\
&= \frac{1}{12}\Bigg\{-\frac{2(R+R_1)-2R_1}{(R+R_1)^3}+\frac{2(R-R_1)+2R_1}{(R-R_1)^3}\\
&\quad +\frac{3}{(R+R_1)^2}-\frac{3}{(R+R_1)^2}\Bigg\}\\
&= \frac{1}{12}\left\{\frac{2R_1}{(R+R_1)^3}+\frac{2R_1}{(R-R_1)^3}+\frac{1}{(R+R_1)^2}-\frac{1}{(R+R_1)^2}\right\}.
\end{aligned}$$

Substituting this to the integral,

$$\begin{aligned}
V_{vdW}^{S}(h) = -\frac{\lambda N^2\pi^2}{C}&\int_{C-R_2}^{C+R_2}\left[R_2^2-(C-R)^2\right]dR\\
&\times\frac{1}{12}\left\{\frac{2R_1}{(R+R_1)^3}+\frac{2R_1}{(R-R_1)^3}+\frac{1}{(R+R_1)^2}-\frac{1}{(R+R_1)^2}\right\}.
\end{aligned}$$

We can calculate each term by using the partial integral. For the first term,

$$\begin{aligned}
\int_{C-R_2}^{C+R_2}\frac{2R_1\{R_2^2-(C-R)^2\}}{(R+R_1)^3}dR &= \left[-\frac{R_1\{R_2^2-(C-R)^2\}}{(R+R_1)^2}\right]_{C-R_2}^{C+R_2}+\int_{C-R_2}^{C+R_2}\frac{2R_1(C-R)}{(R+R_1)^2}dR\\
&= \left[-\frac{2R_1(C-R)}{R+R_1}\right]_{C-R_2}^{C+R_2}-\int_{C-R_2}^{C+R_2}\frac{2R_1}{R+R_1}\\
&= \frac{2R_1R_2}{(C+R_1+R_2)}+\frac{2R_1R_2}{(C+R_1-R_2)}-2R_1\left[\ln(R+R_1)\right]_{C-R_2}^{C+R_2}\\
&= \frac{2R_1R_2}{C+(R_1+R_2)}+\frac{2R_1R_2}{C+(R_1-R_2)}-2R_1\ln\frac{C+R_1+R_2}{C+R_1-R_2}.
\end{aligned}$$

With the similar way, the second term is calculated as

$$\int_{C-R_2}^{C+R_2} \frac{2R_1\{R_2^2-(C-R)^2\}}{(R-R_1)^3}dR = \frac{2R_1R_2}{C-(R_1-R_2)}+\frac{2R_1R_2}{C-(R_1+R_2)}+2R_1\ln\frac{C-(R_1+R_2)}{C-(R_1-R_2)}.$$

For the third term,

$$\begin{aligned}
\int_{C-R_2}^{C+R_2} \frac{\{R_2^2-(C-R)^2\}}{(R+R_1)^2}dR &= \left[-\frac{\{R_2^2-(C-R)^2\}}{R+R_1}\right]_{C-R_2}^{C+R_2} + \int_{C-R_2}^{C+R_2}\frac{2(C-R)}{R+R_1}dR \\
&= [2(C-R)\ln(R+R_1)]_{C-R_2}^{C+R_2} + 2\int_{C-R_2}^{C+R_2}\ln(R+R_1)dR \\
&= [2(C-R)\ln(R+R_1)]_{C-R_2}^{C+R_2} + [2(R+R_1)\ln(R+R_1)]_{C-R_2}^{C+R_2} \\
&\quad -2\int_{C-R_2}^{C+R_2}\frac{R+R_1}{R+R_1}dR \\
&= -2R_2\ln(C+R_1+R_2) - 2R_2\ln(C+R_1-R_2) \\
&\quad +2(C+R_1+R_2)\ln(C+R_1+R_2) \\
&\quad -2(C-R_2+R_1)\ln(C-(R_1+R_2)) - 4R_2 \\
&= 2C\ln\frac{C+R_1+R_2}{C+R_1-R_2} + 2R_1\ln\frac{C+R_1+R_2}{C+R_1-R_2} - 4R_2.
\end{aligned}$$

Similarly, the fourth term is calculated

$$-\int_{C-R_2}^{C+R_2} \frac{\{R_2^2-(C-R)^2\}}{(R+R_1)^2}dR = -2C\ln\frac{C-(R_1-R_2)}{C-(R_1+R_2)}-2R_1\ln\frac{C-(R_1+R_2)}{C-(R_1-R_2)}+4R_2.$$

The summation of these calculated terms is given by the following equation:

$$\begin{aligned}
&\frac{2R_1R_2}{C+(R_1+R_2)}+\frac{2R_1R_2}{C+(R_1-R_2)}+\frac{2R_1R_2}{C-(R_1-R_2)}+\frac{2R_1R_2}{C-(R_1+R_2)} \\
&+2C\ln\frac{(C+R_1+R_2)(C-(R_1+R_2))}{(C+R_1-R_2)(C-(R_1-R_2))} \\
=\ &\frac{4R_1R_2C}{C^2-(R_1+R_2)^2}+\frac{4R_1R_2C}{C^2-(R_1-R_2)^2}+2C\ln\frac{C^2-(R_1+R_2)^2}{C^2-(R_1-R_2)^2}.
\end{aligned}$$

When this integration result is substituted into the original expression, we obtain

$$V_{vdW}^S(h) = -\frac{\lambda N^2\pi^2}{6}\left[\frac{2R_1R_2}{C^2-(R_1+R_2)^2}+\frac{2R_1R_2}{C^2-(R_1-R_2)^2}+\ln\frac{C^2-(R_1+R_2)^2}{C^2-(R_1-R_2)^2}\right]. \tag{2.3.25}$$

To simplify this equation, we introduce some variables. First, the center distance between the two spheres C is given by

$$C = R_1 + R_2 + h, \tag{2.3.26}$$

where h is the closest surface separation distance. We define x and y as follows

$$x = \frac{h}{2R_1}, \qquad y = \frac{2R_2}{2R_1} = \frac{R_2}{R_1}, \tag{2.3.27}$$

where x is the ratio of the particle distance h and the diameter of the sphere 1 $2R_1$, y is the ratio of the diameter of the two spheres. By introducing Eq.(2.3.26) and Eq.(2.3.27), we can rewrite Eq.(2.3.25), for instance, the first term becomes

$$\begin{aligned}\frac{1}{12}\frac{4R_1R_2}{C^2-(R_1+R_2)^2} &= \frac{1}{12}\frac{4R_1R_2}{(R_1+R_2)^2+2h(R_1+R_2)+h^2-(R_1+R_2)^2} \\ &= \frac{\frac{4R_1R_2}{4R_1^2}}{(\frac{h}{2R_1})^2+\frac{2hR_1}{4R_1^2}+\frac{2hR_2}{4R_1^2}} \\ &= \frac{y}{x^2+xy+x}.\end{aligned}$$

By rewriting other terms, Eq.(2.3.25) can be expressed as

$$V_{vdW}^{S}(h) = -\frac{A_{\mathrm{H}}}{12}\left[\frac{y}{x^2+xy+x}+\frac{y}{x^2+xy+x+}+2\ln\frac{x^2+xy+x}{x^2+xy+x+y}\right], \tag{2.3.28}$$

where $A_{\mathrm{H}} = \lambda N^2\pi^2$ is the Hamaker constant. Hamaker discussed some cases where the newly introduced variables are small and large in his paper[56].

For equal-sized particles $y = 1$. With the particle radius R, we obtain

$$V_{vdW}^{S}(h) = -\frac{A_{\mathrm{H}}}{12}\left[\frac{1}{x^2+2x}+\frac{1}{x^2+2x+1}+2\ln\frac{x^2+2x}{x^2+2x+1}\right]. \tag{2.3.29}$$

By introducing $s = 2 + \frac{h}{R}$ and using the following relations

$$\begin{aligned}\frac{1}{2}\frac{1}{x^2+2x} &= \frac{1}{2}\frac{4}{4\frac{h^2}{4R^2}+4\frac{2h}{2R}} = \frac{2}{\frac{h^2}{R^2}+4\frac{h}{R}} = \frac{2}{\frac{h^2}{R^2}+4\frac{h}{R}+4-4} \\ &= \frac{2}{\left(2+\frac{h}{R}\right)^2-4} = \frac{2}{s^2-4},\end{aligned}$$

$$\frac{1}{2}\frac{1}{x^2+2x+1} = \frac{1}{2}\frac{4}{4\frac{h^2}{4R^2}+4\frac{2h}{2R}+4} = \frac{2}{\frac{h^2}{R^2}+4\frac{h}{R}+4}$$
$$= \frac{2}{\left(2+\frac{h}{R}\right)^2} = \frac{2}{s^2},$$

we can obtain the following equation:

$$V_{vdW}^{S}(h) = -\frac{A_{\mathrm{H}}}{6}\left[\frac{2}{s^2-4}+\frac{2}{s^2}+\ln\frac{s^2-4}{s^2}\right]. \tag{2.3.30}$$

Eq.(2.3.30) is the van der Waals potential for equal-sized particles without retardation effects, which cause the reduction of the van der Waals attraction at longer distances due to the finite propagation speed of the light and electromagnetic field. Some expressions have been derived by the previous works[57, 58, 59]. We use the one in Ref. [57] in the following chapter.

2.4 Electrostatic interaction

When the charged surfaces accompanied with the electrical double layer approach with each other, it results in the overlapped double layers and thus the electrostatic interaction between the surfaces emerges due to the local increase in the sum of osmotic pressure and the Maxwell's stress (tension in one-dimension). Throughout this thesis, we use the Derjaguin approximation to calculate inter-particle electrostatic interactions.

Let us consider a volume element Adx with the cross section A separated by the distances between x and $x+dx$ from a charged surface in an electrolyte solution, and the force balance on the volume element Adx as shown in **Fig. 2.4.1**. In the electrolyte solution, ions are distributed following the Boltzmann distribution. The volume element is in balance by the pressure on the faces at x and $x+dx$, and the electrical force acting on the charges inside the Adx. If we set the pressure as $p(x)$, the charge density as ρ_e, the force balance on the volume element Adx is given by

$$p(x)A - p(x+dx)A - \rho_e A dx\frac{d\psi}{dx} = 0.$$

Here, we define that the force in the positive x-axis direction is positive. The direction of the electrical force depends on the sign of the charges. From the force balance, we

obtain

$$\frac{p(x+dx)-p(x)}{dx}+\rho_e\frac{d\psi}{dx}=0$$
$$\Leftrightarrow \frac{dp}{dx}+\rho_e\frac{d\psi}{dx}=0. \tag{2.4.1}$$

Since the charge distribution follows the Poisson equation, substituting Eq.(2.2.5) into the equation above leads to

$$\frac{dp}{dx}-\epsilon_r\epsilon_0\frac{d^2\psi}{dx^2}\frac{d\psi}{dx}=0$$
$$\Leftrightarrow \frac{dp}{dx}-\epsilon_r\epsilon_0\frac{d}{dx}\left[\frac{1}{2}\left(\frac{d\psi}{dx}\right)^2\right]=0$$
$$\Leftrightarrow \frac{d}{dx}\left[p-\frac{1}{2}\epsilon_r\epsilon_0\left(\frac{d\psi}{dx}\right)^2\right]=0.$$

Thus, we can obtain the following equation

$$p(x)-\frac{1}{2}\epsilon_r\epsilon_0\left(\frac{d\psi}{dx}\right)^2=Const. \tag{2.4.2}$$

The second term on the left hand side means Maxwell's stress term. At equilibrium, Eq.(2.4.2) is independent of the position from the surface. This means that the difference of the pressure and Maxwell's stress near or between the surfaces is constant. The force per unit area has the same dimension of the energy per unit volume. Therefore,

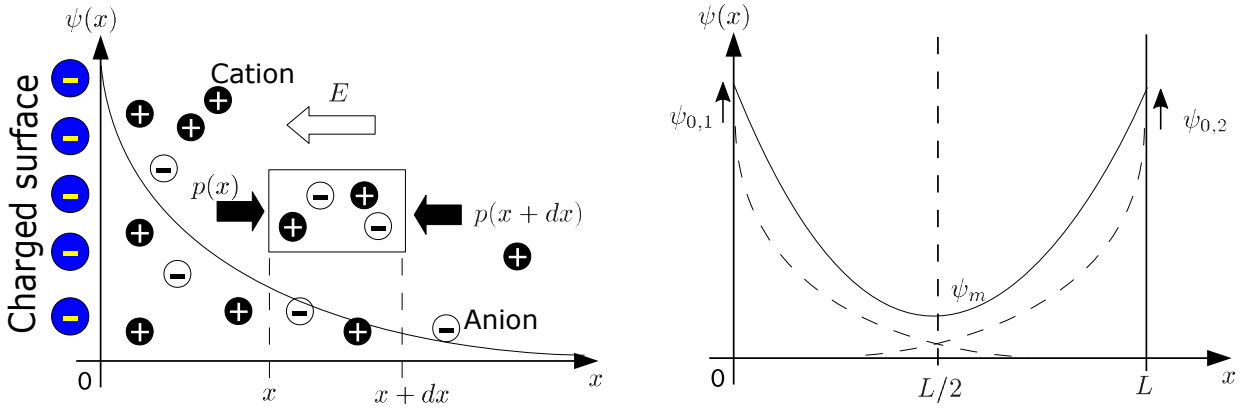

Figure 2.4.1: Schematic representation of an electrical potential distribution in an electrolyte solution adjacent to an isolated plate: a force balance at a control volume and an electrical potential distribution between two paralell plates.

Eq.(2.4.2) can be interpreted that the sum of pressure and electric energy is conserved irrespective of the position at equilibrium.

The electrical potential distribution between two charged surfaces is determined by the interaction between them. To relate the pressure $p(x)$ with the electrical potential $\psi(x)$, we rewrite Eq.(2.4.1) by multiplying dx on the both side as

$$dp = -\rho_e d\psi. \tag{2.4.3}$$

Since the ions follow the Boltzmann distribution, one can substitute Eq.(2.2.1) and Eq.(2.2.6) into Eq.(2.4.3) to obtain the following equation:

$$dp = -\sum_i z_i e n_{i,b} \exp\left(-\frac{z_i e\psi(x)}{k_B T}\right) d\psi. \tag{2.4.4}$$

Using the fact that the electrical potential decays to zero as the distance from the surfaces approaches to infinity, we can simply integrate Eq.(2.4.4) as

$$p(x) - p_b = k_B T \sum_i C_{i,b} \left[\exp\left(-\frac{z_i e\psi(x)}{k_B T}\right) - 1\right], \tag{2.4.5}$$

where p_b is the pressure in the bulk solution. By subtraction of p_b from Eq.(2.4.2), we can define the expression for the disjoining pressure due to the electrical double layer Π_{dl} as

$$\Pi_{dl} = k_B T \sum_i C_{i,b} \left[\exp\left(-\frac{z_i e\psi(x)}{k_B T}\right) - 1\right] - \frac{\epsilon_r \epsilon_0}{2} \left(\frac{d\psi(x)}{dx}\right)^2. \tag{2.4.6}$$

This equation Eq.(2.4.6) can be used to calculate the pressure between the charged surfaces even for asymmetrical surfaces such as oppositely-charged surfaces.

For symmetrically charged surfaces separated by distance L, the gradient of electrical potential between the surfaces at the midpoint $L/2$ becomes zero as described below

$$\frac{d\psi}{dx}\Big|_{x=L/2} = 0.$$

Therefore, at $x = L/2$, from Eq.(2.4.6), the disjoining pressure between the symmetrical surfaces is given by the osmotic pressure at the midpoint $L/2$. That is, in symmetrical

electrolyte solution, Eq.(2.4.6) becomes

$$\Pi_{dl}(L) = 2C_b k_B T \left[\cosh\left(\frac{ze\psi_m(L)}{k_B T}\right) - 1\right], \tag{2.4.7}$$

where $\psi_m(L) = \psi(L/2)$. Note that the pressure $\Pi_{dl}(L)$ and midpoint potential $\psi_m(L) = \psi(L/2)$ depend on the separation distance L. From Eq.(2.4.7) for the symmetrically charged plates with the Derjaguin approximation Eq.(2.3.13), the electrostatic repulsion between two spheres $F^S_{edl}(y)$ can be calculated by

$$\begin{aligned} F^S_{edl}(y) &= \frac{2\pi R_1 R_2}{R_1 + R_2} \int_y^\infty \Pi_{dl}(L) dL \\ &= \frac{2\pi R_1 R_2}{R_1 + R_2} V^P_{edl}(y) \\ &= 4\pi n_b k_B T \frac{R_1 R_2}{R_1 + R_2} \int_y^\infty \left[\cosh\left(\frac{ze\psi_m(L)}{k_B T}\right) - 1\right] dL, \end{aligned} \tag{2.4.8}$$

where y is the particle separation distance, as an integration variable, and $V^P_{edl}(y)$ is the electrostatic repulsive energy per unit area between the charged surfaces. From the relationship between conservative force and potential Eq.(2.3.15), the inter-particle electrostatic potential energy $V^S_{edl}(h)$ is given as follows

$$\begin{aligned} V^S_{edl}(h) &= \int_h^\infty F^S_{edl}(y) dy \\ &= 4\pi C_b k_B T \frac{R_1 R_2}{R_1 + R_2} \int_h^\infty \int_y^\infty \left[\cosh\left(\frac{ze\psi_m(L)}{k_B T}\right) - 1\right] dL dy, \end{aligned} \tag{2.4.9}$$

where h is the inter-particle distance. For equal-sized particles, Eq.(2.4.9) becomes

$$V^S_{edl}(h) = 2\pi C_b R k_B T \int_h^\infty \int_y^\infty \left[\cosh\left(\frac{ze\psi_m(L)}{k_B T}\right) - 1\right] dL dy. \tag{2.4.10}$$

These expressions of Eq.(2.4.8) and Eq.(2.4.10) can be applied for symmetrical electrolyte solution and charged surfaces with arbitrary electrical potential. These equations need numerical integrations.

For low potential case, $\frac{ze\psi_m(L)}{k_B T} < 1$, Eq.(2.4.7) can be expanded with Taylor's series taking until its second-order since $x < 1 \;\Rightarrow\; \exp x = 1 + x + \frac{x^2}{2!} + \cdots$ and the first term

is canceled with the expansion of $\exp(-x)$,

$$\begin{aligned} F_{edl}^{P} &\approx 2C_b k_B T \left[1 + \frac{1}{2}\left(\frac{ze\psi_m(L)}{k_B T}\right)^2\right] - 1 \\ &= C_b k_B T \left(\frac{ze\psi_m(L)}{k_B T}\right)^2 \\ &= \frac{1}{2}\epsilon_r \epsilon_0 \kappa^2 \psi_m(L)^2. \end{aligned} \tag{2.4.11}$$

Note that we use the definitions of cosh and the Debye screening parameter Eq.(2.2.9).

In **Fig. 2.4.1**, where the surface potentials are different $\psi_{0,1} \neq \psi_{0,2}$, the potential gradient at the midpoint does not become zero. Since Eq.(2.4.6) is satisfied, the disjoining pressure for low potential case can be expressed as

$$F_{edl}^{P}(L) = \frac{1}{2}\epsilon_r \epsilon_0 \left[\kappa^2 \psi_m(L)^2 - \left(\frac{d\psi}{dx}\right)^2_{x=L/2}\right]. \tag{2.4.12}$$

Putting the Debye parameter for general electrolyte Eq.(2.2.9), Eq.(2.4.12) can be used for general electrolyte solution case with low potential. For arbitrary potential case, Eq.(2.4.7), if the charged surfaces have the same sign of charges but not symmetrical, Behrens *et al.* have used an analytical solution for non-linear PB equation[60].

2.4.1 Linear superposition approximation

From Eq.(2.2.12), we have

$$\tanh\left(\frac{ze\psi(x)}{4k_B T}\right) = \tanh\left(\frac{ze\psi_0}{4k_B T}\right)\exp(-\kappa x).$$

If the position x is far from the surface so that $\frac{ze\psi(x)}{k_B T} \ll 1$, we can apply the linear approximation to above equation

$$\psi(x) = \frac{4k_B T}{ze}\tanh\left(\frac{ze\psi_0}{4k_B T}\right)\exp(-\kappa x) = \psi_{eff}\exp(-\kappa x), \tag{2.4.13}$$

with

$$\psi_{eff} = \frac{4k_B T}{ze}\tanh\left(\frac{ze\psi_0}{4k_B T}\right), \tag{2.4.14}$$

where ψ_{eff} is the effective potential defined by the analogy of the Debye-Hückel approximation Eq.(2.2.11). If the surfaces are separated by large distances so that Eq.(2.4.13) is valid, the midpoint potential $\psi_m(L)$ between the symmetrical surfaces separated by the distance L can be expressed by the linear superposition of the potentials from the each surfaces, so-called linear superposition approximation (LSA),

$$\psi_m(L) \approx 2 \times \frac{4k_BT}{ze} \tanh\left(\frac{ze\psi_0}{4k_BT}\right) \exp\left(-\frac{\kappa L}{2}\right). \tag{2.4.15}$$

From Eq.(2.4.11), we can calculate the electrostatic repulsive force per unit area between the same surfaces via the linear superposition approximation as

$$\begin{aligned} F_{edl}^P &= C_b k_B T \frac{z^2e^2}{k_B^2T^2} \frac{8^2k_B^2T^2}{z^2e^2} \tanh^2\left(\frac{ze\psi_0}{4k_BT}\right) \exp\left(-\kappa L\right) \\ &= 64 n_b k_B T \gamma_0^2 \exp\left(-\kappa L\right), \end{aligned} \tag{2.4.16}$$

where $\gamma_0 = \tanh\left(\frac{ze\psi_0}{4k_BT}\right)$. With Eq.(2.3.15), the electrostatic potential energy per unit area is given by

$$\begin{aligned} V_{edl}^P(L) &= \int_L^\infty F_{edl}^P dL \\ &= \frac{64 C_b k_B T}{\kappa} \gamma_0^2 \exp\left(-\kappa L\right). \end{aligned} \tag{2.4.17}$$

Using the Derjaguin approximation, for the same and equal-sized particles, the inter-particle electrostatic potential $V_{edl}^S(h)$ is described by

$$\begin{aligned} V_{edl}^S(h) &= \pi R \int_h^\infty V_{edl}^P(L) dL \\ &= \frac{64\pi R C_b k_B T}{\kappa^2} \gamma_0^2 \exp\left(-\kappa h\right). \end{aligned} \tag{2.4.18}$$

2.4.2 Charge regulation model

When the interacting charged surfaces approach with each other, they regulates their surface charges to maintain the chemical equilibrium on their ionic groups. This is called charge regulation. For negatively-charged surfaces, since their surface potentials

increase in magnitude attracting more protons when approaching as shown in **Fig. 2.4.1**. However, they have to reduce their surface charges to keep the free energy in the system constant by protonation.

Let us consider the surface with carboxylic surface groups. The ionization of this surface is described by the following dissociation reaction

$$-\mathrm{COOH} \rightleftharpoons -\mathrm{COO}^- + \mathrm{H}^+ \quad (K_\mathrm{H}), \tag{2.4.19}$$

where K_H is the dissociation constant for deprotonation given by

$$\frac{\Gamma_{-\mathrm{COO}^-}\ a^s_{\mathrm{H}^+}}{\Gamma_{-\mathrm{COOH}}} = K_\mathrm{H}, \tag{2.4.20}$$

where $a^S_{\mathrm{H}^+}$ is the surface activity of protons following the Boltzmann distribution as $a^S_{\mathrm{H}^+} = a_{\mathrm{H}^+,b} \exp\left(-\frac{e\psi_0}{k_B T}\right)$. Setting the total site density of the surface groups $\Gamma_{tot} = \Gamma_{-\mathrm{COOH}} + \Gamma_{-\mathrm{COO}^-}$, we obtain the surface charge density as follows

$$\sigma^I(\psi_0) = -e\Gamma_{-\mathrm{COO}^-} = -\frac{e\Gamma_{tot}}{1 + \left(a_{\mathrm{H}^+,b}/K_\mathrm{H}\right) \exp\left(-\frac{e\psi_0}{k_B T}\right)}, \tag{2.4.21}$$

where the super-script I means the value in the inner layer where the dissociation reaction happens. With the analogy of Eq.(2.2.16) to the surfaces, one obtains the relationship on the both surfaces at $x = \pm L/2$

$$\begin{aligned}
\int_S \boldsymbol{E} \cdot \boldsymbol{n} dS &= \frac{1}{\epsilon_r \epsilon_0} \int_V \rho_e dV \\
&\Leftrightarrow -\int_S \nabla\psi \cdot \boldsymbol{n} dS = \frac{1}{\epsilon_r \epsilon_0} Q \\
&\Leftrightarrow -\frac{d\psi}{dn}\Big|_{x=\pm L/2} S = \frac{1}{\epsilon_r \epsilon_0} Q \\
&\Leftrightarrow \frac{d\psi}{dn}\Big|_{x=\pm L/2} = -\frac{\sigma^I(\psi_0)}{\epsilon_r \epsilon_0} \qquad (2.4.22) \\
&\Leftrightarrow \pm\frac{d\psi}{dx}\Big|_{x=\pm L/2} = \frac{\sigma^I(\psi_0)}{\epsilon_r \epsilon_0}, \qquad (2.4.23)
\end{aligned}$$

where we redefined the range of positions as $x = \pm L/2$ and used normal derivative $\frac{d\psi}{dn} = \nabla\psi \cdot \boldsymbol{n}$ obtained from the chain rule of composite function, and $\boldsymbol{n}$ is the unit normal vector to the surfaces meaning that $\nabla\psi \cdot \boldsymbol{n}|_{x=-L/2} = \frac{d\psi}{dx}\big|_{x=-L/2}$ and $\nabla\psi \cdot \boldsymbol{n}|_{x=L/2} =$

$-\frac{d\psi}{dx}\big|_{x=L/2}$. Eq.(2.4.23) indicates that the electrical boundary condition depends on the surface potentials determined with the interaction between the charged surfaces, changing with the surface separation distance.

For simplicity, let us see the case in symmetrical electrolyte solution. In this case, Eq.(2.2.7) can be expressed as Gouy-Chapman theory as

$$\frac{d^2\psi(x)}{dx^2} = \frac{k_B T}{ze}\kappa^2 \sinh\left(\frac{ze\psi(x)}{k_B T}\right), \tag{2.4.24}$$

where we used the definition of $\sinh(x) = (\exp(x) - \exp(-x))/2$ and the Debye parameter. By introducing non-dimensional electrical potential $\Psi(x) = ze\psi(x)/(k_B T)$, we obtain

$$\frac{d^2\Psi(x)}{dx^2} = \kappa^2 \sinh\Psi(x), \tag{2.4.25}$$

This equation can be easily integrated once by multiplying $d\Psi(x)/dx$ on the both sides as

$$\begin{aligned} &\frac{d\Psi(x)}{dx}\frac{d^2\Psi(x)}{dx^2} = \kappa^2 \sinh\Psi(x)\frac{d\Psi(x)}{dx} \\ \Leftrightarrow\ &\frac{1}{2}\frac{d}{dx}\left(\frac{d\Psi(x)}{dx}\right)^2 = \kappa^2\frac{d}{dx}\{\cosh\Psi(x)\}. \end{aligned}$$

Then, we have

$$\left(\frac{d\Psi(x)}{dx}\right)^2 = 2\kappa^2 \cosh\Psi(x) + C_1, \tag{2.4.26}$$

where C_1 is the integration constant. Set the midpoint between the surfaces separated by the distance L to the origin $x = 0$, the potential gradient at $x = 0$ becomes zero, in other words, the boundary conditions are given by

$$\frac{d\Psi(x)}{dx}\Big|_{x=0} = 0, \tag{2.4.27}$$

$$\Psi(x=0) = \Psi_m = \cosh^{-1}(1 + P/2), \tag{2.4.28}$$

with[61]

$$P = \frac{\Pi_{dl}}{C_b k_B T} = 2(\cosh\Psi - 1).$$

From Eq.(2.4.27) and Eq.(2.4.28), we can express the integration constant to be $C_1 = -2\kappa^2 \cosh \Psi_m$, and Eq.(2.4.26) can be rewritten as

$$\left(\frac{d\Psi(x)}{dx}\right)^2 = 2\kappa^2\{\cosh \Psi(x) - \cosh \Psi_m\}. \tag{2.4.29}$$

Let us introduce the expressions $\Omega(x) = \exp[\Psi(x) - \Psi_m]$ and $\xi = \exp(\Psi_m)$,

$$\left(\frac{d}{dx}\{\Psi_m + \ln \Omega(x)\}\right)^2 = \kappa^2\{e^{\Psi_m + \ln \Omega(x)} + e^{-\{\Psi_m + \ln \Omega(x)\}} - e^{\ln \xi} - e^{-\ln \xi}\}$$
$$\Leftrightarrow \left(\frac{1}{\Omega(x)}\frac{d\Omega(x)}{dx}\right)^2 = \kappa^2[\xi\Omega(x) + \{\xi\Omega(x)\}^{-1} - \xi - \xi^{-1}].$$

By multiplying the both side of above equation by $\Omega(x)^2$ and factorizing it, one obtains

$$\begin{aligned}\left(\frac{d\Omega(x)}{dx}\right)^2 &= \kappa^2[\xi\Omega(x)^3 + \xi^{-1}\Omega(x) - \xi\Omega(x)^2 - \xi^{-1}\Omega(x)^2] \\ &= \kappa^2\xi^{-1}\Omega(x)\{1 - \Omega(x)\}\{1 - \xi^2\Omega(x)\}.\end{aligned}$$

Taking the square root of this equation, we have

$$\frac{d\Omega(x)}{dx} = \pm\kappa\xi^{-\frac{1}{2}}\sqrt{\Omega(x)\{1 - \Omega(x)\}\{1 - \xi^2\Omega(x)\}}. \tag{2.4.30}$$

Here, we consider negatively-charged surfaces. That is, $\Psi(x = \pm L/2) \leq 0$, $d\Psi/dx \leq 0$ for $x \geq 0$. With the symmetry of the system, it allows us that solving the half region divided by the midpoint is equal to solving the whole region. The second condition $d\Psi/dx \leq 0$ for $x \geq 0$ can be known from the fact that the midpoint potential can not be lower than the surface potential if the surfaces are negatively-charged. This second condition and the definition of $\Omega(x)$ indicate that always $\Omega(x) \geq 0$, and $d\Omega/dx = \Omega d\Psi/dx \leq 0$. Therefore, in this case, Eq.(2.4.30) can only be negative as

$$\frac{d\Omega(x)}{dx} = -\kappa\xi^{-\frac{1}{2}}\sqrt{\Omega(x)\{1 - \Omega(x)\}\{1 - \xi^2\Omega(x)\}}. \tag{2.4.31}$$

With the variable separation of Eq.(2.4.31), we can obtain

$$\frac{d\Omega}{\sqrt{\Omega(1 - \Omega)(1 - \xi^2\Omega)}} = -\frac{\kappa}{\sqrt{\xi}}dx. \tag{2.4.32}$$

By integrating Eq.(2.4.32) in the ranges $0 \to x$ for the left-hand side, and $\Omega(0) = 1 \to \Omega(x)$ for the right-hand side, we have

$$-\frac{\kappa x}{\sqrt{\xi}} = \int_1^{\Omega} \frac{d\Omega'}{\sqrt{\Omega'(1-\Omega')(1-\xi^2\Omega')}}. \tag{2.4.33}$$

With the change of variables as $\Omega = \sin^2\theta$ and $d\Omega = 2\sin\theta\cos\theta d\theta$, the integral interval becomes $\theta : \pi/2 \to \sin^{-1}\sqrt{\Omega}$, and we obtain with splitting the interval of integral as

$$\begin{aligned} -\frac{\kappa x}{2\sqrt{\xi}} &= \int_{\pi/2}^{\sin^{-1}\sqrt{\Omega}} \frac{d\theta}{\sqrt{1-\xi^2\sin^2\theta}} \\ &= \int_0^{\sin^{-1}\sqrt{\Omega}} \frac{d\theta}{\sqrt{1-\xi^2\sin^2\theta}} - \int_0^{\pi/2} \frac{d\theta}{\sqrt{1-\xi^2\sin^2\theta}}. \end{aligned} \tag{2.4.34}$$

In Eq.(2.4.34), we define the elliptic integral of the first kind as follows

$$u = \int_0^{\phi} \frac{d\theta}{\sqrt{1-m^2\sin^2\theta}} = F(\phi, m). \tag{2.4.35}$$

The integral of Eq.(2.4.35) with $\phi = \pi/2$, $K(m)$, is specially called the complete elliptic integral of the first kind. The Jacobian elliptic function is defined as an inverse function of the integral Eq.(2.4.35) with

$$\mathrm{sn}(u, m) = \sin\phi, \tag{2.4.36}$$

$$\mathrm{cn}(u, m) = \cos\phi = \sqrt{1-\mathrm{sn}^2(u, m)}, \tag{2.4.37}$$

$$\mathrm{dn}(u, m) = \frac{d\phi}{du} = \frac{1}{du/d\phi} = \sqrt{1-m^2\mathrm{sn}^2(u, m)}, \tag{2.4.38}$$

$$\mathrm{cd}(u, m) = \frac{\mathrm{cn}(u, m)}{\mathrm{dn}(u, m)} = \mathrm{sn}(K(m) - u, m), \tag{2.4.39}$$

where the equation for $\mathrm{cd}(u, m)$ means the periodicity of the elliptic function. From above equations, Eq.(2.4.34) can be expressed as

$$-\frac{\kappa x}{2\sqrt{\xi}} = -u = \mathrm{sn}^{-1}\sqrt{\Omega(x)} - K(\xi), \tag{2.4.40}$$

where sn^{-1} is the inverse function of $\mathrm{sn}(u, m)$. By transferring the second term of the right-hand side to the center and using the definition of the inverse function with the

square root, we can obtain the following equation with Eq.(2.4.39) as

$$\Omega(x) = \mathrm{sn}^2(K(\xi) - u, \xi) = \mathrm{cd}^2(u, \xi), \tag{2.4.41}$$

where $u = \kappa x/(2\sqrt{\xi})$. Recalling the definition of $\Omega(x)$ and $\Psi(x)$, the exact solution of the potential between parallel plates for similarly-charged surfaces can be given by

$$\psi(x) = \psi_m + \frac{2k_BT}{ze} \ln \mathrm{cd}(u, \xi). \tag{2.4.42}$$

Even though we need to calculate the elliptic function numerically, we can determine the electrical potential between charged plates.

The charge density of the interacting parallel plates can be derived from Eq.(2.4.42) and Gauss's law Eq.(2.4.23). From the symmetry of the electrical potential described by Eq.(2.4.42), the charge densities on each plate are identical. Therefore, we just require to calculate the charge density on the one plate located at $x = L/2$ as:

$$\begin{aligned}
\sigma &= -\epsilon_r\epsilon_0 \frac{d\psi(x)}{dn}\Big|_{x=L/2} = \frac{\epsilon_r\epsilon_0 k_BT}{ze}\frac{d\Psi(x)}{dx}\Big|_{x=L/2} \\
&= \frac{\epsilon_r\epsilon_0 k_BT}{ze}\frac{d\Psi(x)}{dx}\Big|_{x=L/2} = \frac{\epsilon_r\epsilon_0 k_BT}{ze}\Omega^{-1}\frac{d\Omega(x)}{du}\frac{du}{dx}\Big|_{x=L/2} \\
&= \frac{\epsilon_r\epsilon_0 k_BT}{ze}\mathrm{cd}^{-2}(u,\xi)\frac{d}{du}\{\mathrm{cd}^2(u,\xi)\}\frac{d}{dx}\left(\frac{\kappa x}{2\sqrt{\xi}}\right)\Big|_{x=L/2} \\
&= \frac{\epsilon_r\epsilon_0 k_BT}{ze}\mathrm{cd}^{-1}(u,\xi)\frac{d}{du}\{\mathrm{cd}(u,\xi)\}\frac{\kappa}{\sqrt{\xi}}\Big|_{x=L/2}.
\end{aligned}$$

Using the following equation

$$\begin{aligned}
\frac{d}{du}\{\mathrm{cd}(u,\xi)\} &= \frac{d}{du}\left(\frac{\mathrm{cn}(u,\xi)}{\mathrm{dn}(u,\xi)}\right) \\
&= \frac{\frac{d}{du}\{\mathrm{cn}(u,\xi)\}\mathrm{dn}(u,\xi) + \mathrm{cn}(u,\xi)\frac{d}{du}\{\mathrm{dn}(u,\xi)\}}{\mathrm{dn}^2(u,\xi)} \\
&= \frac{-\mathrm{cn}(u,\xi)\mathrm{dn}^2(u,\xi) + \xi^2\mathrm{cn}^2(u,\xi)\mathrm{sn}(u,\xi)}{\mathrm{dn}^2(u,\xi)} \\
&= \frac{(\xi^2-1)\mathrm{sn}(u,\xi)}{\mathrm{dn}^2(u,\xi)},
\end{aligned}$$

we can finally obtain the surface charge density as follows

$$\begin{aligned}\sigma &= \frac{\epsilon_r\epsilon_0 k_B T}{ze}\mathrm{cd}^{-1}(u,\xi)\frac{(\xi^2-1)\mathrm{sn}(u,\xi)}{\mathrm{dn}^2(u,\xi)}\frac{\kappa}{\sqrt{\xi}}\Big|_{x=L/2} \\ &= \frac{\epsilon_r\epsilon_0 k_B T}{ze}\frac{\kappa(\xi^2-1)}{\sqrt{\xi}}\frac{\mathrm{sn}(u,\xi)}{\mathrm{cn}(u,\xi)\mathrm{dn}(u,\xi)}\Big|_{x=L/2}. \end{aligned} \tag{2.4.43}$$

Eq.(2.4.43) denotes that the charge density is determined by the midpoint potential or the osmotic pressure with Eq.(2.4.28) at $x = L/2$ since $u = \kappa x/(2\sqrt{\xi})$.

2.4.3 Constant (linearized) charge regulation

In the case of the charge regulating surfaces, we have to consider the relationship between surface charge density $\sigma(\psi_0)$ and electrical potential ψ_0 as depicted in **Fig. 2.4.2**. The curve is given by ionization charge models such as Eq.(2.4.21). The solid lines for infinite and finite separation are given by Eq.(2.2.17) for the isolated surface charge density and Eq.(2.4.43) for the interacting one, respectively. If we define the surface potential for an isolated plate as ψ_0^{iso}, the intersection point of the line by Eq.(2.4.21) with the one by Eq.(2.2.17) gives the solution of the two equations Eqs.(2.4.21) and (2.2.17).

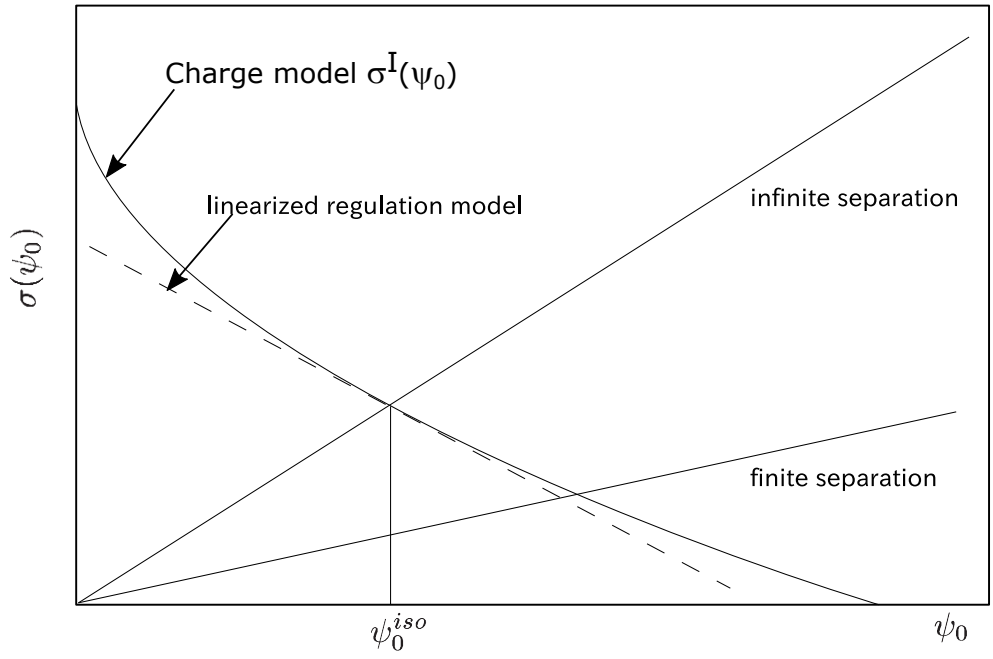

Figure 2.4.2: Charge-potential relationship with a charge regulation model.

It is sometimes difficult to exactly know the ionization isotherm for the surfaces such as Eq.(2.4.21) to be incorporated in the boundary condition for calculating the electrostatic interaction. Such boundary conditions can make the boundary value problems complicated because of its nonlinearity. To mitigate this difficulty, the linearization to the boundary condition has been proposed to solve the linearized problem, Eq.(2.2.8), by the previous researcher[62]. It has been used to solve the nonlinear Poisson-Boltzmann equation Eq.(2.2.7)[63, 64]. Within this concept, the relationship between $\sigma(\psi_0)$ and ψ_0 is approximated with the tangential line at $\psi_0 = \psi_0^{iso}$. This can be interpreted as a linear approximation of $\sigma^I(\psi_0)$ around $\psi_0 = \psi_0^{iso}$. Thus, it is called the linearized regulation model or constant charge regulation model. The tangential line is given by the following equation

$$\sigma^I(\psi_0) \approx \sigma_{tan}(\psi_0) = \sigma(\psi_0^{iso}) - C^I(\psi_0 - \psi_0^{iso}), \tag{2.4.44}$$

with

$$C^I = -\left[\frac{d\sigma^I}{d\psi_0}\right]_{\psi_0=\psi_0^{iso}}, \tag{2.4.45}$$

where C^I (≥ 0) is the inner layer capacitance which has the unit of electrostatic capacitance per unit area. Eq.(2.4.44) gives the linearized boundary condition on the surfaces. For further use, this can be rewritten for the charged surfaces located at $x = \pm L/2$ as

$$\pm\epsilon_r\epsilon_0 \frac{d\psi}{dx}\Big|_{x=\pm L/2} = \sigma\left(\psi_\pm^{iso}\right) - C_\pm^I\left[\psi(\pm L/2) - \psi_\pm^{iso}\right], \tag{2.4.46}$$

where $\psi_\pm^{iso}$ is the surface potential, $\sigma\left(\psi_\pm^{iso}\right)$ is the surface charge density, $C_\pm^I$ is the inner layer capacitance of the two isolated surfaces, and $\psi(\pm L/2)$ is the potential at the interacting surfaces. The inner layer capacitance $C_\pm^I$ for each surfaces can be readily treated by introducing the regulation parameter

$$p_\pm = \frac{C_\pm^{dl}}{C_\pm^{dl} + C_\pm^I}, \tag{2.4.47}$$

where $C_{\pm}^{dl} = \frac{d\sigma_{\pm}}{d\psi_{\pm}}$ is the diffuse layer capacitance of the isolated surfaces. When the regulation parameter $p_{\pm}$ is unity, the problem reduces to the constant charge (CC) condition, while $p_{\pm} = 0$, it reduces to the constant potential (CP) condition as classical limiting cases. This constant charge regulation model can be easily used for asymmetrically charged surfaces and also general electrolyte solutions with the appropriate expressions for the diffuse layer charge density as used in the previous researchers[65, 66, 67, 68].

2.5 DLVO theory

Up to the previous section, we have seen the fundamental framework for the van der Waals attraction and electrostatic repulsion between identical particles. Within DLVO theory, the net mutual interaction acting on particles is expressed as the superposition of the van der Waals attraction and the electrostatic repulsion. DLVO theory gives us a perspective to discuss the aggregation-dispersion of colloids by the balance of the attraction and repulsion. The net potential can be described by the superposition of the van der Waals and electrostatic potentials as follows

$$V(h) = V_{vdW}(h) + V_{edl}(h). \tag{2.5.1}$$

We show an example of the calculations of the DLVO potential in **Fig. 2.5.1**. In **Fig. 2.5.1**, we assume the carboxylated polystyrene latex particles with the diameter of $2R = 1.5$ μm, and the site density of $\Gamma_{tot=}1.136$ nm^{-2} in 10 mM KCl solution at pH 3.5. The dotted line is the van der Waals potential, and the broken lines are the electrostatic potential. The solid lines are calculations of the net interaction potential. Depending on the electrostatic boundary conditions, the black, red, and blue lines are calculated with the constant charge (CC), charge regulation (CR), and constant potential (CP) models, respectively. The maximum values in the potential located around the Debye length are called the energy barrier. The first minimum from the origin is called the primary minimum, and the second one is called the secondary minimum. The higher energy barrier obviously means the stronger repulsion impeding the particle aggregation. To form aggregates in the primary minimum by overcoming the energy barrier, the particles require the higher energy than the barrier. The reason why the DLVO theory has

been widely accepted is that it explains the Schulze-Hardy rule known as an empirical rule[69]. This suggests that ions with higher valence enhance aggregation, and the critical coagulation concentration described later is inversely proportional to the 2nd-6th power of the ionic valence.

To show this relation, let us express the net potential for equal-sized particles as the superposition of Eq.(2.3.19) and Eq.(2.4.18), that is,

$$V^S(h) = \frac{64\pi RC_b k_B T}{\kappa^2}\gamma_0^2 \exp(-\kappa h) - \frac{AR}{12h}. \tag{2.5.2}$$

The energy barrier as shown in **Fig.2.5.1** decreases with decreasing electrostatic repulsion by increase of electrolyte concentrations and decrease of surface potentials. The salt concentration, where the energy barrier disappears, is here called the critical coagulation concentration (CCC). Since the energy barrier is the maximum on the potential curve, the potential gradient at the position on the barrier is zero. Hence, the disap-

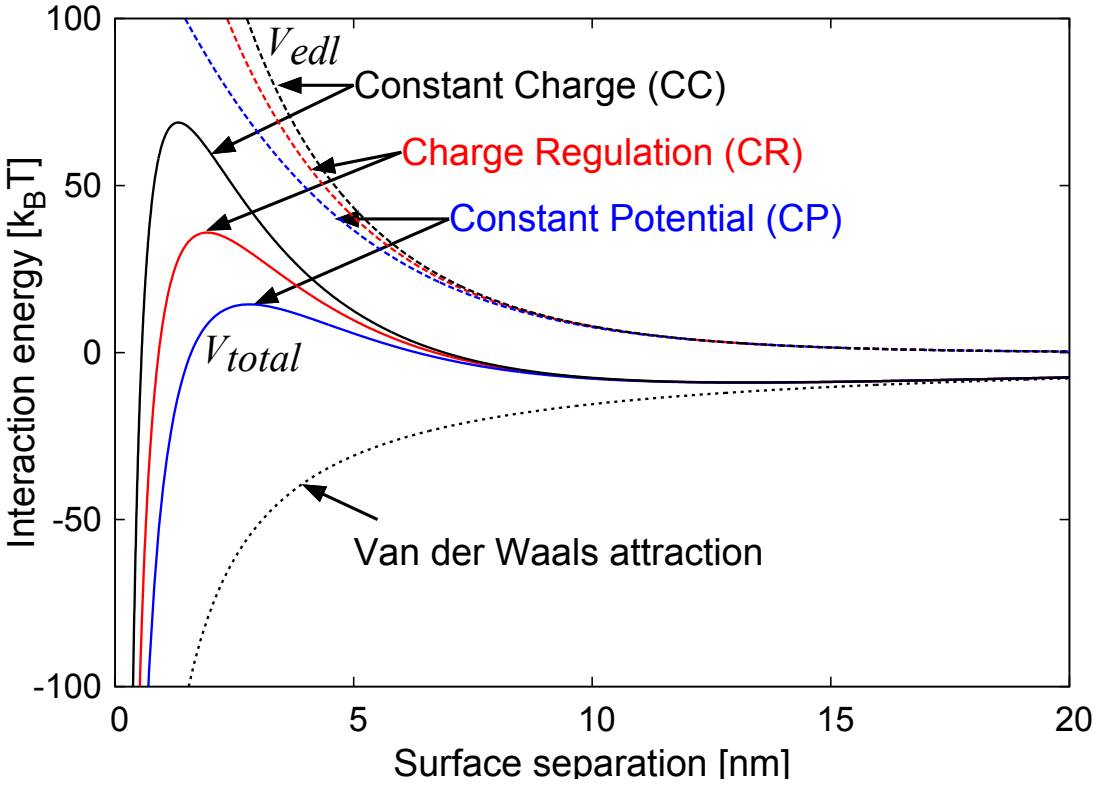

Figure 2.5.1: Relationship between interaction energy and surface separation. A carboxyl latex particle with a diameter of 1.5 μm and a site density of 1.136 nm^{-2} at ionic strength 10 mM and pH 3.5. Dotted line, broken lines, and solid lines are van der Waals attratction, electrostatic repulsion, and total pair interaction energy, respectively.

pearance of the energy barrier means the potential at the barrier becomes zero, that is, $V_{max} = 0$. Therefore, the critical coagulation concentration $C_{b,c}$ satisfies the following equations

$$\frac{dV^S}{dh} = -\frac{64\pi R C_{b,c} k_B T}{\kappa}\gamma_0^2 \exp(-\kappa h) + \frac{AR}{12h^2} = 0, \tag{2.5.3}$$

$$V^S(h) = \frac{64\pi R C_{b,c} k_B T}{\kappa^2}\gamma_0^2 \exp(-\kappa h) - \frac{AR}{12h} = 0. \tag{2.5.4}$$

Dividing Eq.(2.5.3) by $-\kappa$, we have

$$\frac{64\pi R C_{b,c} k_B T}{\kappa^2}\gamma_0^2 \exp(-\kappa h) - \frac{AR}{12\kappa h^2} = 0. \tag{2.5.5}$$

Comparing Eq.(2.5.5) with Eq.(2.5.4), one obviously requires to be $\kappa h = 1$ in order to hold these equations simultaneously. By substituting $\kappa h = 1$, we can obtain

$$\begin{aligned}
&\frac{64\pi R C_{b,c} k_B T}{\kappa^2}\gamma_0^2 \exp(-1) - \frac{AR\kappa}{12} = 0 \\
\Leftrightarrow\ &\frac{64\pi C_{b,c} k_B T}{A}\gamma_0^2 \exp(-1) = \frac{\kappa^3}{12} \\
\Leftrightarrow\ &\frac{64\pi C_{b,c} k_B T}{A}\gamma_0^2 \exp(-1) = \frac{1}{12}\left(\frac{2z^2e^2C_{b,c}}{\epsilon_r\epsilon_0 k_B T}\right)^{\frac{3}{2}} \\
\Leftrightarrow\ &C_{b,c}^{\frac{1}{2}} = \frac{768\pi k_B T}{A}\gamma_0^2 \exp(-1)\left(\frac{\epsilon_r\epsilon_0 k_B T}{2z^2e^2}\right)^{\frac{3}{2}} \\
\Leftrightarrow\ &C_{b,c} = \frac{(768)^2\pi^2(k_B T)^2}{A^2}\gamma_0^4 \exp(-2)\left(\frac{\epsilon_r\epsilon_0 k_B T}{2z^2e^2}\right)^3 \\
\Leftrightarrow\ &C_{b,c} = \frac{(384)^2\pi^2(\epsilon_r\epsilon_0)^3(k_B T)^5}{2A^2e^6\exp(2)}\frac{\gamma_0^4}{z^6}.
\end{aligned} \tag{2.5.6}$$

In the case of high surface potential ψ_0, with the definition of hyperbolic function, we can rewrite as $\gamma_0 = \tanh\left(\frac{ze\psi_0}{4k_BT}\right) \approx \pm 1$. Eq.(2.5.6) gives the relation that $C_{b,c}$ is proportional to the sixth power of the ion valence z as partially mentioned in the Schulze-Hardy rule for high surface potential case. More generally, the Schulze-Hardy rule can written as follows[69]

$$C_{b,c} = \frac{Const.}{z^x} \qquad (2 < x < 6). \tag{2.5.7}$$

In the high surface potential limit, Eq.(2.5.7) reduces to $x \to 6$. This means that the dependence of CCC on ion valence can be weak for low potential case.

In this chapter, we have summarized the DLVO theory with the analytical expressions for the van der Waals attraction and the electrostatic interaction used in this thesis. In next Chapter 3, we give a summary of aggregation kinetics including the DLVO theory. The expressions explained in next chapter are used to analyze the experimental aggregation rates in the following chapters.

Chapter 3

Electrophoresis and aggregation kinetics

3.1 Introduction

We have seen that colloidal particles interact with each other through the electrostatic interaction in the previous section. The electrostatic interaction is affected by the charging state of colloidal particles. Quantifying the charge amount is crucial when quantifying aggregation rates. Therefore, investigating the charging behavior of colloidal particles is still a big issue in colloid science. In this chapter, we briefly explain the basic theory on the electrophoretic mobility as a way to estimate the surface charges of colloidal particles used in this thesis. The aggregation rate coefficients including the physico-chemical interactions such as the DLVO force are explained. First, we shortly mention the basic concepts about electrophoresis. Then, we outline the fundamentals on aggregation kinetics to describe the coagulation process.

3.2 Electrophoresis

There are a lot of ways to estimate the charging behavior of colloidal particles such as electrophoresis, streaming potential, adsorption experiment, potentionmetric titration, and electro-acoustic methods and so on[70]. In this study, we have employed the electrophoretic method to evaluate the charging behavior of colloids. The electrophoresis

is widely used for particulate materials. When applying an electric field to particle suspensions, the particles suspended in the solution move along with the direction of the applied electric field. This is called the electrophoresis as depicted in **Fig. 3.2.1**. In the electrophoretic method, by measuring the velocity of particles in the applied electrical field, we can estimate the charge amounts on the particles. The electrophoretic velocity divided by the magnitude of the applied field is called the electrophoretic mobility (EPM). The analysis on experimental values of electrophoretic mobility allows us to confirm the validity of charging models and to obtain the amount of charges on colloidal particles. With the estimates of charge, we can discuss the relationship between their charging and aggregation behavior. Here, we see a basic equation to analyze the electrophoretic mobilities.

3.2.1 Theoretical expression for electrophoretic mobility

When the Debye length κ^{-1}, which is the measure of the thickness of electrical double layer, is thin compared to the particle radius R, that is, $\kappa R \gg 1$, the electric field and the flow field near the particle can be regarded as parallel to the particle surface. In such a case, the electrophoretic mobility μ_m in an electrolyte solution can be expressed by the following Smoluchowski equation:

$$\mu_m = \frac{U}{E} = \frac{\epsilon_r \epsilon_0}{\eta} \zeta, \tag{3.2.1}$$

where η is the viscosity of the medium, U is the particle migration velocity, and E is the magnitude of the applied electric field. ζ is the zeta potential which is defined as the electric potential at the position of slipping plane from the surface. The position of slipping plane is the distance from the surface to the outer boundary of the fluid layer around the particle moving together with the particle. Eq.(3.2.1) indicates the linear relationship between ζ and μ_m, making it convenient to be widely used to convert the experimental electrophoretic mobility to the corresponding zeta potential. In a theoretical manner, for example, the zeta potential ζ can be calculated by introducing the distance of slipping plane x_s to the Gouy-Chapman equation Eq.(2.2.12) as $\zeta = \psi(x = x_s)$[23]. However, the linear relationship in Eq.(3.2.1) does not hold in

higher zeta potential case. With high ζ, the ion distribution around the particle in the presence of the applied electric field differs from the spherically symmetric equilibrium distribution in the absence of the applied field. The electrical double layer deforms as depicted in **Fig. 3.2.1**. This reduces the electrophoretic velocity through the additional electrical force due to polarization, and the viscous drag force from the ions moving to the opposite direction of the particle motion. Such effects are called the relaxation effect in electrophoresis. With considerable relaxation effects, the relationship between the electrophoretic mobility and the zeta potential has been shown to be non-linear by numerical calculation combining the hydrodynamic equation with the ionic transport in the electric field[71]. They showed that the electrophoretic mobility can have its maximum when plotted against ζ, indicating its double-valuedness. Such relaxation effects have been validated in previous experiments[23, 72, 73, 74].

Ohshima has derived approximated analytical expressions with relaxation effects by solving the Stokes equation for creeping flow including ionic transport and electrostatics[75, 76, 77]. Ohshima's approximated analytical equation[75] is in good agreement with the numerical results by O'Brien-White[71] when $\kappa R > 10$, showing that the analytical equation captures the relaxation effects well. Therefore, in this thesis, we have employed the Ohshima equation[75] for symmetrical monovalent electrolyte cases to calculate theoretical electrophoretic mobilities as described later. However, for more general cases such as asymmetrical electrolyte solution, we have used the numerical program by O'Brien-White[71] or the CellMobility program provided by

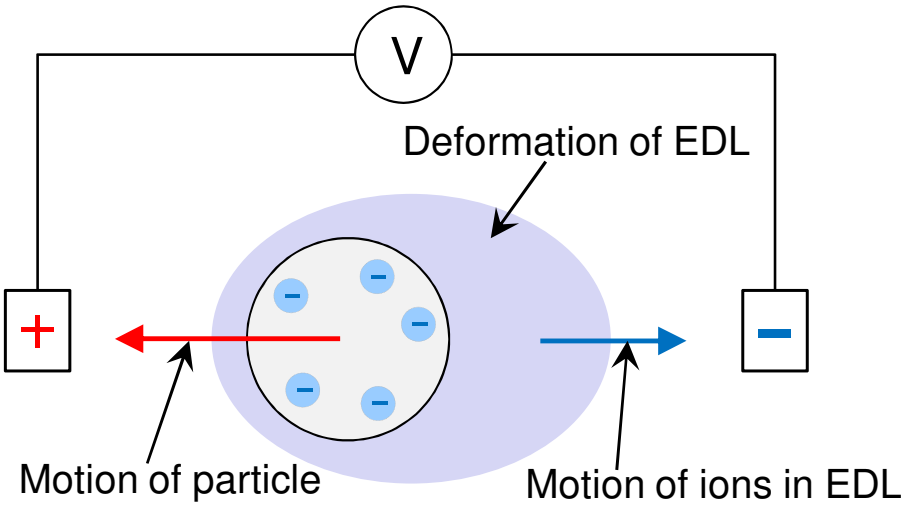

Figure 3.2.1: The schematic view of the electrophoresis with relaxation effect.

the authors of Refs. [78, 79, 80].

3.3 Aggregation kinetics

The aggregation kinetics describes the growth process of aggregates with time by the analogy of reaction kinetics. The parameter representing the growth rate of the aggregates corresponding to the reaction rate constant is called the aggregation rate coefficients formulated by Smoluchowski[12]. In this section, we outline expressions of the aggregation rate coefficients for interacting colloidal particles depending on collision modes between particles. These expressions are used in the following sections for a theoretical analysis.

3.3.1 Population balance equation

The smallest unit of colloidal particles considered in the system is called the primary particle or singlet. An aggregate composed of z primary particles is called zth floc. The relative motion of particles with Brownian motion, shearing flow, and differential sedimentation induces aggregation. As a consequence, the number concentration of zth floc N_z varies with time. In the Smoluchowski treatment, one assumes the following conditions: (i) the aggregation is irreversible and breaking up does not occur after contact, (ii) no multi-body collision occur more than three body collisions, meaning that only two body collisions happen, (iii) the primary particles are spherical and mono-dispersed. With these above assumptions, the temporal change of N_z, dN_z/dt, can be described by the following equation

$$\frac{dN_z}{dt} = \frac{1}{2}\sum_{i+j=z} k_{ij}N_iN_j - N_z\sum_{i=1}^{\infty} k_{iz}N_i, \tag{3.3.1}$$

where k_{ij} is the aggregation rate coefficients between ith flocs and jth flocs. Eq.(3.3.1) is called the population balance equation. The first term on the right-hand side in Eq.(3.3.1) describes the process to form the $z(= i + j)$th flocs due to the collision of ith flocs and jth flocs. The second term expresses the loss of zth flocs by aggregation of zth flocs with other arbitrary flocs.

Here, we focus on aggregation process at early stage where only aggregation between

the primary particles happens to form the secondary particles composed of two primary particles. In this case, Eq.(3.3.1) can be rewritten with respect to the temporal change of the number concentration for the primary and secondary particles

$$\frac{dN_1}{dt} = -k_{11}N_1(0)^2, \quad \frac{dN_2}{dt} = \frac{1}{2}k_{11}N_1(0)^2, \tag{3.3.2}$$

where k_{11} is the aggregation rate coefficients between two primary particles, $N_1(0)$ is the initial number concentration of the primary particles at time $t = 0$.

3.3.2 Brownian aggregation rate coefficients

Brownian aggregation is caused by the collision due to Brownian motion. The Brownian aggregation rate coefficients can be derived by considering the relative diffusion process between interacting colloidal particles[12, 16, 17, 18]. Taking the center of jth flocs as the origin, and taking the r axis outward, we consider the flux by diffusion and conservative forces. First, the relative velocity of ith flocs colliding to jth flocs at the origin v can be calculated by the balance between the conservative force acting on the particles and the hydrodynamic resistance. From **Fig. 3.3.1**, taking the positive direction of force in the direction of r, the relative velocity v can be expressed by

$$\xi v = -\frac{dV^S}{dr}, \tag{3.3.3}$$

where ξ is the hydrodynamic resistance factor. V^S is the physico-chemical interaction potential between ith and jth flocs. The Stokes-Einstein relation is given by

$$D_{ij} = \frac{k_B T}{\xi}, \tag{3.3.4}$$

where D_{ij} is the relative diffusion coefficients of ith and jth flocs. With Eq.(3.3.4), the relative velocity v can be described by

$$v = -\frac{D_{ij}}{k_B T}\frac{dV^S}{dr}. \tag{3.3.5}$$

Note that we take the coordinate outward, and define the outward flux in r to be positive. Thus, one calculate the total flux as the summation of the diffusion flux given by Fick's law J_{B} and the one induced by the conservative force J_{V} described as the product of the number concentration of ith flocs n_{i} and the relative velocity v as follows

$$\begin{aligned} J(r) &= J_{B} + J_{V} \\ &= D_{ij}\left(\frac{dn_{i}}{dr} + \frac{1}{k_{B}T}\frac{dV^{S}}{dr}n_{i}\right). \end{aligned} \tag{3.3.6}$$

At equilibrium, the number of ith flocs colliding to the spherical surface with the radius r per unit time, that is, collision frequency Z [s^{-1}] is given by the following equation[81].

$$\begin{aligned} Z &= 4\pi r^{2} J(r) \\ &= 4\pi r^{2} D_{ij}\left(\frac{dn_{i}}{dr} + \frac{1}{k_{B}T}\frac{dV^{S}}{dr}n_{i}\right) = Const. \end{aligned} \tag{3.3.7}$$

The distribution $y(r)$ can be expressed by

$$y(r) = n_{i}\exp\left(\frac{V^{S}}{k_{B}T}\right). \tag{3.3.8}$$

$$\frac{dy}{dr} = \left(\frac{dn_{i}}{dr} + \frac{1}{k_{B}T}\frac{dV^{S}}{dr}n_{i}\right)\exp\left(\frac{V^{S}}{k_{B}T}\right). \tag{3.3.9}$$

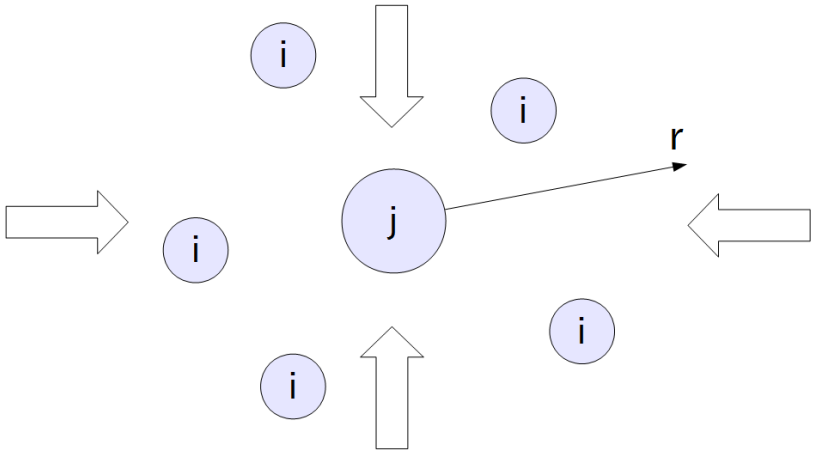

Figure 3.3.1: The schematic view of the flux and the coordinate system for Brownian aggregation. The radial axis is taken to the direction pointed out from a reference particle which is set on the origin.

We define the radii of ith and jth flocs as a_i and a_j, respectively. Since the ith flocs form $(i+j)$th flocs when aggregated, the boundary conditions are given by $n_i = 0$ at $r = a_i + a_j$, and $y(r) \to n_{i,b}$ as $r \to \infty$ where $n_{i,b}$ is the number concentration of the ith flocs in the bulk. From Eq.(3.3.7) and Eq.(3.3.9), we can obtain

$$dy = \frac{Z}{4\pi D_{ij} r^2} \exp\left(\frac{V^S}{k_B T}\right) dr. \tag{3.3.10}$$

By integrating Eq.(3.3.10) with the boundary conditions, we have

$$\begin{aligned} \int_0^{n_{i,b}} dy &= \int_{a_i+a_j}^{\infty} \frac{Z}{4\pi D_{ij} r^2} \exp\left(\frac{V^S}{k_B T}\right) dr \\ \Leftrightarrow Z &= 4\pi n_{i,b} \left[\int_{a_i+a_j}^{\infty} \frac{1}{4\pi D_{ij} r^2} \exp\left(\frac{V^S}{k_B T}\right) dr\right]^{-1}. \end{aligned} \tag{3.3.11}$$

There are many jth particles more than one in the bulk. Therefore, by multiplying the bulk number concentration of jth particles $n_{j,b}$ by Z, one obtains the collision frequency per unit volume between ith and jth flocs. That is,

$$Z n_{j,b} = 4\pi n_{i,b} n_{j,b} \left[\int_{a_i+a_j}^{\infty} \frac{1}{D_{ij} r^2} \exp\left(\frac{V^S}{k_B T}\right) dr\right]^{-1}. \tag{3.3.12}$$

We call the part other than $n_{i,b} n_{j,b}$ on the right hand side in Eq.(3.3.12) the Brownian aggregation rate coefficients $k_{ij,B}$

$$k_{ij,B} = 4\pi \left[\int_{a_i+a_j}^{\infty} \frac{1}{D_{ij} r^2} \exp\left(\frac{V^S}{k_B T}\right) dr\right]^{-1}. \tag{3.3.13}$$

The expression of D_{ij} taking into account hydrodynamic interactions is given by

$$D_{ij} = \frac{1}{B_{ij}(h)} \left(\frac{k_B T}{6\pi a_i \eta} + \frac{k_B T}{6\pi a_j \eta}\right), \tag{3.3.14}$$

with

$$B_{ij}(h) = \frac{6(h/a_{ij})^2 + 13(h/a_{ij}) + 2}{6(h/a_{ij})^2 + 4(h/a_{ij})}, \qquad a_{ij} = \frac{2a_i a_j}{a_i + a_j}. \tag{3.3.15}$$

$B_{ij}(h)$ is a non-dimensional function describing the hydrodynamic retardation due to the squeezing flow between particles when approaching[17, 18]. h is the particle sep-

aration distance expressed as $h = r - (a_i + a_j)$. With Eq.(3.3.14), Eq.(3.3.13) can be rewritten as follows

$$k_{ij,B} = \frac{2k_BT}{3\eta}\left(\frac{1}{a_i}+\frac{1}{a_j}\right)\left[\int_0^\infty \frac{B_{ij}(h)}{(h+a_i+a_j)^2}\exp\left(\frac{V^S(h)}{k_BT}\right)dh\right]^{-1} = \alpha_{ij,B}k_{ij,B}^{Smo}, \tag{3.3.16}$$

with

$$k_{ij,B}^{Smo} = \frac{2k_BT}{3\eta}\left(\frac{1}{a_i}+\frac{1}{a_j}\right)(a_i+a_j), \tag{3.3.17}$$

where $r = h+a_i+a_j$. Eq.(3.3.17) is the Brownian aggregation rate coefficients with any interactions formulated by Smoluchowski[12]. $\alpha_{ij,B}$ in Eq.(3.3.16) is called the capture efficiency for Brownian aggregation given as

$$\alpha_{ij,B} = \left[(a_i+a_j)\int_0^\infty \frac{B_{ij}(h)}{(h+a_i+a_j)^2}\exp\left(\frac{V^S(h)}{k_BT}\right)dh\right]^{-1}. \tag{3.3.18}$$

The capture efficiency $\alpha_{ij,B}$ expresses the effects of inter-particle interactions on aggregation and its inverse is called the stability ratio W normalized by the aggregation rate without any interactions. The stability ratio widely used experimentally is the one normalized by the aggregation rate k^f with only the van der Waals attraction in the absence of the electrostatic interactions[20, 36]. That is,

$$W = \frac{k^f}{k} = \frac{\int_0^\infty \frac{B_{ij}(h)}{(h+a_i+a_j)^2}\exp\left(\frac{V^S(h)}{k_BT}\right)dh}{\int_0^\infty \frac{B_{ij}(h)}{(h+a_i+a_j)^2}\exp\left(\frac{V^S_{vdW}(h)}{k_BT}\right)dh}, \tag{3.3.19}$$

where $V^S_{vdW}(h)$ is the van der Waals potential for spherical particles.

3.3.3 Hydrodynamic interactions in linear shear flows

In the previous section, we have shown the Brownian aggregation rate coefficients in quiescent fluid. However, aggregation happens in flow fields in many industrial processes such as food processing, water treatment, and so on. Thus, to formulate aggregation kinetics for particles immersed in a shearing fluid, we need to consider the particle velocity in the flow under the influence of hydrodynamic interactions between

colloidal particles.

Comprehensive formulations for hydrodynamic interactions have been done in a linear flow[15, 82, 83, 84, 85]. For further use, we summarize the particle velocity including the hydrodynamic interactions in two typical types of linear flow such as simple shear flow and axisymmetrical extensional flow as drawn in **Fig. 3.3.2**. Consider a linear flow $\boldsymbol{u}$ with the velocity gradient of $\nabla \boldsymbol{u} = G_{ij}$ as

$$u_i = G_{ij} x_j,\ G_{ij} = E_{ij} + \Omega_{ij}, \tag{3.3.20}$$

where $\boldsymbol{r} = x_j$ is the position vector, $\mathbf{E} = E_{ij} = \frac{1}{2}(G_{ij} + G_{ji})$ is the rate-of-strain tensor, and $\mathbf{\Omega} = \Omega_{ij} = \frac{1}{2}(G_{ij} - G_{ji})$ is the rate-of-rotation tensor. So, let us put two particles with radii of R_1 and R_2 at the origin and the position $\boldsymbol{r}$ in this linear shear flow field $\boldsymbol{u}$. Since the ambient linear flow is disturbed due to the existence of the particles and inter-particle hydrodynamic interactions, such disturbed flow can be given by the superposition of the ambient flow and the disturbed effect with hydrodynamic interactions. Thus, the relative velocity between the two particles $V_i(\boldsymbol{r})$ can be written as[82]

$$V_i(\boldsymbol{r}) = G_{ij} x_j - \left[\mathcal{A}(r,\rho)\frac{x_i x_j}{r^2} + \mathcal{B}(r,\rho)\left(\delta_{ij} - \frac{x_i x_j}{r^2}\right)\right] E_{jk} x_k, \tag{3.3.21}$$

where $\mathcal{A}(r,\rho)$ and $\mathcal{B}(r,\rho)$ are hydrodynamic interaction functions as described later. δ_{ij} is the Kronecker's delta.

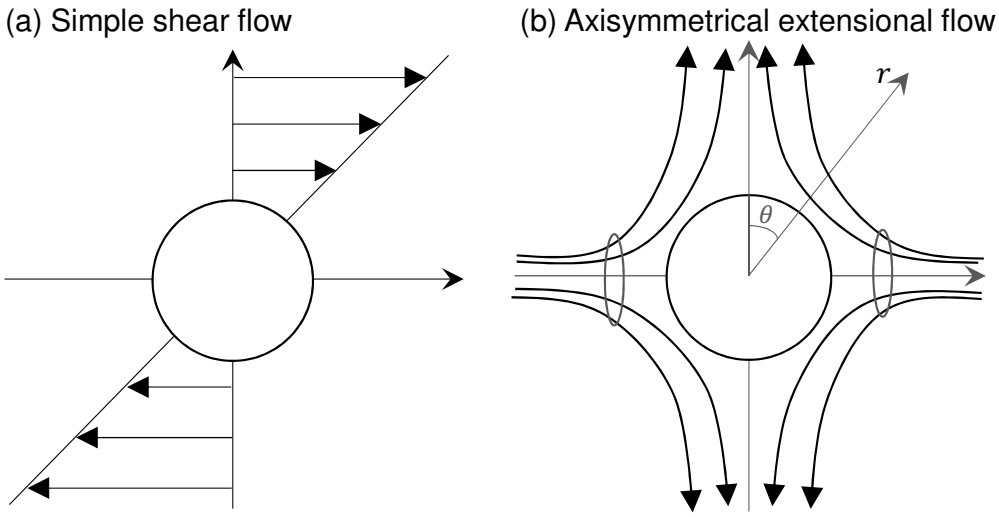

Figure 3.3.2: Schematic view of typical linear flows for (a)simple shear flow and (b)axisymmetrical extensional flow, respectively.

For simple shear flow $\boldsymbol{u} = Gx_2\boldsymbol{e_1}$, Eq.(3.3.21) can be rewritten

$$\begin{aligned}
\boldsymbol{V}(\boldsymbol{r}) = Gx_2\boldsymbol{e_1} &- \frac{\mathcal{A}(r,\rho)}{r^2}\begin{bmatrix} x_1^2 & x_1x_2 & x_1x_3 \\ x_2x_1 & x_2^2 & x_2x_3 \\ x_3x_1 & x_3x_2 & x_3^2 \end{bmatrix}\begin{bmatrix} \frac{1}{2}Gx_2 \\ \frac{1}{2}Gx_1 \\ 0 \end{bmatrix} - \mathcal{B}(r,\rho)\begin{bmatrix} 1 & 0 & 0 \\ 0 & 1 & 0 \\ 0 & 0 & 1 \end{bmatrix}\begin{bmatrix} \frac{1}{2}Gx_2 \\ \frac{1}{2}Gx_1 \\ 0 \end{bmatrix} \\
&- \frac{\mathcal{B}(r,\rho)}{r^2}\begin{bmatrix} x_1^2 & x_1x_2 & x_1x_3 \\ x_2x_1 & x_2^2 & x_2x_3 \\ x_3x_1 & x_3x_2 & x_3^2 \end{bmatrix}\begin{bmatrix} \frac{1}{2}Gx_2 \\ \frac{1}{2}Gx_1 \\ 0 \end{bmatrix} \\
= Gx_2\boldsymbol{e_1} &- \frac{\mathcal{A}(r,\rho)}{r^2}\left[Gx_1^2x_2\boldsymbol{e_1} + Gx_2^2x_1\boldsymbol{e_2} + Gx_1x_2x_3\boldsymbol{e_3}\right] \\
&- \mathcal{B}(r,\rho)\left[\frac{1}{2}Gx_2\boldsymbol{e_1} + \frac{1}{2}Gx_1\boldsymbol{e_2}\right] \\
&+ \frac{\mathcal{B}(r,\rho)}{r^2}\left[Gx_1^2x_2\boldsymbol{e_1} + Gx_2^2x_1\boldsymbol{e_2} + Gx_1x_2x_3\boldsymbol{e_3}\right]. \qquad (3.3.22)
\end{aligned}$$

Here, the relative position between the two particles can be described in the Cartesian coordinate (x_1, x_2, x_3) or the spherical coordinate (r, θ, ϕ) with the relationship between them given by

$$x_1 = r\sin\theta\cos\phi,\ \ x_2 = r\sin\theta\sin\phi,\ \ x_3 = r\cos\theta, \qquad (3.3.23)$$

$$\boldsymbol{e_1} = \boldsymbol{e_r}\sin\theta\cos\phi + \boldsymbol{e_\theta}\cos\theta\cos\phi - \boldsymbol{e_\phi}\sin\phi, \qquad (3.3.24)$$

$$\boldsymbol{e_2} = \boldsymbol{e_r}\sin\theta\sin\phi + \boldsymbol{e_\theta}\cos\theta\sin\phi + \boldsymbol{e_\phi}\cos\phi, \qquad (3.3.25)$$

$$\boldsymbol{e_3} = \boldsymbol{e_r}\cos\theta - \boldsymbol{e_\theta}\sin\theta. \qquad (3.3.26)$$

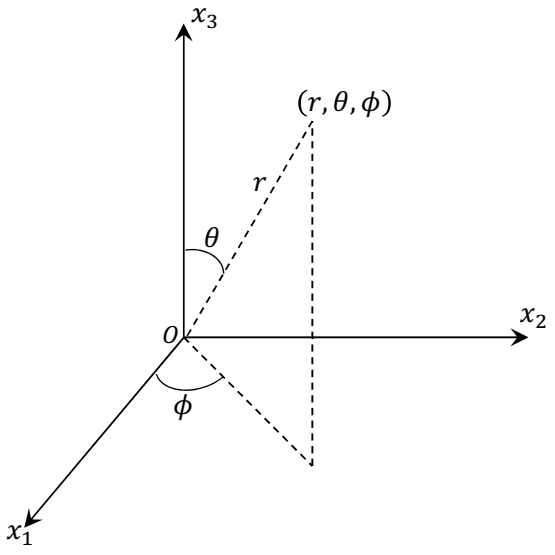

Figure 3.3.3: Schematic representation of Cartesian and spherical polar coordinate systems.

By using these relationships, we can write Eq.(3.3.22) as

$$\begin{aligned}\boldsymbol{V}(\boldsymbol{r}) = \boldsymbol{e_r}\left[Gr(1-\mathcal{A}(r,\rho))\sin^2\theta\sin\phi\cos\phi\right]\\ +\boldsymbol{e_\theta}\left[Gr(1-\mathcal{B}(r,\rho))\sin\theta\sin\phi\cos\theta\cos\phi\right]\\ +\boldsymbol{e_\phi}\left[-Gr\sin\theta\left\{\sin^2\phi+\frac{\mathcal{B}(r,\rho)}{2}\left(\cos^2\phi-\sin^2\phi\right)\right\}\right].\end{aligned} \tag{3.3.27}$$

With Eq.(3.3.27), we can calculate the relative particle velocity of two particles in a simple shear flow in the spherical coordinate (r,θ,ϕ).

Next, for pure straining flow, let E_1, E_2, E_3 to be the three principal rates of strain of the bulk flow, where $E_1 \leq E_2 < E_3$ of which only two are independent because of mass conservation law. That is, the sum of them must be zero. With the velocity $\boldsymbol{u} = E_1x_1\boldsymbol{e_1} + E_2x_2\boldsymbol{e_2} + E_3x_3\boldsymbol{e_3}$, Eq.(3.3.21) can be rewritten in a similar way derived Eq.(3.3.27) as

$$\begin{aligned}\boldsymbol{V}(\boldsymbol{r}) = \boldsymbol{e_r}\left[r(1-\mathcal{A}(r,\rho))\{E_3\cos^2\theta+(E_1\cos^2\phi+E_2\sin^2\phi)\sin^2\theta\}\right]\\ +\boldsymbol{e_\theta}\left[r(1-\mathcal{B}(r,\rho))\sin\theta\cos\theta\{E_1-E_3+(E_2-E_1)\sin^2\phi\}\right]\\ +\boldsymbol{e_\phi}\left[r(1-\mathcal{B}(r,\rho))\sin\phi\cos\phi\{E_2-E_1\}\sin\theta\right].\end{aligned} \tag{3.3.28}$$

For axisymmetrical extensional flow with $E_1 = E_2 = -G$, $E_3 = 2G$, Eq.(3.3.28) can be reduced to the following equation

$$\begin{aligned}\boldsymbol{V}(\boldsymbol{r}) = \boldsymbol{e_r}\left[Gr(1-\mathcal{A}(r,\rho))\{3\cos^2\theta-1\}\right]\\ +\boldsymbol{e_\theta}\left[-3Gr(1-\mathcal{B}(r,\rho))\sin\theta\cos\theta\right].\end{aligned} \tag{3.3.29}$$

We use these velocity distributions to calculate the shear aggregation rate coefficients in the following sections.

3.3.4 Aggregation rate coefficients in a simple shear flow

Aggregation rate coefficients in a simple shear flow has been derived by considering the relative motion of colliding particles due to the velocity gradient in the surrounding fluid[12]. Such relative motion can be calculated by using the trajectory analysis based on hydrodynamics[35, 37, 86]. We show the schematic representation of the trajectory analysis as depicted in **Fig. 3.3.4**. Let us consider the two particles with the radii

of R_i and R_j in a simple shear flow with the velocity field of $u_y = Gx$. Neglecting the Brownian motion of the particles, the particle relative motion is determined in a deterministic way. In this situation, the relative trajectory of the reference particle j and the colliding one i can be determined by the balance of the physico-chemical and hydrodynamic interactions. Therefore, the collision frequency between the particles i and j can be calculated as the number of particles per unit time flowing into the cross section through which the trajectories passes to finally collide and form the aggregate, so-called the capture cross section, on the $x-z$ plane sufficiently away from the reference particle. That is,

$$Z = 4GN_i \int_0^{z_{max}} \int_0^{x_c(z')} x' dx' dz' \tag{3.3.30}$$

where $x_c(z)$ is the shape of the boundary of the capture cross section separating the trajectories whether aggregation happen or not. z_{max} is the maximum value of z on the capture cross section. It means the capture cross section is characterized by $x_c(z)$ and z_{max}. Hence, its expression per unit volume is given by

$$ZN_j = 2GN_iN_j \int_0^{z_{max}} [x_c(z')]^2 dz'. \tag{3.3.31}$$

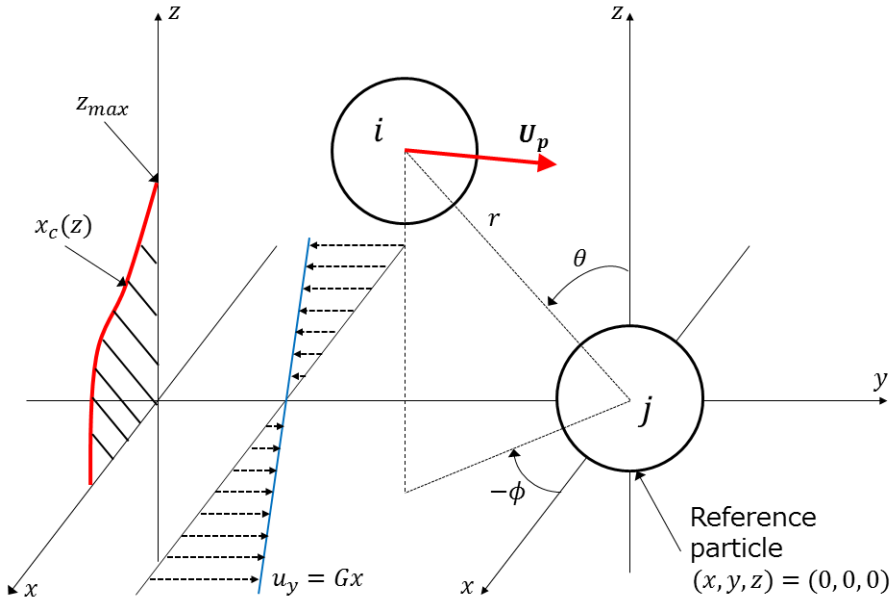

Figure 3.3.4: Schematic representation of a trajectory analysis. $\boldsymbol{U_p}$ the particle relative velocity described by Eqs.(3.3.36-3.3.38), $x_c(z)$ the boundary between aggregation or not on $x-z$ plane at the released point($y = -100R_i$), and z_{max} the maximum of z on the boundary, respectively.

Therefore, in a similar manner for Brownian diffusion, the aggregation rate coefficients in a simple shear flow can be expressed by the following equation

$$k_{ij,sh} = 2G \int_0^{z_{max}} [x_c(z')]^2 dz'. \tag{3.3.32}$$

In the absence of any inter-particle interactions, the particle trajectory follows the streamline of the shear flow without being disturbed by the existence of each other. This case corresponds to the one with $x_c(z) = \sqrt{(R_i + R_j)^2 - z^2}$ and $z_{max} = R_i + R_j$ in Eq.(3.3.32). Thus, the aggregation rate coefficients without any interactions $k_{ij,sh}^{Smo}$ is given by[12]

$$k_{ij,sh}^{Smo} = \frac{4}{3} G (R_i + R_j)^3. \tag{3.3.33}$$

By using Eq.(3.3.33), Eq.(3.3.32) can be rewritten as

$$k_{ij,sh} = \alpha_{ij,sh} \frac{4}{3} G (R_i + R_j)^3, \tag{3.3.34}$$

with

$$\alpha_{ij,sh} = \frac{3}{2(R_i + R_j)^3} \int_0^{z_{max}} [x_c(z')]^2 dz', \tag{3.3.35}$$

where $\alpha_{ij,sh}$ is the capture efficiency for aggregation in a simple shear flow. $\alpha_{ij,sh}$ can be regarded as the ratio of finally aggregating particles among the particles flowing into the capture cross section in the case without any interactions.

To calculate the capture efficiency, let us explain briefly to determine $x_c(z)$ and z_{max} which characterize the capture cross section by using the trajectory analysis. As mentioned above, neglecting the Brownian diffusion, the relative colliding trajectory between two particles can be determined in a deterministic way, and it can be described by the following trajectory equations[87]

$$\begin{aligned} \frac{dr^*}{dt^*} &= r^*(1 - \mathcal{A}(r^*, \rho)) \sin^2\theta \sin\phi \cos\phi \\ &\quad + \frac{\mathcal{G}(r^*, \rho)}{6\pi\eta G R_i^2} (F_{vdW} + F_{edl}), \end{aligned} \tag{3.3.36}$$

$$\frac{d\theta}{dt^*} = (1 - \mathcal{B}(r^*, \rho)) \sin\theta \cos\theta \sin\phi \cos\phi, \tag{3.3.37}$$

$$\frac{d\phi}{dt^*} = \cos^2\phi - \frac{\mathcal{B}(r^*, \rho)}{2} \cos 2\phi, \tag{3.3.38}$$

where $r^* = r/R_i$ ($R_i >= R_j$) is the non-dimensional distance between particle centers, $\rho = R_j/R_i$ is the size ratio, and $t^* = Gt$ is the non-dimensional time. $\mathcal{A}(r^*, \rho)$, $\mathcal{B}(r^*, \rho)$, and $\mathcal{G}(r^*, \rho)$ are the hydrodynamic interaction functions depending on r^* and ρ. F_{vdW} and F_{edl} in Eq.(3.3.36) are the van der Waals attractive and electrostatic interaction forces, respectively. The hydrodynamic parts in these equations are equivalent to ones in Eq.(3.3.27), but look different because of the different direction of the ambient simple shear flow.

$\mathcal{A}(r^*, \rho)$, $\mathcal{B}(r^*, \rho)$, and $\mathcal{G}(r^*, \rho)$ at long separation distances can be expressed as follows[17, 82].

$$\mathcal{A}(r^*, \rho) = \frac{5(1+\rho^3)}{2r^{*3}} - \frac{3(1+\rho^5)+5\rho^2(1+\rho)}{2r^{*5}} + \frac{25\rho^3}{r^{*6}}, \tag{3.3.39}$$

$$\mathcal{B}(r^*, \rho) = \frac{1+\rho^5+(5/3)\rho^2(1+\rho)}{r^{*5}}, \tag{3.3.40}$$

$$\mathcal{G}(r^*, \rho) = 1 + \frac{1}{\rho}. \tag{3.3.41}$$

In the case of equal-sized particles $\rho = 1$, $\mathcal{A}(r^*, \rho)$, $\mathcal{B}(r^*, \rho)$, and $\mathcal{G}(r^*, \rho)$ at short separation distances are given by [82, 87].

$$\mathcal{A}(r^*, \rho) = 1 - 4.077h^*, \tag{3.3.42}$$

$$\mathcal{B}(r^*, \rho) = 0.4060 + \frac{0.78}{\ln h^*}, \tag{3.3.43}$$

$$\mathcal{G}(r^*, \rho) = 4h^*(1 + 1.34h^* \ln h^*), \tag{3.3.44}$$

where $h^* = r^* - \rho - 1$ is the normalized surface separation distance. In this thesis, we employed the interpolated functions of $\mathcal{A}(r^*, \rho)$, $\mathcal{B}(r^*, \rho)$, and $\mathcal{G}(r^*, \rho)$ for intermediate separation distances tabulated by Wang[88].

The time evolution of the relative position of two particles can be calculated by integrating Eqs.(3.3.36-3.3.38). To solve the set of these ordinary differential equations, we use the fourth-order Runge-Kutta method. Changing released points of a particle from $x-z$ plane at $y^* = y/R = -100$ in the velocity field $u_y = Gx$, each trajectory from a release point is judged whether aggregation occurs or not in a deterministic way. The calculation is stopped when the relative position of the particles results in one of the following three cases as (i) $r^* - \lambda - 1 < \epsilon^* = \epsilon/R$, where ϵ is the minimum separation, (ii) $\phi > \pi/2$, or (iii) $y^* = 10$. The former two cases (i) and (ii) correspond to aggregation. The last case (iii) means that each particle is separated and no aggregation occurs. In the present study, $\epsilon^* = 10^{-7}$ was adopted to avoid computational divergence[89].

3.3.5 Turbulent aggregation rate coefficients

The turbulent aggregation rate coefficients can be derived by considering the particle flux to the reference particle as described above. The aggregation rate coefficients in a homogeneous isotropic turbulence has been formulated by Saffman and Turner (1956)[13]. First, let us consider the case without inter-particle interactions where particles move along with the fluid stream line. According to the Kolmogoroff's hypothesis of locally isotropic turbulence, the orientational information of flow is lost as the energy cascade process proceeds to smaller eddies in a well-developed turbulence. The transferred energy is finally dissipated to heat in the smallest eddies. The flow in the local scale becomes isotropic independent of the flow direction in the large scale turbulence. If particle collisions happen in the smallest eddies which are often larger than colloidal length scales, we can assume that the surrounding flow field is a homogeneous isotropic turbulence. As in the case of the Brownian aggregation, we take the coordinate system outward from the center of a jth floc. With the collision radius of $R_c = a_i + a_j$, the turbulent aggregation rate coefficients can be calculated by the averaged flow rate passing inward through the spherical surface S with the radius of R_c located around the center of jth flocs

$$k_{ij}^{ST} = -\overline{\int_{w_r<0} w_r dS}, \tag{3.3.45}$$

where w_r is the velocity difference in the radial direction between the origin and the surface S, and the upper bar means the average over all possible motion. The minus sign on the right-hand side is for making influx positive since the radial component of the velocity against the inflow is $w_r < 0$ with the coordinate system taken outward. The product of Eq.(3.3.45) and $N_i N_j$ is the collision frequency per unit volume between ith and jth flocs. In an isotropic turbulence, since there is no correlation between the particle position and the nature of turbulence, the average in the above equation is equal to the one at the fixed point in space.

To obtain an analytical expression for the turbulent aggregation rate coefficients, one needs to evaluate the integral in Eq.(3.3.45). First, from the equation of continuity, we

have the following equation:

$$\int_{w_r<0} w_r dS + \int_{w_r>0} w_r dS = 0. \tag{3.3.46}$$

Eq.(3.3.46) means that even if the fluid is moving at random with the relative radial velocity taking various positive and negative values on the surface S, the net flow rate on S is always zero. This indicates that the inflow and outflow have a same absolute value, but the opposite sign. Using the facts that $|w_r| = -w_r$ if $w_r < 0$ and $|w_r| = w_r$ if $w_r > 0$, the surface integral for the absolute value of w_r on the surface S is given by

$$\begin{aligned}\int_S |w_r| dS &= \int_{w_r<0} |w_r| dS + \int_{w_r>0} |w_r| dS \\ &= -\int_{w_r<0} w_r dS + \int_{w_r>0} w_r dS \\ &= -2\int_{w_r<0} w_r dS,\end{aligned}$$

where we used the equation of continuity, Eq.(3.3.46). Therefore, by taking the average of the above equation, Eq.(3.3.45) can be evaluated as follows

$$\begin{aligned}k_{ij}^{ST} &= \frac{1}{2}\overline{\int_S |w_r| dS} = \frac{1}{2}\int_S \overline{|w_r|} dS \\ &= 2\pi R_c^2 \overline{|w_r|}.\end{aligned} \tag{3.3.47}$$

In Eq.(3.3.47), we use the commutativity of the surface integral and average, and the fact that the average is constant irrespective of the position on the surface S since the average in Eq.(3.3.45) is equal to the one at the fixed point in space in an isotropic turbulence.

When the collision radius is smaller than the Kolmogoroff microscale of turbulence, we can write $\overline{|w_r|} = R_c \overline{|\frac{\partial u_r}{\partial r}|}$ where $\overline{|\frac{\partial u_r}{\partial r}|}$ is the averaged absolute value of the longitudinal derivative for the radial velocity component. According to Taylor's isotropic turbulence theory, the mean square of the longitudinal derivative for the radial velocity component is given by

$$\overline{\left(\frac{\partial u_r}{\partial r}\right)^2} = \frac{\epsilon_{\mathrm{T}}}{15\nu}, \tag{3.3.48}$$

where ϵ_{T} is the turbulent energy dissipation rate per unit mass, ν is the kinematic viscosity. This implies that the extensional component in the flow is more dominant for the energy dissipation. From the isotropy, we have

$$\overline{\frac{\partial u_r}{\partial r}} = 0. \tag{3.3.49}$$

With Eq.(3.3.49), we know that the variance of $\frac{\partial u_r}{\partial r}$ is equal to Eq.(3.3.48). From the experimental result by Townsend[90], one assumes that $\frac{\partial u_r}{\partial r}$ approximately follows the normal distribution. With these assumptions, the probability density function $P\left(\frac{\partial u_r}{\partial r}\right)$ of $\frac{\partial u_r}{\partial r}$ can be described by the following equation

$$P\left(\frac{\partial u_r}{\partial r}\right) = \frac{1}{\sqrt{2\pi}\sqrt{\epsilon_{_T}/(15\nu)}} \exp\left[-\frac{\left(\frac{\partial u_r}{\partial r}\right)^2}{2\epsilon_{_T}/(15\nu)}\right]. \tag{3.3.50}$$

Let us calculate $\overline{|\frac{\partial u_r}{\partial r}|}$ with Eq.(3.3.50)

$$\begin{aligned}
\overline{\left|\frac{\partial u_r}{\partial r}\right|} &= \int_{-\infty}^{\infty} \left|\frac{\partial u_r}{\partial r}\right| \frac{1}{\sqrt{2\pi}\sqrt{\epsilon_{_T}/(15\nu)}} \exp\left[-\frac{\left(\frac{\partial u_r}{\partial r}\right)^2}{2\epsilon_{_T}/(15\nu)}\right] d\left(\frac{\partial u_r}{\partial r}\right) \\
&= \int_{0}^{\infty} \left|\frac{\partial u_r}{\partial r}\right| \frac{1}{\sqrt{2\pi}\sqrt{\epsilon_{_T}/(15\nu)}} \exp\left[-\frac{\left(\frac{\partial u_r}{\partial r}\right)^2}{2\epsilon_{_T}/(15\nu)}\right] d\left(\frac{\partial u_r}{\partial r}\right) \\
&+ \int_{-\infty}^{0} \left|\frac{\partial u_r}{\partial r}\right| \frac{1}{\sqrt{2\pi}\sqrt{\epsilon_{_T}/(15\nu)}} \exp\left[-\frac{\left(\frac{\partial u_r}{\partial r}\right)^2}{2\epsilon_{_T}/(15\nu)}\right] d\left(\frac{\partial u_r}{\partial r}\right).
\end{aligned}$$

With the property of the absolute value, we can calculate the first term on the right-hand side as

$$\text{(First term)} = \int_{0}^{\infty} \frac{\partial u_r}{\partial r} \frac{1}{\sqrt{2\pi}\sqrt{\epsilon_{_T}/(15\nu)}} \exp\left[-\frac{\left(\frac{\partial u_r}{\partial r}\right)^2}{2\epsilon_{_T}/(15\nu)}\right] d\left(\frac{\partial u_r}{\partial r}\right).$$

For the second term,

$$\begin{aligned}
\text{(Second term)} &= \int_{-\infty}^{0} \left|\frac{\partial u_r}{\partial r}\right| \frac{1}{\sqrt{2\pi}\sqrt{\epsilon_{_T}/(15\nu)}} \exp\left[-\frac{\left(\frac{\partial u_r}{\partial r}\right)^2}{2\epsilon_{_T}/(15\nu)}\right] d\left(\frac{\partial u_r}{\partial r}\right) \\
&= -\int_{\infty}^{0} \frac{\partial u_r}{\partial r} \frac{1}{\sqrt{2\pi}\sqrt{\epsilon_{_T}/(15\nu)}} \exp\left[-\frac{\left(\frac{\partial u_r}{\partial r}\right)^2}{2\epsilon_{_T}/(15\nu)}\right] d\left(\frac{\partial u_r}{\partial r}\right) \\
&= \int_{0}^{\infty} \frac{\partial u_r}{\partial r} \frac{1}{\sqrt{2\pi}\sqrt{\epsilon_{_T}/(15\nu)}} \exp\left[-\frac{\left(\frac{\partial u_r}{\partial r}\right)^2}{2\epsilon_{_T}/(15\nu)}\right] d\left(\frac{\partial u_r}{\partial r}\right).
\end{aligned}$$

Hence, we have

$$\overline{\left|\frac{\partial u_r}{\partial r}\right|} = 2\int_0^\infty \frac{\partial u_r}{\partial r}\frac{1}{\sqrt{2\pi}\sqrt{\epsilon_T/(15\nu)}}\exp\left[-\frac{\left(\frac{\partial u_r}{\partial r}\right)^2}{2\epsilon_T/(15\nu)}\right] d\left(\frac{\partial u_r}{\partial r}\right).$$

Using the relation with the variance σ^2 as

$$\frac{1}{\sqrt{2\pi\sigma^2}}\int_0^\infty x\exp\left(-\frac{x^2}{2\sigma^2}\right)dx = \frac{\sigma}{\sqrt{2\pi}}. \tag{3.3.51}$$

One obtains

$$\overline{\left|\frac{\partial u_r}{\partial r}\right|} = \frac{2}{\sqrt{2\pi}}\sqrt{\frac{\epsilon_T}{15\nu}} = \sqrt{\frac{2\epsilon_T}{15\pi\nu}}. \tag{3.3.52}$$

By substituting this result Eq.(3.3.52) into Eq.(3.3.47), we can obtain the turbulent aggregation rate coefficients without any interactions as follows

$$k_{ij}^{ST} = 2\pi R_c^3\sqrt{\frac{2\epsilon_T}{15\pi\nu}} = R_c^3\sqrt{\frac{8\pi\epsilon_T}{15\nu}}. \tag{3.3.53}$$

The turbulent aggregation rate coefficients including inter-particle interactions $k_{ij,T}$ can be expressed as the product of Eq.(3.3.53) and the capture efficiency $\alpha_{ij,T}$. That is,

$$k_{ij,T} = \alpha_{ij,T}k_{ij}^{ST} = \alpha_{ij,T}R_c^3\sqrt{\frac{8\pi\epsilon_T}{15\nu}}. \tag{3.3.54}$$

In this thesis, we calculate the capture efficiency $\alpha_{ij,T}$ by the trajectory analysis as introduced above, even though the trajectory analysis is strictly valid in a shear flow. However, we apply the trajectory analysis to the turbulent coagulation as a first approximation because the flow in the smallest eddies of a turbulence is expected to be analogous to the shear flow with a mean local shear rate in the turbulence[38] as mentioned above. This assumption is presumable if the length scale where coagulation occurs is smaller than the scale in the smallest eddies. This expansion of the trajectory analysis to the turbulent aggregation has been done by Higashitani for the first time[38]. The validity of this approximation has been confirmed by previous researchers in the case where no electrostatic interaction[6, 38, 39, 40].

In this chapter, we have summarized the basic concepts of electrophoresis such as the relaxation effect and aggregation rate coefficients used in the following chapters. First

of all, we apply these expressions to analyze electrophoretic mobilities and aggregation rates in a simple shear flow for model colloidal particles with surface sulfate groups in next Chapter 4.

Chapter 4

Effect of ionic strength and shear rate on aggregation in a shear flow

4.1 Introduction

In the previous chapters, so far, we have summarized fundamental theoretical concepts used in this thesis.

As mentioned above, aggregation processes are basically determined by the physicochemical interaction and the collision mode between the particles[2]. The former is mainly composed of the van der Waals (vdW) attraction and the electrical double layer repulsion. The net force can be given by the sum of these interaction forces according to the classical theory by the Derjaguin-Landau-Verwey-Overbeek (DLVO), so-called the DLVO theory[4, 5]. The collision mode is composed of the collision due to Brownian motion in quiescent fluid and the velocity difference in fluid such as laminar shear and turbulent flow[6, 7, 8, 9, 10, 11].

Theoretical formulation for aggregation kinetics by Brownian motion and a laminar shear flow was undertaken by Smoluchowski[12]. Unfortunately, Smoluchowski's formulation neglects any interactions, although the colliding particles hydrodynamically and physicochemically interact with each other in more realistic systems. Without any

interaction, the trajectory of colliding particles is rectilinear. On the contrary, the collision trajectory with inter-particle interaction becomes curvilinear. Taking into account the physicochemical and hydrodynamic interactions, one can modify the Smoluchowski collision rate Z_{Smol} for identical particles with a radius of R in a simple shear flow with a shear rate of G as

$$Z = \alpha Z_{Smol}, \tag{4.1.1}$$

where $Z_{Smol} = 32R^3GN_0/3$, N_0 and α are the initial total number concentration of the particles and a capture efficiency, respectively. The capture efficiency α reflects the effect of hydrodynamic and physicochemical interactions between the particles on the aggregation rate. The capture efficiency has been numerically calculated with trajectory analysis by many researchers[36, 37, 35, 86, 87, 88, 89, 46, 47].

So far, however, the previous researchers computed the trajectory by using the double layer repulsion based on the linearized Poisson-Boltzmann equation, which is only applicable under the condition where electric potential between the particle surfaces is low. That is, the previously calculated results can not be applied to the aggregation of particles with high surface potential often faced in the realistic case. Moreover, the theoretical calculations with the trajectory analysis in the presence of the double layer repulsion have not been quantitatively compared with the systematic experimental data taken using the well-characterized colloidal particles. On the contrary, the kinetic theory in Brownian coagulation has shown that it is quantitatively consistent with the experimental data in some limited conditions[23]. Here, we focus on the experimental data by Sato *et al.*[41]. They measured the capture efficiencies as a function of KCl concentration in a simple shear flow using the well-characterized and highly charged latex particles. Their experimental data are systematically taken in well-defined system and include the rates in the presence of the repulsive double layer forces. Nevertheless, their data have not been substantially analyzed due to the problem of the previous calculation which assumes the low potential condition in the evaluation of the electrical repulsion. Therefore, the kinetics of aggregation in flow fields has not yet been subjected to intense study in spite of its scientific and practical importance.

In the present study, we calculate the capture efficiency of charged colloidal particles in a simple shear flow on the basis of hydrodynamic trajectory analysis incorporating

the double layer repulsion with the exact non-linear Poisson-Boltzmann solution in the symmetrical electrolyte solution. Furthermore, from the comparison between theoretical and experimental values in the well-defined system, we discuss the validity of the theory with trajectory analysis for the shear-induced aggregation. It should be noted that such comparisons have never been attempted in the presence of the double layer repulsion.

4.2 Experiments

4.2.1 Materials

In the present study, we analyze the experimental data of aggregation rate of polystyrene sulfate latex (PSL) particles with two different diameters of 1.96 and 2.8 μm by Sato *et al.*[41]. The smaller particles were synthesized by means of surfactant-free aqueous polymerization. The larger particles were purchased from Interfacial Dynamic Corporation. These PSL particles with the density of 1.055 g/cm^3 are spherical, monodisperse and have the sulfate head-groups on the surface which are strong acid. The surfaces are thus considered to be negatively charged with a constant surface charge density irrespective of pH and ionic strength. On the one hand, the magnitude of surface potential decreases with increasing ionic strength by screening effect. The surface charge densities for the larger and smaller particles were known to be $\sigma = -70$ mC/m^2 reported by the manufacturer and $\sigma = -60$ mC/m^2 taken from the literature[41], respectively. The ionic strength was controlled by KCl solution. More details of these particles are found in elsewhere[41]. All experiments were carried out at 20 ℃.

4.2.2 Electrophoresis

Electrophoretic mobility of these particles was measured as a function of KCl concentration by using a laser Doppler velocimetry setup (ZetaSizer Nano ZS and 2000, Malvern) to confirm the validity of the standard electrokinetic model described above. The experimental procedures are as follows. Firstly, the colloidal suspensions were prepared by mixing the required amount of stock latex suspension, KCl solution, and pure

water. Secondary, the suspensions were injected into the cell for electrophoretic measurement. Finally, the cell was set in the instrument and the electrophoretic mobility was measured.

4.2.3 Aggregation in a shear flow

Aggregation experiments in a simple shear flow were performed by using a Couette flow device composed of two concentric cylinders. The Couette flow device generates steady laminar shear flows in the gap between the two cylinders by rotating the outside cylinder. Changing the revolution speed of the outer cylinder Ω, the averaged shear rate in the gap G_{ave} can be controlled and calculated by

$$G_{ave} = \frac{4\Omega}{\left(\frac{1}{r_1^2} - \frac{1}{r_2^2}\right)(r_2^2 - r_1^2)}, \tag{4.2.1}$$

where r_1 and r_2 are the outer radius of the inside cylinder and the inner radius of the outside cylinder, respectively. The value of G_{ave} is used as G in Eq.(3.3.36) in the trajectory analysis. The aggregation experiments of the particles were carried out as a function of KCl concentration. The required amounts of latex suspension, KCl solution, and pure water were mixed and immediately poured into the gap in the Couette flow device. Then, the suspension was subjected to a shear flow with three shear rates of $G = 23,\ 46,\ 92\ \mathrm{s}^{-1}$. The rotation was stopped in a certain period of time and the suspension was sampled to measure the total particle number concentration $N(t)$ at elapsed time t by a Coulter particle counter. From the measured relationship between $N(t)$ and t, the capture efficiency α can be obtained with the following expression by assuming the constant volume fraction of particles in the early stage of aggregation process[41]

$$\ln\left[\frac{N(t)}{N_0}\right] = -\alpha\frac{4\phi G}{\pi}t, \tag{4.2.2}$$

where ϕ is the volume fraction of particles in the suspension. These experiments were performed at low volume fraction ϕ of $0.4 - 3.8 \times 10^{-5}$. Therefore, we assume that the effect of volume fraction on the flow field is negligible.

4.3 Theory

4.3.1 Electrophoretic mobility and zeta potential

Electrophoresis has been extensively used to study the charging behavior of colloidal particles[23, 72]. We thus adopt the electrophoresis to evaluate the charging properties of colloidal particles, such as surface charge density and potential, through the analysis of experimental data by a standard electrokinetic model as described below.

With the Poisson-Boltzmann equation in 1:1 (symmetrical) electrolyte solution, the surface charge density σ can be related to the surface potential $\psi_{_{0,iso}}$ for the isolated particle surface as[91]

$$\sigma = \frac{2\epsilon_r\epsilon_0\kappa k_B T}{e}\sinh\left(\frac{e\psi_{_{0,iso}}}{2k_B T}\right), \tag{4.3.1}$$

with

$$\kappa = \sqrt{\frac{2C_b e^2}{\epsilon_r\epsilon_0 k_B T}}, \tag{4.3.2}$$

where $\epsilon_r\epsilon_0$, κ, C_b, k_B, T, and e are the permittivity of the medium, the Debye parameter, the bulk concentration of the electrolyte, the Boltzmann constant, absolute temperature, and the elementary charge, respectively. κ^{-1} is usually called the Debye length which is the measure of the thickness of electrical diffuse double layer.

The electrophoretic mobility $\mu_{_m}$ is defined as the ratio of translational velocity of a particle U induced by the applied electric field and the magnitude of the applied electric field E in a solution.

$$\mu_{_m} = \frac{U}{E}. \tag{4.3.3}$$

Assuming that the surface charge density is constant which is fulfilled for the sulfate latex particles used in Sato's study, the surface potential is determined from Eq.(4.3.1). The evaluated surface potential can be used to calculate electrophoretic mobility $\mu_{_m}$ if the $\psi_{_{0,iso}}$ equals to the zeta potential ζ which is defined as an electrical potential at the outer end of immobile fluid layer near the surface. The electrophoretic mobility $\mu_{_m}$ in a solution with a viscosity η is often calculated using the Helmholtz-Smoluchowski equation, which is also simply called the Smoluchowski equation, given by the following

equation as described above

$$\mu_m = \frac{\epsilon_r \epsilon_0}{\eta}\zeta. \tag{4.3.4}$$

This equation is conveniently used to transform the experimental electrophoretic mobility to ζ because the relationship is linear and simple. However, it is not readily applicable to the case of high ζ where the relationship between the electrophoretic mobility and ζ becomes non-linear by the relaxation effect which gives rise to the appearance of the minimum/maximum electrophoretic mobility by decreased translational velocity of a particle due to the deformation of electrical double layer. The deformation is caused by the motion of counter-ion due to the applied electric field in the opposite direction of particle motion and becomes more significant with increasing the surface potential and decreasing the salt concentration. The non-linear relationship has been confirmed using the theoretical computation by O'Brien and White[71], and a number of experimental studies[23, 72, 73].

Approximate analytical expressions of electrophoretic mobility including the relaxation effect for a sphere have been proposed by Ohshima[75, 76]. In the present study, we use Ohshima's equations because they are accurate when κR is larger than 10. The large κR means that the particle radius is considerably larger than the thickness of the double layer. This condition is satisfied in Sato's study. In the 1:1 symmetrical electrolyte solution such as KCl, the analytical expression of electrophoretic mobility μ_m is given by

$$\mu_m = \mathrm{sgn}(\zeta)\frac{\epsilon_r \epsilon_0}{\eta}\left\{|\zeta| + \left(\frac{k_B T}{e}\right)\left[-\frac{2F}{1+F}H + \frac{\mathcal{M}}{\kappa R}\right]\right\}, \tag{4.3.5}$$

with

$$F = \frac{2}{\kappa R}(1+3m_+)\{\exp(e|\zeta|/(2k_B T)) - 1\}, \tag{4.3.6}$$

$$H = \ln\left[\frac{1+\exp(e|\zeta|/(2k_B T))}{2}\right], \tag{4.3.7}$$

$$\begin{aligned}\mathcal{M} = &-18\left(t + \frac{t^3}{9}\right) + \frac{15F}{1+F}\left(t + \frac{7t^2}{20} + \frac{t^3}{9}\right) - 6(1+3m_-)(1-\exp(-|\tilde{\zeta}|/2))I \\ &+\frac{12F}{(1+F)^2}H + \frac{9|\tilde{\zeta}|}{1+F}(m_- I + m_+ H) - \frac{36F}{1+F}\left(m_- I^2 + \frac{m_+}{1+F}H^2\right),\end{aligned} \tag{4.3.8}$$

$$\tilde{\zeta} = e\zeta/(k_B T), \tag{4.3.9}$$

$$t = \tanh(|\tilde{\zeta}|/4), \tag{4.3.10}$$

$$K = 1 - \frac{25}{3(\kappa R + 10)} \exp\left(-\frac{\kappa R}{6(\kappa R - 6)}|\tilde{\zeta}|\right), \tag{4.3.11}$$

$$I = \ln\left[\frac{1 + \exp(-|\tilde{\zeta}|/2)}{2}\right], \tag{4.3.12}$$

$$m_{+} = \frac{2\epsilon_r \epsilon_0 k_B T}{3\eta e^2}\lambda_{+}, \tag{4.3.13}$$

where $\tilde{\zeta}$ is the non-dimensional ζ potential, sgn(ζ) is a function defined as -1 when $\zeta < 0$ and $+1$ when $\zeta \geq 0$. Also, m_{+} and λ_{+} are the scaled drag coefficient of counter-ion and the drag coefficient of the counter ion species, and m_{-} is the scaled drag coefficient of co-ion defined by Eq.(4.3.13) replacing λ_{+} to λ_{-} respectively. The third term in Eq.(4.3.5) including a function of $\mathcal{M}$ can be neglected when κR is considerably large. The ionic drag coefficient $\lambda_{\pm}$ is defined as

$$\lambda_{\pm} = \frac{N_A e^2 |z_{\pm}|}{\Lambda^0_{\pm}}, \tag{4.3.14}$$

where N_A, $z_{\pm}$, and $\Lambda^0_{\pm}$ are Avogadro's number, the ion valence, the limiting conductance of the each ionic species, respectively. To calculate the electrophoretic mobility, we use the values of the limiting conductance taken from the literature[92, 93].

4.3.2 Trajectory analysis

Capture efficiency is calculated by trajectory analysis[35, 36]. Consider two particles with a radius of R and a surface potential of $\psi_{0,iso}$, which is a electrical potential on the isolated particle surface, in a simple shear flow with a shear rate of G. The relative position between the two particles can be described in the Cartesian coordinate (x, y, z) or the spherical coordinate (r, θ, ϕ). The relative velocity of the particles is determined by the following trajectory equations as described above[87].

$$\frac{dr^*}{dt^*} = r^*(1 - \mathcal{A}(r^*, \rho))\sin^2\theta \sin\phi\cos\phi + \frac{\mathcal{G}(r^*, \rho)}{6\pi\eta G R^2}(F_{vdW} + F_{edl}), \tag{4.3.15}$$

$$\frac{d\theta}{dt^*} = (1 - \mathcal{B}(r^*, \rho))\sin\theta\cos\theta\sin\phi\cos\phi, \tag{4.3.16}$$

$$\frac{d\phi}{dt^*} = \cos^2\phi - \frac{\mathcal{B}(r^*, \rho)}{2}\cos 2\phi, \tag{4.3.17}$$

where t, $r^* = r/R$, $t^* = Gt$, and ρ are time, dimensionless center-to-center distance of the particles, dimensionless time, and size ratio, respectively. $\mathcal{A}$, $\mathcal{B}$, and $\mathcal{G}$ are also hydrodynamic interaction functions that depend on ρ and r^*. In the present study, we use the expression of $\mathcal{A}$, $\mathcal{B}$, and $\mathcal{G}$ for $\rho = 1$ given by some researchers[17, 82, 86, 87, 88], because the particles have the same radius R. The more detailed expressions are explained in the previous chapter.

In Eq.(4.3.15), F_{vdW} and F_{edl} are the van der Waals attractive force and the double layer repulsive force, respectively. The van der Waals attraction including the retardation effect is calculated by the following expressions[46, 47, 89]. That is, if $p < 0.590$,

$$F_{vdW} = -\frac{A_{\mathrm{H}} R}{(1+\rho)h^2} \frac{1 + 3.54p}{6(1 + 1.77p)^2}, \tag{4.3.18}$$

and if $p \geq 0.590$,

$$F_{vdW} = -\frac{A_{\mathrm{H}} R}{(1+\rho)h^2} \left(\frac{2.45}{15p} - \frac{2.17}{30p^2} + \frac{1.18}{105p^3} \right), \tag{4.3.19}$$

where $h = r - 2R$, A_{H}, and $p = 2\pi h/\lambda_{\mathrm{L}}$ are surface separation distance between two equal size particles, the Hamaker constant, and dimensionless distance in which λ_{L} is the London wavelength and has been usually taken $\lambda_{\mathrm{L}} = 100$ nm. The value of λ_{L} is comparable to the travel distance of light during one rotation of a Bohr atom electron; $c/\nu \approx 100$ nm where c and ν are the speed of light and the frequency of rotation of a Bohr atom electron[22].

In symmetrical ($z : z$ type) electrolyte solutions such as KCl, F_{edl} can be calculated by using the Derjaguin approximation as follows[60]:

$$F_{edl} = 2\pi C_b R k_B T \int_h^\infty \left[\cosh\left(\frac{e\psi_m(L)}{k_B T} \right) - 1 \right] dL, \tag{4.3.20}$$

where $\psi_m(L)$ is the mid-plane potential between two identical plates with a plate-to-plate distance of L. If the electrolyte is symmetrical, $\psi_m(L)$ can be related to the surface charge density σ by[60]

$$\sigma = \frac{\epsilon_r \epsilon_0 \kappa k_B T}{e} \frac{\exp(2e\psi_m/(k_B T)) - 1}{\exp(e\psi_m/(2k_B T))} \frac{\mathrm{sn}(\nu|m)}{\mathrm{cn}(\nu|m)\mathrm{dn}(\nu|m)}, \tag{4.3.21}$$

where $\mathrm{sn}(\nu|m)$, $\mathrm{cn}(\nu|m)$, and $\mathrm{cd}(\nu|m)$ are the Jacobian elliptic functions of argument $\nu = \kappa L/[4\exp(e\psi_m/(2k_BT))]$ and parameter $m = \exp(2e\psi_m/(k_BT))$ as explained in the previous chapter.

The temporal change of relative position between two colliding particles can be calculated using Eqs.(4.3.15)-(4.3.17) by the forth Runge-Kutta method. The previous chapter mentions how to terminate each calculation from released points to judge whether aggregation occurs or not in a deterministic way in more detail. Then, the boundary between aggregation or not on $x - z$ plane at the released point, $x_c(z)$ and the maximum of z on the boundary, z_{max} can be evaluated with the trajectory analysis described above. With the $x_c(z)$ and z_{max}, the particle collision rate Z in Eq.(4.1.1) is calculated by integrating the particle flux passing through inner region of the boundary given by

$$\begin{aligned} Z &= 4N_0G\int_0^{z_{max}}\int_0^{x_c(z')} x'dx'dz' \\ &= 2N_0G\int_0^{z_{max}}[x_c(z')]^2dz'. \end{aligned} \tag{4.3.22}$$

From Eq.(4.1.1), Eq.(4.3.22) and the Smoluchowski collision rate Z_{smol}, the capture efficiency α is calculated as follows

$$\alpha = \frac{3}{16}\int_0^{z^*_{max}}[x^*_c(z^*)]^2dz^*, \tag{4.3.23}$$

where $z^* = z/R$, z^*_{max} and $x^*_c(z^*) = x_c/R$.

Moreover, we uses a model including the probabilistic distribution in surface charge density to examine the effect of surface charge variation on capture efficiency[21]. When two colliding particles with normal-distributed surface charge density approach to each other, the capture efficiency can be calculated on average as

$$\alpha_{ave} = \int_{-\infty}^{\infty}\int_{-\infty}^{\infty}\alpha(\sigma_1,\sigma_2)P(\sigma_1,\sigma_2)\mathrm{d}\sigma_1\mathrm{d}\sigma_2, \tag{4.3.24}$$

where σ_1 and σ_2 are the surface charge densities of each particles. The σ_1 and σ_2 are normally distributed and follow the joint probability density function $P(\sigma_1,\sigma_2)$ with

the standard deviation $\Delta\sigma$ as

$$P(\sigma_1, \sigma_2) = \frac{1}{2\pi(\Delta\sigma)^2} \exp\left[-\frac{(\sigma_1 - \sigma_0)^2}{2(\Delta\sigma)^2}\right] \times \exp\left[-\frac{(\sigma_2 - \sigma_0)^2}{2(\Delta\sigma)^2}\right], \tag{4.3.25}$$

where CV $= \Delta\sigma/\sigma_0$ is the coefficient of variance. In the case of CV $= 0$, Eq.(4.3.24) reduces to the one without the distribution in surface charge density, just the value of σ_0 is used.

4.4 Results and Discussion

4.4.1 The electrophoretic mobility

In **Figs. 4.4.1** and **4.4.2**, measured electrophoretic mobilities (open circles) are shown with theoretical ones (lines). The solid and broken lines are the theoretical calculation with the relaxation effect (Eq.(4.3.5) proposed by Ohshima) and without the relaxation (Eq.(4.3.4) proposed by Smoluchowski), respectively. Surface charge densities σ of -60 mC/m^2 for the smaller latex and -70 mC/m^2 for the larger particles were taken from the literature[41]. From **Figs. 4.4.1** and **4.4.2**, we see that the experimental values of electrophoretic mobility decrease with decreasing the KCl concentration and show a minimum value. The minimum value indicates that the re-

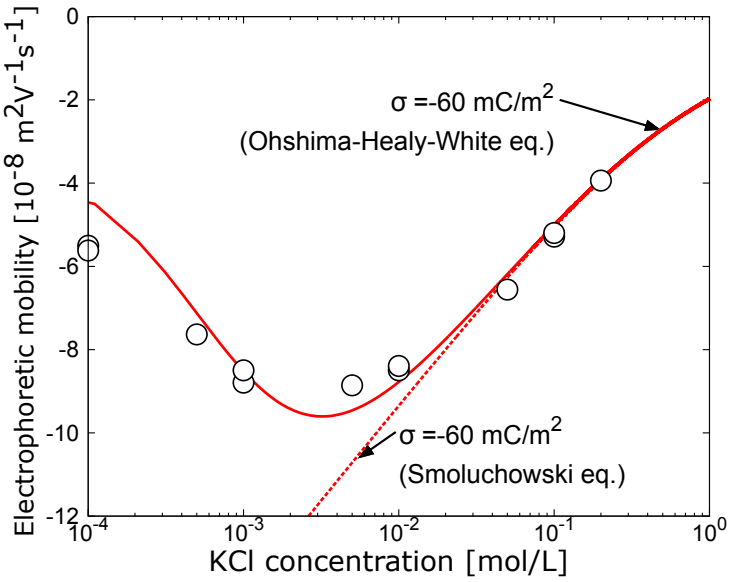

Figure 4.4.1: The relationship between electrophoretic mobility and KCl concentration for the particles with the diameter of $2R = 1.96$ μm: Open circles and lines are experimental values and theoretical values calculated by standard electrokinetic model, respectively.

laxation effect becomes significant with increasing the surface potential and with the decrease of the KCl concentration. The theoretical values including the relaxation effect agree with the experimental ones whereas the calculations without the relaxation effect significantly deviate from the experimental values at low KCl concentration. In the lowest KCl concentration, where the absolute surface potential is the highest, the Ohshima theory slightly overestimates the experimental ones. The discrepancies are not significant compared to the Smoluchowski's theory. But there is the difference between Ohshima theory and experiment. Similar differences have been observed by some other researchers at low ionic strength[11, 23]. In the case of low ionic strength and high surface potential, the relaxation effects are significant. As a result, the electrophoretic mobility shows the minimum value. While the theory including the relaxation captures the mobility minimum, differences exist between the experimental data and the theoretical values in such conditions. The discrepancy is probably caused by the incompleteness of the relaxation theory. At high surface potential and low salt concentration, the surface strongly attracts and concentrates the counter-ions near the surface. Because the theory does not include the effect of finite size of ions, the exact description of the layer structure and mobility of accumulated ion near the surface are still lacking. In any case, from the analysis, we conclude that the standard electrokinetic model and the charge densitiy are valid for both particles, in particular, in the KCl concentration

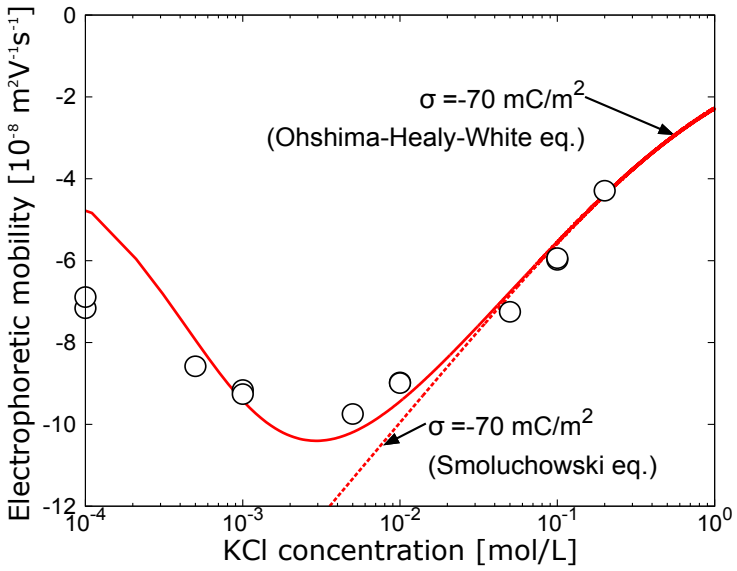

Figure 4.4.2: The relationship between electrophoretic mobility and KCl concentration for the particles with the diameter of $2R = 2.8$ μm: Open circles and lines are experimental values and theoretical values calculated by standard electrokinetic model, respectively.

larger than 10^{-3} M. Therefore, the surface charge densities used in the electrophoretic mobility are used for the trajectory analysis in the following section.

4.4.2 Capture efficiency in a shear flow

Measured and theoretical capture efficiencies for different shear rates are shown in **Fig. 4.4.3** for smaller particles ($2R = 1.96$ μm) and **Fig. 4.4.4** for larger particles ($2R = 2.8$ μm). Symbols are experimental data. Solid and dotted lines are theoretical

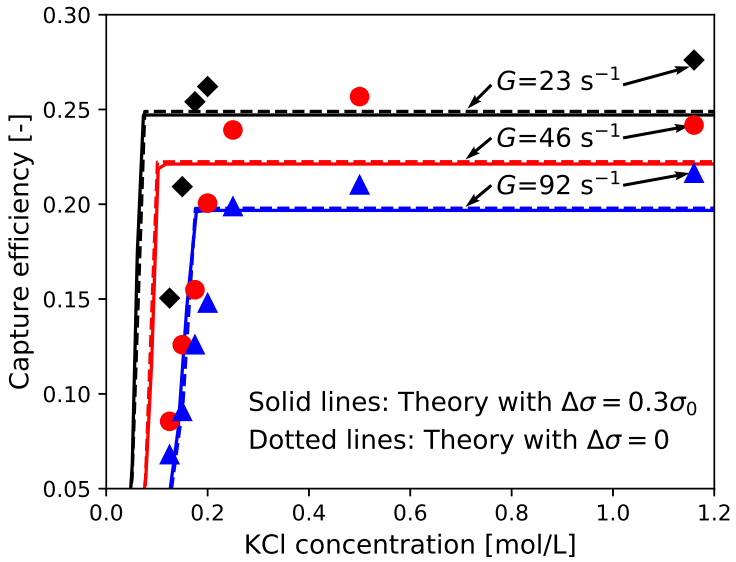

Figure 4.4.3: Capture efficiency vs. KCl concentration for the particles with the diameter of $2R = 1.96$ μm: Open circles are experimental values taken from Sato *et al.*[41]. Open circles are experimental values taken from Sato *et al.*[41]. Solid and dotted lines are theoretical values calculated by trajectory analysis using the exact PB solution with the standard deviation of $\Delta\sigma = 0.3\sigma_0$ and 0, respectively.

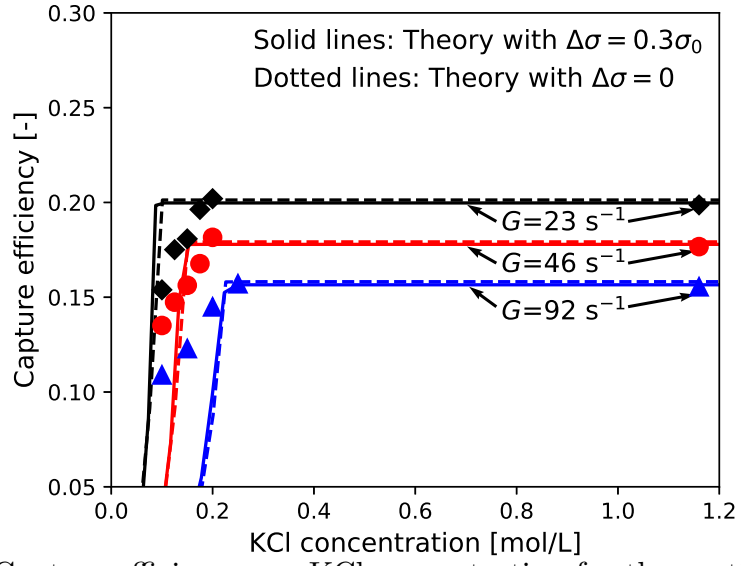

Figure 4.4.4: Capture efficiency vs. KCl concentration for the particles with the diameter of $2R = 2.8$ μm: Open circles are experimental values taken from Sato *et al.*[41]. Solid and dotted lines are theoretical values calculated by trajectory analysis using the exact PB solution with the standard deviation of $\Delta\sigma = 0.3\sigma_0$ and 0, respectively.

values calculated by trajectory analysis using non-linear Poisson-Boltzmann solution with the standard deviation of $\Delta\sigma = 0.3\sigma_0$ and 0, respectively. The theoretical values obtained by using the trajectory analysis are calculated with the Hamaker constant of $A_{\mathrm{H}} = 2.0 \times 10^{-21}$ J for both particles. This value of A_{H} for polystyrene latex particles has been confirmed to agree with the Lifshitz theory considering the effects of surface roughness and have been verified by the direct force measurement by atomic force microscope[94]. When we calculate the repulsive double layer force in this study, the surface charge density of the particles is assumed to be constant as the electrostatic boundary condition. This boundary condition is valid for the used particle surfaces bearing the strong acid groups, whose deprotonation is independent of pH and the surface separation, which means that protonation occurs to remain the surface equilibria when the surfaces approach to contact. It should be emphasized that the double layer repulsion is calculated without adjustable parameters, since the validity of the surface charge densities is confirmed by describing the experimental electrophoretic mobility with the standard electrokinetic model.

From **Figs. 4.4.3** and **4.4.4**, we find that the calculated and measured capture efficiencies decrease with decreasing the KCl concentration, demonstrating that the aggregation is impeded by the increased double layer repulsion. Furthermore, the calculated capture efficiencies qualitatively describe the experimental trend. In particular, from both figures, we find that, in both experiment and theoretical calculation, (1) CCC shifts to higher KCl concentration and (2) the dependencies of capture efficiencies on the KCl concentration slightly become more gradual as the shear rate increases. In addition, more gradual slope in the relationship between capture efficiency and KCl concentration below CCC is observed for the larger particle. This trend is also reproduced by the trajectory analysis. The agreement between theory and experiment in the trends of capture efficiency found in this study provides an evidence of the usefulness of the trajectory analysis for the study of shear-induced aggregation. However, the calculated values of CCC do not perfectly agree with experimental ones as shown in **Fig. 4.4.5**. Moreover, in the slow aggregation regime below CCC, the capture efficiencies are not in quantitative agreement with the experimental ones. Also, theoretical capture efficiencies in the absence of double layer force in **Fig. 4.4.3** are slightly lower

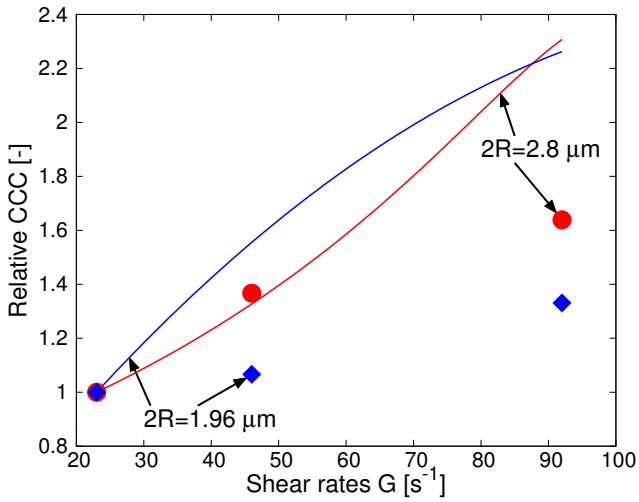

Figure 4.4.5: Critical Coagulation Concentration (CCC) vs. Shear rate G for the particles with the diameter of $2R = 1.96$ μm and $2R = 2.8$ μm: Symbols and solid lines are experimental values taken from Sato *et al.*[41] and theoretical values calculated by trajectory analysis with the exact PB solution, respectively.

than the experimental values. These discrepancies might be caused by Brownian diffusional effects and the additional non-DLVO forces such as hydration force, and charge heterogeneity[22, 23]. However, even though the effect of charge heterogeneity on α could be partially included in the calculation by considering the distributed charge density, the differences between the theories with $\Delta\sigma = 0.3\sigma_0$ and 0 are insignificant. This suggest that the effect of charge heterogeneity might not be significant in this case. Therefore, we guess that including coupled effects of Brownian motion on capture efficiency could be a next step to discuss the origin of these discrepancies.

4.5 Conclusion

We analyzed capture efficiency of a negatively charged sulfate latex particles as a function of KCl concentration and shear rate on the basis of the trajectory analysis for the first time. In the calculation of the double layer repulsion with the non-linear Poisson-Boltzmann equation, the constant charge (CC) boundary condition was used. This is because it is valid for the latex particles bearing strong acid (sulfate) groups whose charges are independent of pH. The validity of surface charge densities as an input value to calculate the repulsive force was confirmed by the electrophoretic measurements with the analysis by the standard electrokinetic model. Calculated capture

efficiencies were in reasonable agreement with experimental values taken from the previous study[41]. Our finding suggests that the trajectory analysis is valuable for the study on the aggregation in flow fields. However, the quantitative differences between measured and calculated capture efficiencies were observed in the presence of the double layer repulsion even with the use of the exact Poisson-Boltzmann solution. The difference might be caused by additional non-DLVO forces[23, 22], and Brownian fluctuation which are not included in the present analysis. Moreover, whereas the constant charge model is assumed in this study, the charge regulation could be significant when they approach in short distances because the proton concentration on their surface could be increased due to the high surface potential when approaching with each other. This might even cause the protonation of their sulfate group to regulate their surface charges and reduce the electrical repulsion between them. Therefore, one could try the other electrical boundary condition such as charge regulation model.

Chapter 5

Effect of hydrophobic monovalent ions on charge reversal of model colloids

5.1 Introduction

In the previous Chapter 4, we have analyzed the effect of ionic strength and shear rate on aggregation rates in a simple shear flow for the sulfate latex particles with constant charges quantified by the electrophoretic measurements and its analysis. We do not consider ion adsorption onto the colloid surfaces in the previous chapter. However, the ion adsorption often happens in environments because there can be strongly-adsorbed ions such as multivalent counter-ions and hydrophobic organic ions. Such counter-ion adsorption compensates the surface charge amounts on the colloids and subsequently affects the aggregation behavior of colloids. Therefore, in this Chapter 5, we investigate the charging behavior of colloidal particles in the presence of hydrophobic ions.

Again, the stability of colloidal dispersion against aggregation-sedimentation is one of the important issues for scientific interest and industrial and technological applications such as foods storage, inks, paints, water treatment, and colloid-facilitated transport[1, 2]. The stability of colloids can be commonly explained by the Derjaguin, Landau, Verwey, and Overbeek (DLVO) theory[4, 5] in which interparticle interactions

are composed of the van der Waals attraction and electrical double layer force. Particularly, the electrical double layer force is regulated by the charging behavior of colloidal particles. Therefore, one needs to estimate the surface charge of colloidal particles to predict their stability.

The surface charging properties of colloidal particles are strongly affected by the adsorption of oppositely-charging species such as polyelectrolytes[27, 28], surfactants[30, 31], and multivalent ions[24, 25, 43] onto the surfaces. Such adsorption can induce so-called charge reversal/overcharging which causes the change in sign of the net surface charges due to the excess accumulation of counter ionic species[32]. To reveal the mechanism of charge reversal, many studies have been done with the approaches of Monte-Carlo simulation and molecular dynamics including inter-ion correlation[95, 33], ionic specificity[96], and hydrophobic interaction[97]. The previous studies have demonstrated that the hydrophobicity of ions and colloids can significantly influence the surface/electrokinetic charge density in the presence of large hydrophobic ions[97, 34, 98, 29]. Notably, the previous research with molecular dynamics simulation[97] has confirmed the linear relationship between the isoelectric point (IEP), which is the concentration where the charge reversal occurs, and the surface charge density by assuming a constant adsorption free energy of ions[34, 99]. Nevertheless, the intrinsic energy of adsorption for hydrophobic tetraphenylphosphonium (TPP^+) ions onto polystyrene sulfate latex surfaces decreases with increasing the surface charge density[29] even though the hydrophobic ion concentration at the IEP increases with the increase of the charge density as shown in the previous studies[97, 34]. This finding suggests that the intrinsic adsorption energy of hydrophobic ions can be a function of surface charge density. However, the effect of charge density on the intrinsic energy of adsorption of hydrophobic ions remains ambiguous because the previous work used sulfate latex particles with different charge densities and sizes[29].

In the present study, to clarify the effect of surface charges on the adsorption of hydrophobic ions, which induces the reverse of sign in the surface (or zeta) potential, we measured and analyzed the electrophoretic mobilities of carboxylate polystyrene latex particles in the presence of hydrophobic tetraphenylphosphonium (TPP^+) ions. Carboxyl latex particles have carboxyl groups on their surface, and thus the negative

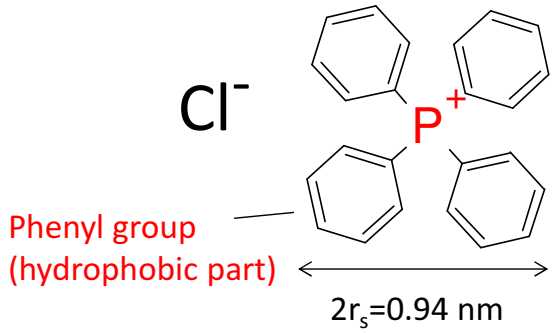

Figure 5.2.1: Structural formula of tetraphenylphosphonium chloride TPPCl

surface charge density increases with pH due to their deprotonation. This feature of carboxylated latex particles enables us to examine the effect of charge density and hydrophobic interaction on the adsorption of TPP^+ ions onto the surfaces without changing the size of particles.

5.2 Experiments

5.2.1 Materials

Carboxylated polystyrene latex particles (Molecular Probes) were employed as model colloidal particles. The used carboxyl latex particles have pH-dependent negative charges due to the deprotonation of the carboxyl groups on the particle surface. The manufacturer reports that the chargeable site density on the surface Γ_{tot} is 1.136 nm^{-2}, the diameter $2a$ is 1.5 ± 0.03 μm, and the density is 1.055 g/cm^3, respectively. KCl (JIS special grade, Wako Pure Chemical Industries) and tetraphenylphosphonium chloride TPPCl (EP grade, Tokyo Chemical Industry Co.) were used to prepare the electrolyte solutions. The structural formula of TPPCl is shown in **Fig. 5.2.1**. The pH was adjusted by the addition of HCl (JIS special grade, Wako Pure Chemical Industries) and KOH solutions. Carbonate free KOH solution was prepared by following the method described in the literature[100]. Before the sample preparation, all solutions were filtered with a 0.20 μm pore filter (DISMIC 25HP, ADVANTEC). All solutions and suspensions were prepared from deionized water (Elix, MILLIPORE) and degassed before use.

5.2.2 Electrophoretic measurements

Electrophoretic mobility (EPM) was measured by electrophoretic light scattering technique with Zetasizer NANO-ZS (Malvern). Measurements were carried out as a function of solution pH at different mixed molar ratio X=[TPP^+]/[K^+] with fixed ionic strength, where [TPP^+] and [K^+] denote the concentrations of TPP^+ and K^+. The pH was adjusted in the range from 3 to 11 with HCl and KOH solutions. Ionic strengths were 10 mM and 50 mM, and the mixed molar ratios X were 0, 0.01, 0.1, 0.5, 5 and ∞. The particle concentration was set to 50 mg/L in all experiments. The samples were prepared by mixing the required volumes of the suspension of the carboxyl latex particles, KCl solution, TPPCl solution, pH adjuster, and degassed water. The pH was measured with a combination electrode (ELP-035, TOA-DKK). All the experiments were carried out at 20 ℃.

5.3 Modeling

5.3.1 Charging model

The surface charge of the used particle arises from the deprotonation of carboxyl group. That is,

$$-\mathrm{COOH} \rightleftharpoons -\mathrm{COO}^- + \mathrm{H}^+. \tag{5.3.1}$$

The dissociation equilibrium between the carboxyl groups and the proton in the electrolyte solution is characterized by the proton dissociation constant defined as[23]

$$\mathrm{p}K_\mathrm{H} = -\log_{10} K_\mathrm{H} = -\log_{10} \frac{\Gamma_{-\mathrm{COO}^-} a^s_{\mathrm{H}^+}}{\Gamma_{-\mathrm{COOH}}}, \tag{5.3.2}$$

where $\Gamma_{-\mathrm{COO}^-}$, $\Gamma_{-\mathrm{COOH}}$, and $a^s_{\mathrm{H}^+}$ are the surface activities of dissociated and protonated carboxyl groups, and proton, respectively. K_H is the acid dissociation constant. The value of $\mathrm{p}K_\mathrm{H}$ used in this study is 4.9 from the literature[23]. The surface activity of proton is related to the bulk activity $a^b_{\mathrm{H}^+}$ and the surface potential ψ_0 via the

Boltzmann equation

$$a^s_{\mathrm{H^+}} = a^b_{\mathrm{H^+}} \exp\left(-\frac{e\psi_0}{k_B T}\right), \tag{5.3.3}$$

where e is the elementary charge, k_B is the Boltzmann constant, T is the absolute temperature. Since the surface charge density is attributed to the dissociated carboxyl groups on the surface, the relationship between the surface charge density and the surface potential due to deprotonation can be described as

$$\sigma_0 = -e\Gamma_{-\mathrm{COO^-}} = -\frac{e\Gamma_{tot}}{1 + 10^{\mathrm{p}K_{\mathrm{H}} - \mathrm{pH}} \exp\left(-\frac{e\psi_0}{k_B T}\right)}, \tag{5.3.4}$$

where Γ_{tot} is the total site density of surface carboxyl groups including dissociated and protonated ones.

The TPP^+ ions strongly adsorb onto the surfaces of the polystyrene latex particles which are hydrophobic. To describe the adsorption of the TPP^+ ions, we introduce the Stern layer model with the following equation[30, 34]:

$$\Gamma_s = 2r_s C_{\mathrm{TPP}} \left(-\frac{-\phi + e\psi_d}{k_B T}\right), \tag{5.3.5}$$

where the Γ_s is the amount of adsorbed TPP^+ ions in the Stern layer, r_s is the radius of adsorbed TPP^+ ion with the value of $2r_s = 0.94$ nm[34] used in present study, C_{TPP} is the bulk concentration of TPPCl, ψ_d is the diffuse layer potential, ϕ is the non-electrostatic chemical/intrinsic adsorption energy per ion. The term of chemical/intrinsic adsorption energy represents the energies other than from electrostatic origin. To incorporate the dependency of the non-electrostatic adsorption energy on the surface charge density proposed by the previous work[29], we have introduced the following simple linear interpolation to calculate the value of ϕ as

$$\phi = (\phi_{min} - \phi_{max})\frac{\sigma_0}{-e\Gamma_{tot}} + \phi_{max}, \tag{5.3.6}$$

where ϕ_{min} and ϕ_{max} are the minimum and the maximum non-electrostatic chemical/intrinsic adsorption energy per ion. These values are determined below in Section 4.

With Eq. (5.3.5), we can express the Stern layer charge density σ_s as

$$\sigma_s = eN_A\Gamma_s, \tag{5.3.7}$$

where N_A is the Avogadro number. This equation suggests that the adsorbed amount of TPP^+ ions in the Stern layer is in charge of the development of the Stern layer charge density σ_s.

The relationship between the diffuse layer charge density σ_d and the diffuse layer potential ψ_d for our system is given by the Grahame equation for monovalent salt as follows[21]:

$$\sigma_d = -\frac{2\epsilon_r\epsilon_0\kappa k_B T}{e}\sinh\left(\frac{e\psi_d}{2k_B T}\right), \tag{5.3.8}$$

with the Debye length κ^{-1} as

$$\kappa^{-1} = \left(\frac{\epsilon_r\epsilon_0 k_B T}{2(C_{\mathrm{KCl}} + C_{\mathrm{TPPCl}})N_A e^2}\right)^{\frac{1}{2}}, \tag{5.3.9}$$

where C_{KCl} and C_{TPPCl} are the concentrations of KCl and TPPCl, and ϵ_0 is the dielectric constant of vacuum, $\epsilon_r = 80.4$ is the relative dielectric constant of water. For the surface bearing weak-acidic groups with the Stern layer, one needs to assume the following linear relationship[21]

$$\sigma_0 = C_s(\psi_0 - \psi_d), \tag{5.3.10}$$

where C_s is the Stern layer capacitance. We set the value to $C_s = \epsilon_r\epsilon_0/r_s$ by assuming the thickness of the Stern layer is the radius of TPP^+ ion r_s.

According to the principle of electroneutrality, the sum of surface σ_0, the Stern layer σ_s, and diffuse layer charge densities σ_d must be zero. It requires the condition below:

$$\sigma_0 + \sigma_s + \sigma_d = 0. \tag{5.3.11}$$

The set of Eqs. (5.3.2-5.3.11) is solved numerically to obtain the diffuse layer potential ψ_d for the successive calculation of the zeta potential ζ. Particularly, in a pure KCl solution, the above set of equation is solved with the conditions $\psi_d = \psi_0$, $\sigma_s = 0$, and

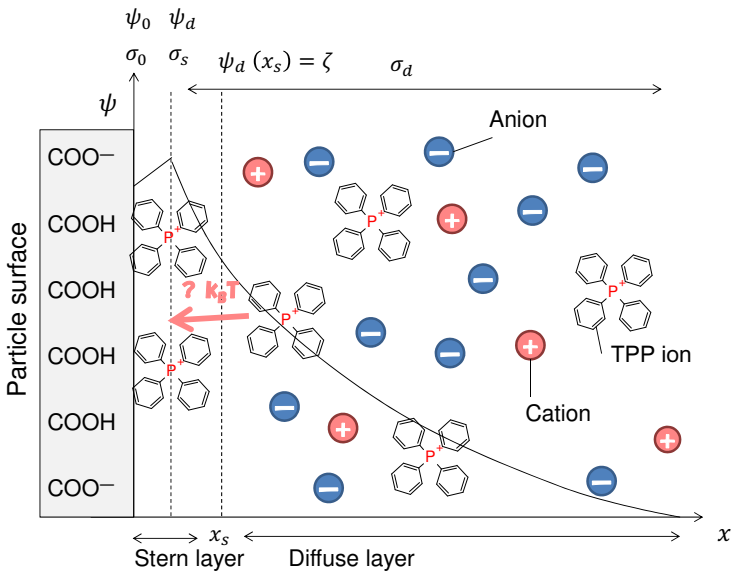

Figure 5.3.1: Graphical representation of 1-pK_{H} Stern-Gouy-Chapman model with TPP^+ adsorption

$C_s \to \infty$ meaning no Stern layer for pure KCl case.

To calculate the electrophoretic mobility in the following section, the zeta potential ζ from ψ_d, which is set to $\psi_d = \psi_0$ for pure KCl solution, is calculated with the Gouy-Chapman theory via

$$\zeta = \psi(x_s) = \frac{4k_BT}{e} \tanh^{-1}\left[\tanh\left(\frac{e\psi_d}{4k_BT}\exp(-\kappa x_s)\right)\right], \tag{5.3.12}$$

where x_s is the distance to the slipping plane. The value of x_s for pure KCl case is set to x_s=0.25 nm[23], while the value for mixed KCl and TPPCl case is set to $x_s = r_s$=0.47 nm with the assumption that the extent of the slipping plane coincides with the outer edge of the adsorbed TPP^+ ion on the surface.

5.3.2 Electrophoretic mobility (EPM)

The electrophoretic mobilities (EPMs) are calculated from the zeta potential using the Ohshima equation including the relaxation effect[75] and the Smoluchowski equation neglecting the relaxation effect. We have calculated the electrophoretic mobilities with the same equation used in Section 3, Eq. (4.3.5). In this chapter, the values of the limiting molar conductance of each ions employed 66.17 for K^+, 20.7 for TPP^+, and 68.68 for Cl^- which are taken from the literature[93, 101].

5.4 Results and Discussion

We plot the EPMs of carboxyl latex particles as a function of the solution pH at different ionic strengths in **Fig. 5.4.1** (a,b) for 10 mM and **Fig. 5.4.1** (c,d) for 50 mM, respectively. In **Fig. 5.4.1**, the symbols are experimental values, the solid lines are the theoretical values calculated by the Ohshima equation including the relaxation effect, and the dashed lines are the theoretical values calculated by the Smoluchowski equation neglecting the relaxation effect. While the lines in **Fig. 5.4.1** (a,c) are drawn with the constant non-electrostatic intrinsic energy of TPP^+ adsorption of $\phi = 6\ k_BT$, the lines in **Fig. 5.4.1** (b,d) are obtained with the assumption that the energy for TPP^+ adsorption linearly varies with the surface charge density from 6 k_BT to 4 k_BT. The value of 6 k_BT is taken from the literature[34]. They also reported that the free energy of transfer for a phenyl group from water to organic solvents is approximately 3 k_BT and it is closely related to the adsorption energy. It should be noted that the value of 6 k_BT corresponds to the situation where two of four phenyl groups on TPP^+ ions adsorb onto hydrophobic polystyrene latex surfaces[34]. These values used in the literature are comparable with the values we used.

In the case of pure KCl solution, X=[TPP^+]/[K^+]=0, the electrophoretic mobility in magnitude increases with pH. It shows that the particles are highly negatively charged at high pH due to the deprotonation of carboxyl groups. The experimental electrophoretic mobilities in the solution including TPP^+ in **Fig. 5.4.1** show positive values at low pH, indicating that the occurrence of charge inversion. This inversion is attributed to the adsorption of TPP^+ on the surfaces by hydrophobic interaction between phenyl groups of TPP^+ ions and the polystyrene surface. With increasing pH, the positive electrophoretic mobilities decrease. Then, the electrophoretic mobilities reverse again to negative values. This charge re-reversal means that the increased number of deprotonated carboxyl groups at high pH outnumbers the adsorbed amount of TPP^+ ions. In addition, the charge re-reversal pHs shift to higher pH with increasing the mixed molar ratio X and the ionic strength. This is because larger amounts of deprotonated carboxyl groups are required to compensate more adsorbed TPP^+ ions associated with abundant TPP^+ ions in bulk solution. However, the experimental

electrophoretic mobilities at 50 mM and mixed molar ratios higher than X=5 in **Fig. 5.4.1** (c,d) are positive and do not show the charge re-reversal regardless of pH. This can be ascribed to the existence of excess amounts of adsorbed TPP^+ ions even though all carboxyl groups are deprotonated at high pH.

From the comparison of calculated values with two different models, Smoluchowski equation and Ohshima equation, we confirm that differences in calculated electrophoretic mobilities between these two methods are not so significant for our case. This can be rationalized by relatively low zeta potentials which are induced by the charge reversal, and thus the relaxation effect is not significant.

In the comparison with theoretical values calculated by assuming the constant non-electrostatic intrinsic energy of adsorption in **Fig. 5.4.1** (a,c), one finds that the calculations capture the experimental trends. However, the calculations with the constant adsorption energy overestimates the adsorption amount of TPP^+ ions and cannot describe the experimentally observed charge re-reversal of electrophoretic mobilities at high pH with higher mixed molar ratios. In contrast, the calculated mobilities obtained by assuming that the intrinsic energy of adsorption in **Fig. 5.4.1** (b,d) is proportional to the surface charge density can successfully reproduce the charge re-reversal for all the conditions and even in high mixed molar ratios. Therefore, our result suggests that the intrinsic energy of adsorption of TPP^+ decreases from 6 k_BT to 4 k_BT with increasing charge density. This finding is consistent with the result that the intrinsic energy of TPP^+ adsorption decreases with increasing the surface charge density of sulfate latex particles with different diameters[29], and complements their finding by monodisperse carboxylated latex particles with pH-variable surface charge.

Moreover, on the basis of our results above, we suggest the reason why the intrinsic energy of adsorption for TPP^+ ions can be dependent on the surface charge density as follows. As the deprotonation of surface carboxyl groups progresses with increasing pH, the particle surfaces become less hydrophobic. Such relatively low hydrophobicity can make difficult TPP^+ ions to be accumulated near the surfaces. Therefore, the adsorption energy decreases with the surface charge density, in other word, the number of dissociated surface groups. Hence, such reduction in the adsorption energy might cause the charge re-reversed electrophoretic mobilities from positive to negative due to

the deprotonation of carboxyl groups. This suggestion also can rationalize the result of the previous study[29] because high surface charge densities of the sulfate latex particles mean larger number of surface sulfate groups on their surfaces.

Even though the proposed simple modeling captures the experimental trends represented by the charge re-reversal, there are still quantitative discrepancies in intermediate mixed molar ratios, for instance, X=0.01 and 0.1 at 10 and 50 mM. This could suggest us that the adsorption behavior in mixed solution of KCl and TPPCl

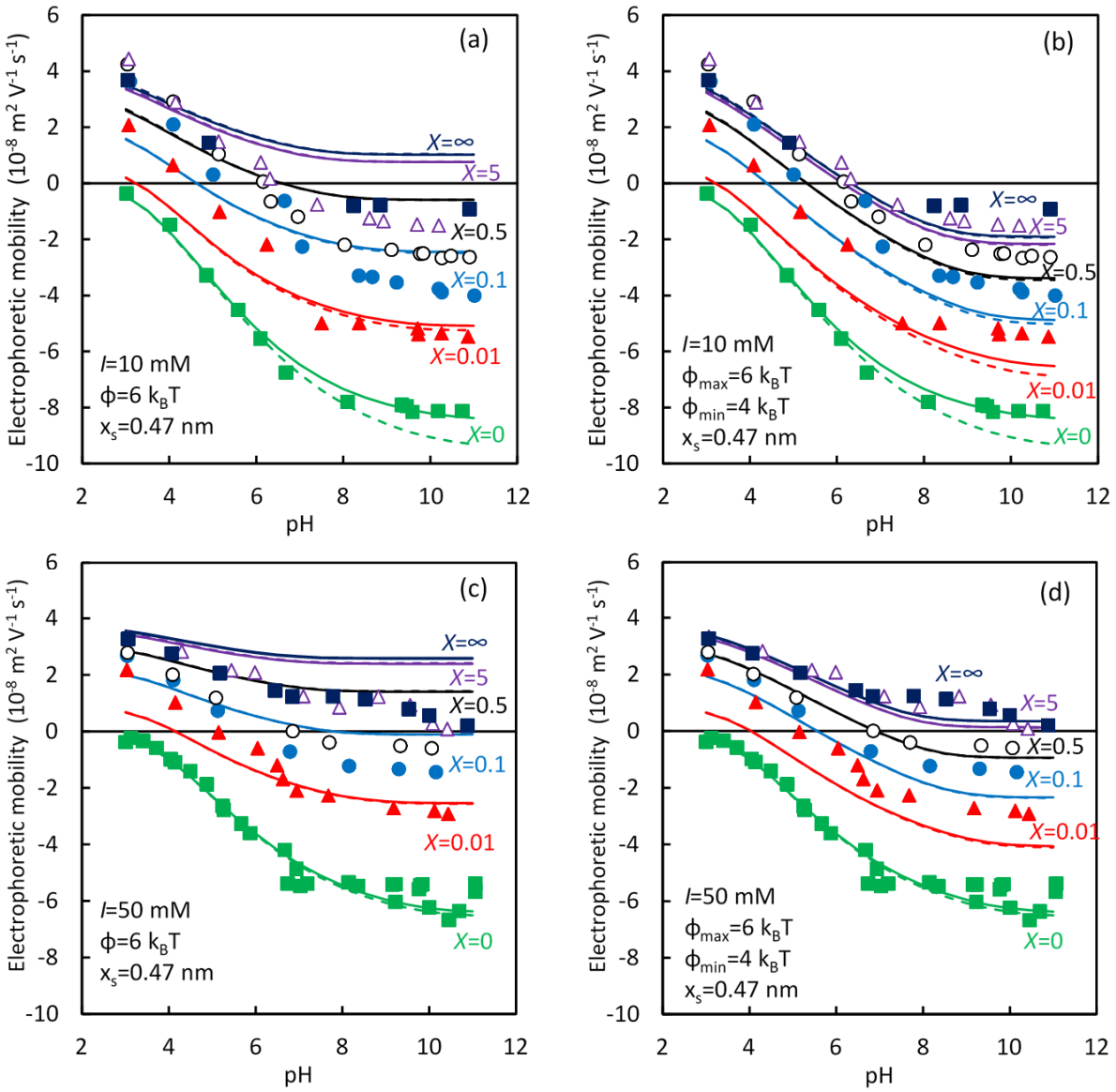

Figure 5.4.1: The relationship between electrophoretic mobility of carboxyl latex particles and pH in mixed solution of KCl and TPPCl at 10 mM for (a,b) and 50 mM for (c,d). Symbols are experimental values. Solid and dashed lines are theoretical values calculated by the Ohshima equation and the Smoluchowski equation, respectively. Mixed molar ratios X=[TPP^+]/[K^+] are 0, 0.01, 0.1, 0.5, 5 and ∞ from lower to upper lines. Calculated values in (a,c) are obtained by assuming the constant non-electrostatic intrinsic energy of TPP^+ adsorption and theoretical values in (b,d) are calculated by assuming pH-dependent intrinsic energy of TPP^+ adsorption.

can be more complex than the simple model used in this chapter. The discrepancies in solution containing K^+ ions at higher pH could be explained by K^+ binding to the deprotonated carboxylic groups[102] by decreasing the amounts of surface charge, which decreases the magnitude of mobilities. However, such explanation is not applicable at lower pH because of less deprotonated groups. So, the discrepancies at lower pH within our simple modeling seem to be attributed to mixed effects due to mutual interaction between K^+ and TPP^+ ions. Since TPP^+ ions have larger hydrophobicity, in other words, higher affinity to the hydrophobic latex surfaces than K^+ ions, TPP^+ ions tend to accumulate near the surface than K^+ ions. In addition, K^+ ions experience electrical repulsion with TPP^+ ions and less attraction with the surface due to its lower surface charge density at low pH. These interactions between the surface and ions might cause the depletion of K^+ ions between the surface and TPP^+ ions, which can augment the TPP^+ adsorption by depletion forces. Related specific ionic effects have been examined in the previous work[96], however, mixed effects of ions with different surface affinity on the adsorption are still under consideration. Molecular dynamics and Monte Carlo simulation would help to clarify this enhanced adsorption in mixed solution.

Another possible effect, which can apparently reduce the adsorption energy in our modeling, is to consider ionic steric effect due to ionic saturation and finite size effects in adsorption process. Along with an approximated mean field model for the steric effect discussed in the previous research[34], an estimate for the excess chemical potential of TPP^+ at the Stern layer is given by $\mu_{ex} \approx k_B T \ln(1 + C_s v)$, where $C_s = \Gamma_s/(2r_s)$ calculated from Eq. (5.3.5) is the TPP^+ concentration at the Stern layer, and $v \approx 200$ cm^3/mol is the volume of the cation approximated as the value for $TPAs^+$ (tetraphenyl arsonium ion)[103]. In 50 mM solution of pure TPPCl with constant adsorption energy of $\phi = 6\ k_B T$, one estimates $C_s \approx 2.38$ M, and leads a repulsive free energy with $\mu_{ex} \approx 0.39 k_B T$. This value is still smaller than the reduction of adsorption energy of $|\phi_{max} - \phi_{min}| = 2k_B T$, suggesting that the steric effect is not dominant in the TPP^+ adsorption. Therefore, our interpretation can be valid in the solution where TPPCl is dominant, although we need more sophisticated theoretical treatment for the reduction of adsorption energy in the future.

5.5 Conclusion

Electrophoretic mobilities of carboxyl latex particles were measured in mixed solutions of KCl and TPPCl as a function of the pH, the ionic strength, and the mixed molar ratio of X=[TPP^+]/[K^+] to reveal the effect of hydrophobicity on the charge reversal. We observed that the charge reversal of the latex occurred at low pH in the presence of hydrophobic TPP^+ ions because of hydrophobic interaction. With increasing pH, the EPMs were reversed again due to the increased deprotonation of carboxylic groups and the reduction of hydrophobic interaction. With the theoretical analysis describing such charge re-reversal, we found the reduction in the intrinsic energy of adsorption of TPP^+ with increasing the charge density from $6k_BT$ at the lowest charge density to $4k_BT$ at the highest charge density. This finding supports the conclusion in the previous work[29] and suggests that the non-electrostatic energy of adsorption of TPP^+ is dependent on the surface charge density of adsorbents.

Chapter 6

Effect of anionic species on Brownian homo/hetero-aggregation of oppositely-charged particles

6.1 Introduction

In the previous chapter 5, we have shown that even hydrophobic monovalent counter ions can induce a charge reversal due to the specific adsorption onto the charged surfaces. Such charge reversal can substantially influence the aggregation stability of colloidal particles by varying the electrostatic interactions between them[104].

Generally, the stability of colloidal suspensions can be strongly affected by the presence of multivalent counter-ions, as already noted by Schulze[105] and Hardy[106]. Colloidal suspensions are destabilized by forming aggregates of colloidal particles, whereby the early stage of aggregation is governed by the formation of particle doublets. Again, Derjaguin, Landau, Verwey, and Overbeek (DLVO)[4, 5] have shown that the formation of particle doublets is classified to the following two regions, so-called fast and slow aggregation. The fast aggregation process is controlled by the particle pairs colliding

by Brownian or fluid motion, and interacting mainly via the van der Waals attraction. Usually, this process occurs at high salt concentrations where the electrostatic repulsion between particles is screened. The slow aggregation process is rate-limited to overcome an energy barrier due to the electrical repulsion, and it is enhanced in low salt concentrations. The transition between these two regions is observed at a rather certain concentration, called as the critical coagulation concentration (CCC). The Schulze-Hardy rule states that the CCC strongly decreases with increasing the valence of counter-ions[107, 2]. These trends have been affirmed by systematic experiments in different types of aqueous particle suspensions in the presence of multivalent counter-ions[108, 109, 110, 111, 112, 113, 26].

Time-resolved light scattering techniques have verified to be much useful not only for aggregation studies on ionic valence effects[23, 114], but also for ones on ion specific effects[44, 45]. Despite of the same ionic valence in solutions, each counter-ions can have different affinities to a surface, which may induce the strong adsorption of ions on oppositely charged particles and destabilize the particles. In addition, such adsorption also causes a charge reversal of the particles as seen in the previous chapter 5. As a result, the particles are re-stabilized at intermediate salt concentrations[45]. The DLVO theory can be used to interpret such phenomena with the aid of the complemented measurements for their charging behaviors such as zeta potentials. Again, within the DLVO theory, the interaction force is modeled by a superposition of van der Waals and double layer forces. Even though we might not always apply these interpretations, we believe that a reasonably good understanding of the stability of aqueous colloidal suspensions has been attained nowadays.

However, this understanding solely holds for homo-aggregation, meaning that aggregates are being formed out of identical particles. Hetero-aggregation, meaning that aggregates are being formed out of different particles, is much less understood. The most particular reason for this situation is that measuring hetero-aggregation rates is more difficult than for homo-aggregation. The typical drawback is that in a binary mixture of colloidal particles, the hetero-aggregation can happen simultaneously with two different types of homo-aggregation, and these three processes are required to separate suitably in order to extract the hetero-aggregation rate. One can overcome this difficulty by

performing experiments with two types of particles which have different signs of their surface charge, but with the equal size and bulk composition. To study such system, one may use any of the existing methods to investigate homo-aggregation, and measure the apparent aggregation rate, typically increased rates of hydrodynamic radius of the system, as a function of the mixing ratio of the two types of particles. In the early stage of aggregation, the hetero-aggregation rate can be evaluated from the dependence of the apparent aggregation rate on the ratio of particle concentrations[115, 116]. While such experiments can be easily analyzed, this technique is extremely cumbersome, and limits the options of particles to be studied. Despite these restrictions, a similar method was also used to investigate the heteroaggregation of particles with widely different shapes and sizes[117, 118]. While these measurements could provide useful conclusions too, the analysis remains qualitative.

Recently, some researchers have proposed an alternative technique, which can be utilized to study hetero-aggregation in any kind of binary mixtures of differently sized colloidal particles[42]. This technique is based on time-resolved simultaneous multi-angle light scattering, and exploits the specific angular dependence of the form factors of the different doublets to distinguish the contributions from hetero-aggregation and homo-aggregation. While this technique offers wider options of particles, its disadvantage is that the analysis of experimental data is more complex, and requires the form factors of the asymmetric dimers. However, for spherical and mono-disperse particles, these form factors can be accurately and numerically calculated using the T-matrix method[119, 120].

Despite these complexities, hetero-aggregation processes were tackled by these techniques. An important finding was that the hetero-aggregation rate between oppositely charged particles is comparable to the ones for homo-aggregation at high salt levels, but becomes faster with decreasing the salt concentration[42, 48, 121]. This trend can be rationalized by the augmented attractive electrical double layer forces acting between oppositely charged particles in low salt concentrations. A similar tendency could be also observed for the deposition kinetics of colloidal particles onto oppositely charged collector beads[122, 123]. Another important finding was made by examining the dependence of the hetero-aggregation rate between two types of oxide particles or amphoteric

polystyrene latex particles with two different isoelectric points upon pH. This rate becomes the fastest when the pH is between the two isoelectric points, where they are oppositely charged, but is quickly diminished below and above these points[124, 115]. These findings confirm the importance of electrical double layer forces in these processes. However, they reported the apparent stability ratio of binary colloidal suspensions, and extracting the hetero-aggregation rate was not attempted. However, more recently, to quantify the hetero-aggregation more accurately, the previous work has measured the hetero-aggregation rates of oppositely-charged particles in the presence of multivalent ions[43] by utilizing the multi-angle light scattering with T-matrix method. They have reported the novel pattern of the hetero-aggregation with charge reversal, which shows more repulsive behaviors in intermediate concentrations due to stronger electrostatic repulsion between the charge-reversed particles and highly-charged ones than the repulsions between the charge-reversed ones. This repulsive behavior of hetero-aggregation for asymmetrically charged particles has been supported by the DLVO theory[66], and they also pointed out that the importance of electrical boundary conditions such as constant potential and constant charge ones on the hetero-aggregation process around the isoelectric point for the charge-reversed particles[66, 43].

Anionic specific effects on hetero-aggregation processes however have not been investigated so far. For this reason, in the present work, we study binary suspensions of amidine and sulfate latex particles with different types of anions with same valency. These particles are oppositely charged in the presence of indifferent monovalent salts such as KCl. However, when ions specifically adsorb to the oppositely-charged surfaces, the charge of one particle type becomes neutralized and even reversed, while the other particle type remains highly charged. Experimental studies in such situations have not been performed yet, and the present study reports the measurements of anionic effects on hetero-aggregation rates for the first time.

6.2 Conclusion

In this study, we have measured both Brownian homo- and hetero-aggregation rates and corresponding stability ratios for positively- and negatively-charged particles in the presence of different anionic species of monovalent and divalent electrolytes. These

experimental results of the stability ratios are analyzed by using the classical DLVO theory with the corresponding zeta potentials for each particles in the different types of electrolyte solutions. The calculations are in reasonably good agreements with the experimental data.

Especially, with the cases where the positively-charged particles reverse its charge due to the adsorption of anionic species and the sign of charge of the negatively-charged particles are not changed, we have found that the hetero-aggregation with charge reversal can be more repulsive than the one for homo-aggregation of the positively-charged particles experiencing charge reversal in the range of intermediate salt concentrations, which is induced by the anionic specificity on the positively-charged particles. This experimental trends indicate that the electrostatic interactions between the two types of particles are more repulsive than the ones between the positively-charged particles with less charge amounts due to its charge reversal causing a weaker repulsion. The negatively-charged sulfate latex particles are more highly-charged developing a stronger repulsion with the charge reversed amidine latex particles.

For the monovalent phosphate anion case, the hetero-aggregation between the oppositely-charged particles shows the stability ratio higher than one below the isoelectric point of the amidine latex particles. This might suggest that the surface potential for the amidine latex are reversed when the highly-charged sulfate latex approaches as for the case of the constant charge model, and might be attributed to its strong affinity of phosphate ions to the amidine surface and less repulsion with the sulfate latex.

In addition, although the amidine latex particles are reversed its charge in the divalent SeO_4^{2-} solution, its homo-aggregation above the isoelectric point does not show the increased stability ratio due to less electrostatic repulsion in higher ionic strengths. While the hetero-aggregation between the amidine and sulfate latex are impeded by the stronger repulsion between them, again due to the highly-charged sulfate latex particles. Notably, these experimental values can be reasonably described by the classical DLVO theory with proper boundary conditions.

Chapter 7

Analysis on aggregation of unequal-sized particles in a mixing flow

7.1 Introduction

In the previous chapter 6, we have shown the importance of anion species on both Brownian homo- and hetero-aggregation rates with charge reversal. The validity of the DLVO theory to explain the more repulsive behaviors of the hetero-aggregation is demonstrated. More generally, however, the hetero-aggregation can happen not only in quiescent condition, but also in sheared flow such as mixing flow. So, we have to consider how hetero-aggregation proceeds in shear.

Some researchers have tackled questions to understand the shear hetero-aggregation. Adler calculated the capture efficiency of hetero-aggregation for unequal-sized particles in a simple shear flow with different size ratios of smaller and larger particle radii by the trajectory analysis described above[125]. He has reported that the capture efficiency in a simple shear flow considerably decreases with decreasing size ratio even in the absence of electrostatic repulsion. Such decrease of the capture efficiency can be rationalized to consider the opened and closed trajectories around the large particle. First, within the trajectory analysis neglecting Brownian motion, the colliding particles can

form aggregates if their relative trajectory between the reference and another particles approaches and attaches to the reference particle due to the van der Waals attraction. The opened trajectory is the relative trajectory approaching from far away towards the reference particle and flowing out to infinity in the absence of attractive forces. The closed trajectory is the ones going out from and back to the reference particle, which does not contribute to the net particle flux towards the reference particle. These three types of trajectory can not cross each other because of its deterministic nature of the hydrodynamic equation. Hence, since the closed trajectory is extended to further away from the collision surface with increasing asymmetry in the particle radii as noted by Adler[125, 87], the hetero-aggregation for unequal-sized particles in a simple shear flow are significantly impeded due to less trajectories entering to the reference particle. Such observation has been verified by the others[50] who summarized their calculations as the correlation equation of the capture efficiency in a simple shear flow.

The practical importance of pure straining flow such as plane and axisymmetrical extensional flow has been noted by the previous works[36, 86]. Particularly, Zeichner has demonstrated that the hydrodynamic interactions are less significant in an extensional flow than in a simple shear flow[36]. As a result, the aggregation in an extensional flow are more effectively enhanced than the one in a simple shear flow. This can be caused by the vorticity accompanied with a simple shear flow, where the contribution to the relative velocity is not affected by hydrodynamic interactions as obviously seen in the trajectory equations. This also corresponds to a rigid rotation of a particle pair. The rotation due to the vorticity decreases the time interval for particles interacting with each other through the van der Waals attraction to overcome hydrodynamic interactions. In principal, no closed trajectory exists in the extensional flow[86, 87]. This means that the extended closed trajectory with decreasing the size ratio does not appear to slow down aggregation in a pure straining flow. Therefore, we expect that the significant reduction of capture efficiency by size ratio found in shear hetero-aggregation is not significant in extensional flow. In addition, some researchers have suggested that the flow in the smallest eddies where turbulent aggregation occurs can be effectively represented by assuming an axisymmetrical extensional flow[126, 127, 128].

However, the experimental observations are still ambiguous on the effect of size ratio

on the orthokinetic hetero-aggregation. The previous work reported that the aggregation is facilitated with decreasing the size ratio[129], while the opposite trend has been reported that the hetero-aggregation is enhanced with increasing the size ratio by the other[130]. Hence, to clarify this problem, Yamauchi has measured the hetero-aggregation for unequal-sized and oppositely-charged particles in a turbulent flow generated by stirring as a function of the size ratio[49]. They reported that the capture efficiencies of turbulent hetero-aggregation are roughly constant with decreasing the size ratio in contrast to the drastic decrease of values calculated using the correlation equation in a simple shear flow by the previous work[50]. Explanation to such insensitivity of the capture efficiency on size ratio is still lacking.

Therefore, in the present study, to give insights to the experimental trend observed by Yamauchi[49], we calculate the capture efficiency of the hetero-aggregation for unequal-sized particles in an axisymmetrical extensional flow by the convevtive-diffusion approach[128, 131] and the ones in a simple shear flow by the correlation equation mentioned above[50]. Furthermore, from the comparison of theoretical values with experimental ones obtained by Yamauchi[49], we discuss the validity of the theory used in this study for the shear hetero-aggregation. It should be noted that such comparisons have never been attempted to clarify the effect of different types of flow on orthokinetic aggregation.

7.2 Conclusion

We have analyzed the experimental data obtained by Yamauchi[49] with the calculations by solving the convective-diffusion equation in an uniaxial extentional flow[131] and by the trajectory analysis in a simple shear flow[50] in the absence of the electrical forces. By comparing between these results, we have shown that the turbulent hetero-aggregation for unequal-sized particles can be more comparable with the calculation by convective-diffusion equation Eq.(**??**) in the extensional flow than the one calculated by the trajectory analysis in a simple shear flow[50]. This might imply that the flow in the microscale turbulence is more likely to be approximated as an axisymmetrical extensional flow than a simple shear flow as noted by Batchelor[126, 127].

Chapter 8

Concluding remarks

In this thesis, we have examined the charging and aggregation behaviors of polystyrene latex particles with sulfate, amidine, or carboxyl groups as model colloidal particles. The charging properties such as surface charge densities and zeta potentials have been studied as a function of salt concentration and types. The charge reversal due to counter-ion adsorption has been examined by the electrophoretic method throughout this thesis. Using the measured electrokinetic potentials, we have analyzed the rate of homo-aggregation in a simple shear flow by the trajectory analysis with DLVO theory. The anionic specificity on both Brownian homo- and hetero-aggregation with charge reversal has been discussed by DLVO theory. Furthermore, to clarify the effect of flow on hetero-aggregation, we have analyzed the hetero-aggregation rates for unequal-sized particles in a mixing flow with the convective-diffusion equation for uniaxial extensional flow. As a result, we have shown that the DLVO theory works for homo- and hetero-aggregation by Brownian diffusion and flow fields.

Here, as concluding remarks, let us summarize the conclusions obtained in this thesis as follows:

1. We have shown that the trajectory analysis with non-linear Poisson-Boltzmann solution is valid to predict aggregation rates in a simple shear flow with electrostatic repulsion by the quantitative comparison of experiments with theory for well-characterized particles for the first time. Our calculation captures typical behaviors of aggregation in a shear flow such as increase in critical coagulation concentration with shear rate G.

2. By analyzing the electrophoretic mobility for carboxyl latex particles in the presence of TPP^+ ions, which induce the charge reversal due to the ion adsorption on the particle surface with its hydrophobicity, we found the reduction in the intrinsic energy of adsorption of TPP^+ with increasing the charge density from $6k_BT$ at the lowest charge density to $4k_BT$ at the highest charge density. This finding supports the conclusion in the previous work[29] and suggests that the non-electrostatic energy of adsorption of TPP^+ is dependent on the surface charge density of adsorbents.

3. We have demonstrated that hetero-aggregation with charge reversal induced by counter-anions can be more repulsive than homo-aggregation for positively-charged particles, which experience charge reversal, due to the stronger interactions with highly- and negatively-charged particles.

4. In the case of monovalent phosphate anion, we have observed that hetero-aggregation between the positively- and negatively-charged particles can be repulsive even below the isoelectric point. This suggests that the weak-positive surface (diffuse layer) potential on the amidine latex can be overcompensated when approaching to the surface with high-negative surface (diffuse layer) potential. These two experimental findings have been supported by DLVO theory.

5. We have shown that the hetero-aggregation for unequal-sized particles in a mixing flow can be more analogous to the calculation by convective-diffusion equation in an uniaxial extensional flow than the one calculated by the trajectory analysis in a simple shear flow[50]. This infers that the flow in the microscale turbulence is more likely to be axisymmetrical extensional flow than simple shear flow as noted by Batchelor[126, 127].

As described above, we have extensively investigated the validity of DLVO theory in kinetics of Brownian and shear aggregation by comparing the theory with experiments in model systems. We could have validated the theory even for more complex systems such as hetero-aggregation in Brownian diffusion and shear flow. Therefore, our results can give us more detailed insights to understand and control the stability of homo- and

hetero-aggregation in more realistic systems. To confirm the validity of our results, studying the hetero-aggregation for unequal-sized particles in different flows such as oscillating flow would clarify the effects of flow types on shear aggregation. The observed less sensitivity of hetero-aggregation in pure straining flow on size ratio can reasonably explain the experimental trends. However, its applicability to turbulent aggregation is still questioning. Considering the theory in randomly fluctuating flow[132, 8] could be a way to discuss the universality of our conclusion. At this moment, we would leave this problem in future studies.

Acknowledgement

Without the help of many people who contributed to this thesis in various ways, for sure, I could not finish this. I would like to express my deep gratitude to all those who gave me the possibility to be accepted this thesis.

First of all, I would like to express my indebtedness to my superviser, Assoc. Prof. Motoyoshi Kobayashi for his hearted mentorship and many help to be accepted as a JSPS research fellow (DC1) and also as a JSPS post-doctoral fellow from next academic year. I could not know how the study in the field of colloid science is excited without his help. And also, I would like to thank Assoc. Prof. Kobayashi giving me the opportunity to stay in the University of Geneva under supervision of Prof. Michal Borkovec. It was my great pleasure to study in his group and it has expanded my perspective to do study and how to proceed it.

I would like to tell my appreciation to Prof. Yasuhisa Adachi in our Colloid laboratory at University of Tsukuba for his valuable and fruitful suggestions throughout my study in the Colloid laboratory, and his thoughtful lectures for my undergraduate. These lecture guided us, which include my classmates, to the field of colloid science.

I would like to thank Assist. Prof. Yuji Yamashita for his suggestions and careful comments on this thesis. This has helped me a lot to improve this thesis and add some more explanations. It was my pleasure to be suggested to print this thesis as a book.

I also would like to thank Assist. Prof. Kazuyoshi Ogawa for his suggestions to further improve this thesis.

I would really appreciate Prof. Mitsuteru Irie at Miyazaki University to teach and have me in his intensive course with boarding on a ship in Toyama prefecture. I would never forget such a great experience to see the wild dolphins in the sea.

I would like to thank Prof. Michal Borkovec from University of Geneva for his acceptance to my stay in his group. And also I really thank Dr. Istvan Szilagyi, Dr.

Gregor Trefalt, Mr. Tianchi Cao, Mr. Tomislav Kramer, and Mrs. Anne-Marie Loup for their help and discussions during my stay. It is a great experience through my life to work with them. And I also thank Mme. Claudine Robert-Grandpierre for her kindly supports and help to live in Perly during my stay in Geneva.

I also would like to thank all of professors and staff of Graduate School of Life and Environmental Sciences, University of Tsukuba for their many supports to go abroad for conferences and to do comfortable student life.

I would like to express my gratitude for all current and former members in our Colloid laboratory for their help and frequent discussions, especially, Mr. Hakim Azizul, Mr. Atsushi Yamaguchi, my classmates, Mr. Yuta Honjo, Mr. Tomohiko Tamaru, and Mr. Sena Taga.

I thank my friend since my undergraduate, Dr. Mami Shimmura from water management laboratory for her kindly help and albums during our campus life that helped me a lot during my stay in Geneva.

I also thank our helpful secretaries and technician, Ms. Ogawa, Ms. Yamada, and Mr. Sakurai for their kind help to organize any conferences and events.

I am grateful for the financial support from University of Tsukuba. And also, I really thank to the support from the Japan Society for the Promotion of Science through the research Fellowship for Young Scientists(DC1) and JSPS KAKENHI Grant Number 15J00805.

Finally, I owe my deepest gratitude to my family, especially, to my mother Yoko Sugimoto, and my dear co-worker Ms. Manami Nishiya for their support and help. It is difficult for me to finish this thesis without her collaboration and help because the part of this thesis is the collaborative work with Ms. Nishiya. I would like to thank her again for her collaboration and help.

January, 2018

Takuya SUGIMOTO

List of publications

1. T. Sugimoto, M. Kobayashi, and Y. Adachi, "Aggregation rate of charged colloidal particles in a shear flow: trajectory analysis using non-linear Poisson-Boltzmann solution", *J. Japan Society of Civil Engineers, Ser. A2 (Applied Mechanics)*, Vol.70 (2), pp.I_475-I_482, 2014.

2. M. Nishiya, T. Sugimoto, and M. Kobayashi, "Electrophoretic mobility of carboxyl latex particles in the mixed solution of 1:1 and 2:1 electrolytes or 1:1 and 3:1 electrolytes: Experiments and modeling", *Colloids and Surfaces A: Physicochemical and Engineering Aspects*, Vol.504, pp.219-227, 2016.

3. T. Sugimoto, M. Nishiya, and M. Kobayashi, "Electrophoretic mobility of carboxyl latex particles: Effects of hydrophobic monovalent counter-ions", *Colloid and Polymer Science*, Vol.295, pp.2405-2411, 2017.

References

[1] M. Elimelech, J. Gregory, and X. Jia. *Particle deposition and aggregation: measurement, modelling and simulation*. Butterworth-Heinemann, 1998.

[2] W. B. Russel, D. A. Saville, and W. R. Schowalter. *Colloidal dispersions*. Cambridge University Press, 1989.

[3] W. H. McAnally and A. J. Mehta. Aggregation Rate of Fine Sediment. *Journal of Hydraulic Engineering*, 126(12):883–892, dec 2000.

[4] B. V. Derjaguin and L Landau. The theory of stability of highly charged lyophobic sols and coalescence of highly charged particles in electrolyte solutions. *Acta Physicochim. URSS*, 1941.

[5] E. J. W. Verwey, J. T. G. Overbeek, and J. T. G. Overbeek. Theory of the stability of lyophobic colloids. *DoverPublications. com*, 1999.

[6] Y. Adachi. Dynamic aspects of coagulation and flocculation. *Advances in Colloid and Interface Science*, 56:1–31, mar 1995.

[7] M. Kobayashi, T. Maekita, Y. Adachi, and H. Sasaki. Colloid stability and coagulation rate of polystyrene latex particles in a turbulent flow. *International Journal of Mineral Processing*, 73(2-4):177–181, feb 2004.

[8] B. K. Brunk, D. L. Koch, and L. W. Lion. Observations of coagulation in isotropic turbulence. *Journal of Fluid Mechanics*, 371:81–107, 1998.

[9] B. K. Brunk, D. L. Koch, and L. W. Lion. Hydrodynamic pair diffusion in isotropic random velocity fields with application to turbulent coagulation. *Physics of Fluids*, 9:2670–2691, 1997.

[10] J. C. Winterwerp. A simple model for turbulence induced flocculation of cohesive sediment. *Journal of Hydraulic Research*, 36(3):309–326, may 1998.

[11] T. Sugimoto, M. Kobayashi, and Y. Adachi. The effect of double layer repulsion on the rate of turbulent and Brownian aggregation : experimental consideration.

Colloids and Surfaces A: Physicochemical and Engineering Aspects, 443:418–424, 2014.

[12] M. V. Smoluchowski. Versuch einer mathematischen Theorie der Koagulationskinetik kolloider Lösungen. *Z. Phys. Chem.*, 92:129–168, 1917.

[13] P. G. Saffman and J. S. Turner. On the collision of drops in turbulent clouds. *Journal of Fluid Mechanics*, 1(1):16–30, may 1956.

[14] H. Brenner. The Stokes resistance of an arbitrary particle. *Chemical Engineering Science*, 18:1–25, 1963.

[15] J. Happel and H. Brenner. *Low Reynolds Number Hydrodynamics: With Special Applications to Particulate Media*. Martinuis Nijhoff, 1983.

[16] N. Fuchs. Effect of the charge of aerosols on their stability. *Z. Phys*, 89:736–742, 1934.

[17] L. A. Spielman. Viscous interactions in Brownian coagulation. *Journal of Colloid and Interface Science*, 33(4):562–571, aug 1970.

[18] E. P. Honig, G. J. Roebersen, and P. H. Wiersema. Effect of hydrodynamic interaction on the coagulation rate of hydrophobic colloids. *Journal of Colloid And Interface Science*, 36(1):97–109, 1971.

[19] H. Reerink and J. Th. G. Overbeek. The rate of coagulation as a measure of the stability of silver iodide sols. *Discussions of the Faraday Society*, 18:74–84, jan 1954.

[20] R. H. Ottewill and J. N. Shaw. Stability of monodisperse polystyrene latex dispersions of various sizes. *Discussions of the Faraday Society*, 42:154–163, jan 1966.

[21] M. Schudel, S. H. Behrens, H. Holthoff, R. Kretzschmar, and M. Borkovec. Absolute Aggregation Rate Constants of Hematite Particles in Aqueous Suspensions: A Comparison of Two Different Surface Morphologies. *Journal of Colloid and Interface Science*, 196(2):241–253, 1997.

[22] J. N. Israelachvili. *Intermolecular and surface forces*. Academic Press, 2011.

[23] S. H. Behrens, D. I. Christl, R. Emmerzael, P. Schurtenberger, and M. Borkovec. Charging and Aggregation Properties of Carboxyl Latex Particles : Experiments versus DLVO Theory. *Langmuir*, 16(12):2566–2575, 2000.

[24] M. L. Jiménez, Á. V. Delgado, and J. Lyklema. Hydrolysis versus ion correlation models in electrokinetic charge inversion: Establishing application ranges. *Langmuir*, 28(17):6786–6793, 2012.

[25] M. Nishiya, T. Sugimoto, and M. Kobayashi. Electrophoretic mobility of carboxyl latex particles in the mixed solution of 1:1 and 2:1 electrolytes or 1:1 and 3:1 electrolytes: Experiments and modeling. *Colloids and Surfaces A: Physicochemical and Engineering Aspects*, 504:219–227, 2016.

[26] G. Trefalt, I. Szilagyi, G. Téllez, and M. Borkovec. Colloidal Stability in Asymmetric Electrolytes: Modifications of the Schulze-Hardy Rule. *Langmuir*, 33(7):1695–1704, 2017.

[27] I. Szilagyi, G. Trefalt, A. Tiraferri, P. Maroni, and M. Borkovec. Polyelectrolyte adsorption, interparticle forces, and colloidal aggregation. *Soft matter*, 10(15):2479–502, apr 2014.

[28] W. Tan, W. Norde, and L. K. Koopal. Interaction between lysozyme and humic acid in layer-by-layer assemblies: Effects of pH and ionic strength. *Journal of colloid and interface science*, 2014.

[29] A. Hakim, M. Nishiya, and M. Kobayashi. Charge reversal of sulfate latex induced by hydrophobic counterion: effects of surface charge density. *Colloid and Polymer Science*, 294(10):1671–1678, 2016.

[30] P. Somasundaran, T. W. Healy, and D. W. Fuerstenau. Surfactant Adsorption at the Solid–Liquid Interface–Dependence of Mechanism on Chain Length. *Journal of Physical Chemistry*, 68(12):3562–3566, 1964.

[31] M. Kobayashi, S. Yuki, and Y. Adachi. Effect of anionic surfactants on the stability ratio and electrophoretic mobility of colloidal hematite particles. *Colloids and Surfaces A: Physicochemical and Engineering Aspects*, 510:190–197, 2016.

[32] J. Lyklema. Overcharging, charge reversal: Chemistry or physics? *Colloids and Surfaces A: Physicochemical and Engineering Aspects*, 291(1-3):3–12, 2006.

[33] A. Martín-Molina, J. A. Maroto-Centeno, R. Hidalgo-Álvarez, and M. Quesada-Pérez. Charge reversal in real colloids: Experiments, theory and simulations. *Colloids and Surfaces A: Physicochemical and Engineering Aspects*, 319(1-3):103–108, 2008.

[34] A. Martín-Molina, C. Calero, J. Faraudo, M. Quesada-Pérez, A. Travesset, and R. Hidalgo-Álvarez. The hydrophobic effect as a driving force for charge inversion in colloids. *Soft Matter*, 5(7):1350, 2009.

[35] T. G. M. van de Ven and S. G. Mason. The microrheology of colloidal dispersions VII. Orthokinetic doublet formation of spheres. *Colloid and Polymer Science*, 255(5):468–479, may 1977.

[36] G. R. Zeichner and W. R. Schowalter. Use of trajectory analysis to study stability of colloidal dispersions in flow fields. *AIChE Journal*, 23(3):243–254, may 1977.

[37] W. R. Schowalter. Stability and Coagulation of Colloids in Shear Fields. *Annual Review of Fluid Mechanics*, 16(1):245–261, jan 1984.

[38] K. Higashitani, K. Yamauchi, Y. Matsuno, and G. Hosokawa. Turbulent coagulation of particles dispersed in a viscous fluid. *Journal of Chemical Engineering of Japan*, 16(4):299–304, 1983.

[39] Y. Adachi, M. A. Cohen Stuart, and R. Fokkink. Kinetics of Turbulent Coagulation Studied by Means of End-over-End Rotation. *Journal of Colloid and Interface Science*, 165:310–317, 1994.

[40] M. Kobayashi and D. Ishibashi. Absolute rate of turbulent coagulation from turbidity measurement. *Colloid and Polymer Science*, 289(7):831–836, feb 2011.

[41] D. Sato, M. Kobayashi, and Y. Adachi. Capture efficiency and coagulation rate of polystyrene latex particles in a laminar shear flow: Effects of ionic strength and shear rate. *Colloids and Surfaces A: Physicochemical and Engineering Aspects*, 266(1-3):150–154, 2005.

[42] W. Lin, M. Kobayashi, M. Skarba, C. Mu, P. Galletto, and M. Borkovec. Heteroaggregation in Binary Mixtures of Oppositely Charged Colloidal Particles. *Langmuir : the ACS journal of surfaces and colloids*, (35):1038–1047, 2006.

[43] T. Cao, T. Sugimoto, I. Szilágyi, G. Trefalt, and M. Borkovec. Heteroaggregation of Oppositely Charged Particles in the Presence of Multivalent Ions. *Phys. Chem. Chem. Phys.*, 19:15160–15171, 2017.

[44] T. Oncsik, G. Trefalt, M. Borkovec, and I. Szilagyi. Specific ion effects on particle aggregation induced by monovalent salts within the Hofmeister series. *Langmuir*, 31(13):3799–3807, 2015.

[45] M. Pavlovic, R. Huber, M. Adok-Sipiczki, C. Nardin, and I. Szilagyi. Ion specific effects on the stability of layered double hydroxide colloids. *Soft Matter*, 12(17):4024–4033, 2016.

[46] M. Kobayashi. Aggregation of Unequal-sized and Oppositely Charged Colloidal Particles in a Shear Flow. *Journal of Applied Mechanics*, 11:517–523, 2008.

[47] M. Kobayashi. Kinetics of Shear Coagulation of Oppositely Charged Particles : A Trajectory Analysis. *Theoretical and Applied Mechanics Japan*, 56:267–272, 2008.

[48] T. Sugimoto, Y. Watanabe, and M. Kobayashi. Kinetics of turbulent heterocoagulation of oppositely charged colloidal particles. *Theoretical and applied mechanics Japan*, 63(0):133–145, 2015.

[49] C. Yamauchi. *Turbulent hetero-aggregation for mixtures of oppositely-charged particles: Size ratio effects*. Iwate University, thesis edition, 2009.

[50] M. Han and D. F. Lawler. The (Relative) Insignificance of G in Flocculation. *Journal (American Water Works Association)*, 84:79–91, 1992.

[51] V. A. Parsegian. *Van der Waals Forces*. Cambridge University Press, 2006.

[52] E. M. Lifshitz. The Theory of Molecular Attractive Forces between Sol ids. *J. Exper. Theoret. Phys. USSR*, 29:94–110, 1955.

[53] T. Kondo, H. Ohshima, N. Muramatsu, and K. Makino. *Biophysical Chemistry*. Sankyo Shuppan, 1992.

[54] B. V. Derjaguin. Friction and adhesion. IV. The theory of adhesion of small particles. *Kolloid Zeits*, 69:155–164, 1934.

[55] R. S. Bradley. LXXIX. The cohesive force between solid surfaces and the surface energy of solids. *The London, Edinburgh, and Dublin Philosophical Magazine and Journal of Science*, 13(86):853–862, apr 1932.

[56] H. C. Hamaker. The London-van der Waals Attraction between Spherical Particles. *Physica*, 4(10):1058–1072, 1937.

[57] J. H. Schenkel and J. A. Kitchener. A test of the Derjaguin-Verwey-Overbeek theory with a colloidal suspension. *Transactions of the Faraday Society*, 56(0):161, jan 1960.

[58] E. J. Clayfield, E. C. Lumb, and P. H. Mackey. Retarded dispersion forces in

colloidal particles-Exact integration of the casimir and polder equation. *Journal of Colloid And Interface Science*, 37(2):382–389, 1971.

[59] R. H. Davis. Gravity-induced coalescence of drops at arbitrary Peclet numbers. *Journal of Fluid Mechanics*, 280:119–148, 1994.

[60] S. H. Behrens and M. Borkovec. Electrostatic Interaction of Colloidal Surfaces with Variable Charge. *The Journal of Physical Chemistry B*, 103(15):2918–2928, apr 1999.

[61] S. H. Behrens and M. Borkovec. Exact Poisson-Boltzmann solution for the interaction of dissimilar charge-regulating surfaces. *Physical Review E*, 60(6):7040–7048, dec 1999.

[62] S. L. Carnie and D. Y. C. Chan. Interaction free energy between plates with charge regulation: A linearized model. *Journal of Colloid and Interface Science*, 161:260–264, 1993.

[63] S. H. Behrens and M. Borkovec. Electric double layer interaction of ionizable surfaces: Charge regulation for arbitrary potentials. *The Journal of Chemical Physics*, 111(1):382, 1999.

[64] R. Pericet-camara, G. Papastavrou, S. H. Behrens, and M. Borkovec. Interaction between Charged Surfaces on the Poisson - Boltzmann Level: The Constant Regulation Approximation. *Journal of Physical Chemistry B*, 108:19467–19475, 2004.

[65] G. Trefalt, I. Szilagyi, and M. Borkovec. Poisson-Boltzmann description of interaction forces and aggregation rates involving charged colloidal particles in asymmetric electrolytes. *Journal of Colloid and Interface Science*, 406:111–120, 2013.

[66] G. Trefalt, F. J. M. Ruiz-Cabello, and M. Borkovec. Interaction forces, heteroaggregation, and deposition involving charged colloidal particles. *Journal of Physical Chemistry B*, 118(23):6346–6355, 2014.

[67] G. Trefalt, S. H. Behrens, and M. Borkovec. Charge Regulation in the Electrical Double Layer: Ion Adsorption and Surface Interactions. *Langmuir*, 32:380–400, 2016.

[68] F. J. M. Ruiz-Cabello, M. Moazzami-Gudarzi, M. Elzbieciak-Wodka, P. Maroni, C. Labbez, M. Borkovec, and G. Trefalt. Long-ranged and soft interactions be-

tween charged colloidal particles induced by multivalent coions. *Soft Matter*, 11:1562–1571, 2015.

[69] B. Vincent. Early (pre-DLVO) studies of particle aggregation. *Advances in Colloid and Interface Science*, 170:56–67, 2012.

[70] S. Wall. The history of electrokinetic phenomena. *Current Opinion in Colloid & Interface Science*, 15(3):119–124, jun 2010.

[71] R. W. O'Brien and L. R. White. Electrophoretic mobility of a spherical colloidal particle. *Journal of the Chemical Society, Faraday Transactions 2*, 74(0):1607, jan 1978.

[72] R. H. Ottewill and J. N. Shaw. Electrophoretic studies on polystyrene latices. *Journal of Electroanalytical Chemistry and Interfacial Electrochemistry*, 37(1):133–142, jun 1972.

[73] M. Kobayashi. Electrophoretic mobility of latex spheres in the presence of divalent ions: Experiments and modeling. *Colloid and Polymer Science*, 286:935–940, 2008.

[74] T. Sugimoto, M. Kobayashi, and Y. Adachi. Aggregation Rate of Charged Colloidal Particles in a Shear Flow : Trajectory Analysis Using Non-linear Poisson-Boltzmann Solution. *J. Applied Mechanics, JSCE*, 70(2):I_475–I_482, 2014.

[75] H. Ohshima, T. W. Healy, and L. R. White. Approximate analytic expressions for the electrophoretic mobility of spherical colloidal particles and the conductivity of their dilute suspensions. *Journal of the Chemical Society, Faraday Transactions 2*, 79(11):1613, jan 1983.

[76] H. Ohshima. Approximate expression for the electrophoretic mobility of a spherical colloidal particle in a solution of general electrolytes. *Colloids and Surfaces A: Physicochemical and Engineering Aspects*, 267(1-3):50–55, oct 2005.

[77] H. Ohshima. Simple approximate analytic expression for the electrophoretic mobility of a spherical colloidal particle in a mixed solution of 1:1 and 2:1 electrolytes. *Colloid and Polymer Science*, 292(6):1457–1461, 2014.

[78] S. Ahualli, A. V. Delgado, S. J. Miklavcic, and L. R. White. Dynamic Electrophoretic Mobility of Concentrated Dispersions of Spherical Colloidal Particles. On the Consistent Use of the Cell Model. *Langmuir*, 22(16):7041–7051, 2006.

[79] S. Ahualli, A. V. Delgado, S. J. Miklavcic, and L. R. White. Use of a cell model for the evaluation of the dynamic mobility of spherical silica suspensions. *Journal of Colloid and Interface Science*, 309(2):342–349, may 2007.

[80] B. H. Bradshaw-Hajek, S. J. Miklavcic, and L. R. White. Dynamic Dielectric Response of Concentrated Colloidal Dispersions: Comparison between Theory and Experiment. *Langmuir*, 25(4):1961–1969, feb 2009.

[81] H. Ohshima. *Electrical phenomena at interfaces and biointerfaces : fundamentals and applications in nano-, bio-, and environmental sciences*. Wiley, 2012.

[82] G. K. Batchelor and J. T. Green. The hydrodynamic interaction of two small freely-moving spheres in a linear flow field. *Journal of Fluid Mechanics*, 56(02):375, nov 1972.

[83] D. J. Jeffrey and Y. Onishi. Calculation of the resistance and mobility functions for two unequal rigid spheres in low-Reynolds-number flow. *Journal of Fluid Mechanics*, 139:261–290, 1984.

[84] D. J. Jeffrey. The calculation of the low Reynolds number resistance functions for two unequal spheres. *Physics of Fluids A: Fluid Dynamics*, 4(1):16–29, 1992.

[85] S. Kim and S. J. Karrila. *Microhydrodynamics: principles and selected applications*. Courier Corporation, 1991.

[86] P. A. Arp and S. G. Mason. The kinetics of flowing dispersions: VIII. Doublets of rigid spheres (theoretical). *Journal of Colloid and Interface Science*, 61(1):21–43, aug 1977.

[87] P. M. Adler. Interaction of unequal spheres: I. Hydrodynamic interaction: Colloidal forces. *Journal of Colloid and Interface Science*, 84(2):461–473, dec 1981.

[88] Q. Wang. A study on shear coagulation and heterocoagulation. *Journal of Colloid and Interface Science*, 150(2):418–427, may 1992.

[89] M. Vanni and G. Baldi. Coagulation efficiency of colloidal particles in shear flow. *Advances in Colloid and Interface Science*, 97(1-3):151–177, mar 2002.

[90] A. A. Townsend. The measurement of double and triple correlation derivatives in isotropic turbulence. *Mathematical Proceedings of the Cambridge Philosophical Society*, 43(4):560–570, 1947.

[91] H. Ohshima. *Biophysical chemistry of biointerfaces*. Wiley, 2013.

[92] W. M. Haynes. *CRC Handbook of Chemistry and Physics, 95th Edition.* CRC Press, 2014.

[93] The Chemical Society of Japan, editor. *Kagaku Binran (Ed.).* Maruzen, 5th ed. edition, 2004.

[94] M. Elzbieciak-Wodka, M. N. Popescu, F. J. M. Ruiz-Cabello, G. Trefalt, P. Maroni, and M. Borkovec. Measurements of dispersion forces between colloidal latex particles with the atomic force microscope and comparison with Lifshitz theory. *Journal of Chemical Physics*, 140, 2014.

[95] M. Quesada-Pérez, E. González-Tovar, A. Martín-Molina, M. Lozada-Cassou, and R. Hidalgo-Álvarez. Ion size correlations and charge reversal in real colloids. *Colloids and Surfaces A: Physicochemical and Engineering Aspects*, 267(1-3):24–30, 2005.

[96] F. Vereda, A. Martín Molina, R. Hidalgo-Alvarez, and M. Quesada-Pérez. Specific ion effects on the electrokinetic properties of iron oxide nanoparticles: experiments and simulations. *Phys. Chem. Chem. Phys. Phys. Chem. Chem. Phys*, 17(17):17069–17078, 2015.

[97] C. Calero, J. Faraudo, and D. Bastos-González. Interaction of monovalent ions with hydrophobic and hydrophilic colloids: Charge inversion and ionic specificity. *Journal of the American Chemical Society*, 133(38):15025–15035, 2011.

[98] L. Perez-Fuentes, C. Drummond, J. Faraudo, and D. Bastos-González. Anions makes the difference: Insights from the interaction of big cations and anions with poly(N-isopropylacrylamide) chains and microgels. *Soft Matter*, 11:5077, 2015.

[99] K. Besteman, M. A. G. Zevenbergen, and S. G. Lemay. Charge inversion by multivalent ions: Dependence on dielectric constant and surface-charge density. *Physical Review E - Statistical, Nonlinear, and Soft Matter Physics*, 72:1–9, 2005.

[100] P. Sipos, P. M. May, and G. T. Hefter. Carbonate removal from concentrated hydroxide solutions. *The Analyst*, 125(5):955–958, 2000.

[101] Y. Zhao and G. R. Freeman. Electrical Conductances of Tetraphenylphosphonium and Tetraphenylboride Salts in C 1 to C 4 Alcohols. 3654(96):17568–17572, 1996.

[102] L. Ehrl, Z. Jia, H. Wu, M. Lattuada, M. Soos, and M. Morbidelli. Role of counterion association in colloidal stability. *Langmuir*, 25(13):2696–2702, 2009.

[103] J. I. Kim. Preferential solvation of single ions. A critical study of the Ph4AsPh4B assumption for single ion thermodynamics in amphiprotic and dipolar-aprotic solvents. *The Journal of Physical Chemistry*, 82(2):191–199, 1978.

[104] Alexander M. Smith, Plinio Maroni, and Michal Borkovec. Attractive Non-DLVO Forces Induced by Adsorption of Monovalent Organic Ions. *Physical Chemistry Chemical Physics*, 20:158–164, 2018.

[105] H. Schulze. -. *J. Prakt. Chem.*, 25:431–452, 1882.

[106] W. B. Hardy. -. *Proc. R. Soc. London*, 66:110–125, 1900.

[107] J. T. G. Overbeek. The Rule of Schulze and Hardy. *Pure and Applied Chemistry*, 52(5):1151–1161, jan 1980.

[108] B. Tezak, E. Matijevic, and K. F. Schulz. Coagulation of hydrophobic sols in statu nascendi 3. The influence of the ionic size and valency of the counterion. *Journal of Physical Chemistry*, 59(8):769–773, 1955.

[109] G. Frens and J. J. F. G. Heuts. The Double Layer Potential as a Rate Determining Factor in the Coagulation of Electrocratic Collids. *Colloids and Surfaces*, 30:295–305, 1988.

[110] C. Schneider, M. Hanisch, B. Wedel, A. Jusufi, and M. Ballauff. Experimental study of electrostatically stabilized colloidal particles: Colloidal stability and charge reversal. *Journal of Colloid and Interface Science*, 358(1):62–67, 2011.

[111] I. Szilagyi, A. Polomska, D. Citherlet, A. Sadeghpour, and M. Borkovec. Charging and aggregation of negatively charged colloidal latex particles in the presence of multivalent oligoamine cations. *Journal of Colloid and Interface Science*, 392(1):34–41, 2013.

[112] N. O. Mchedlov-Petrossyan, V. K. Klochkov, and G. V. Andrievsky. Colloidal dispersions of fullerene C60 in water: some properties and regularities of coagulation by electrolytes. *Journal of the Chemical Society, Faraday Transactions*, 93(24):4343–4346, 1997.

[113] M. Kobayashi, M. Skarba, P. Galletto, D. Cakara, and M. Borkovec. Effects of heat treatment on the aggregation and charging of Stöber-type silica. *Journal of Colloid and Interface Science*, 292(1):139–147, 2005.

[114] S. Xu and Z. Sun. Progress in coagulation rate measurements of colloidal disper-

sions. *Soft Matter*, 7(24):11298, nov 2011.

[115] R. O. James, A. Homola, and T. W. Healy. Heterocoagulation of amphoteric latex colloids. *Journal of the Chemical Society, Faraday Transactions 1: Physical Chemistry in Condensed Phases*, 73(0):1436, jan 1977.

[116] H. Kihira and E. Matijević. Kinetics of Heterocoagulation. 3. Analysis of Effects Causing the Discrepancy between the Theory and Experiment. *Langmuir*, 8(12):2855–2862, 1992.

[117] J. Labille, C. Harns, J. Y. Bottero, and J. Brant. Heteroaggregation of titanium dioxide nanoparticles with natural clay colloids. *Environmental Science and Technology*, 49(11):6608–6616, 2015.

[118] B. M. Smith, D. J. Pike, M. O. Kelly, and J. A. Nason. Quantification of Heteroaggregation between Citrate-Stabilized Gold Nanoparticles and Hematite Colloids. *Environmental Science and Technology*, 49(21):12789–12797, 2015.

[119] M. I. Mishchenko and D. W. Mackowskib. Electromagnetic Scattering by Ramdomly Oriented Bispheres: Comparison of Theory and Experiment and Benchmark Calculations. *Journal of Quantitative Spectroscopy and Radiative Transfer*, 55(5):683–694, 1996.

[120] P. Galletto, W. Lin, M. I. Mishchenko, and M. Borkovec. Light-scattering form factors of asymmetric particle dimers from heteroaggregation experiments. *Journal of Chemical Physics*, 123:064709, 2005.

[121] N. Ryde and E. Matijević. Kinetics of heterocoagulation. Part 4.—Evaluation of absolute coagulation rate constants using a classical light scattering technique. *J. Chem. Soc., Faraday Trans.*, 90(1):167–171, jan 1994.

[122] M. Elimelech. Effect of Particle Size on the Kinetics of Particle Deposition under Attractive Double Layer Interactions, 1994.

[123] M. Kobayashi, H. Nanaumi, and Y. Muto. Initial deposition rate of latex particles in the packed bed of zirconia beads. *Colloids and Surfaces A: Physicochemical and Engineering Aspects*, 347(13):2–7, 2009.

[124] T. W. Healy, G. R. Wiese, D. E. Yates, and B. V. Kavanagh. Heterocoagulation in Mixed Oxide Colloidal Dispesions. *J. Colloid Interface Sci.*, 42(3):647–649, 1973.

[125] P. M. Adler. Heterocoagulation in shear flow. *Journal of Colloid and Interface Science*, 83(1):106–115, sep 1981.

[126] G. K. Batchelor. Mass transfer from a particle suspended in fluid with a steady linear ambient velocity distribution. *Journal of Fluid Mechanics*, 95(2):369–400, 1979.

[127] G. K. Batchelor. Mass transfer from small particles suspended in turbulent fluid. *Journal of Fluid Mechanics*, 98(3):609–623, 1980.

[128] S. Melis, M. Verduyn, G. Storti, and M. Morbidelli. Effect of Fluid Motion on the Aggregation of Small Particles Subject to Interaction Forces. *AIChE Journal*, 45(7):1383–1393, 1999.

[129] K. Furusawa and C. Anzai. Preparation of composite fine particles by heterocoagulation. *Colloid and Polymer Science*, 265:882–888, 1987.

[130] S. Harley, D. W. Thompson, and B. Vincent. The adsorption of small particles onto larger particles of opposite charge Direct electron microscope studies. *Colloids and Surfaces*, 62:153–162, 1992.

[131] M. Lattuada and M. Morbidelli. Effect of repulsive interactions on the rate of doublet formation of colloidal nanoparticles in the presence of convective transport. *Journal of Colloid and Interface Science*, 355(1):42–53, 2011.

[132] B. K. Brunk, D. L. Koch, and L. W. Lion. Turbulent coagulation of colloidal particles. *Journal of Fluid Mechanics*, 364:81–113, 1998.